

6-25-2015

Multispectral Metamaterial Detectors for Smart Imaging

John A. Montoya

Follow this and additional works at: https://digitalrepository.unm.edu/ece_etds



Part of the [Electrical and Computer Engineering Commons](#)

Recommended Citation

Montoya, John A.. "Multispectral Metamaterial Detectors for Smart Imaging." (2015). https://digitalrepository.unm.edu/ece_etds/
179

This Dissertation is brought to you for free and open access by the Engineering ETDs at UNM Digital Repository. It has been accepted for inclusion in Electrical and Computer Engineering ETDs by an authorized administrator of UNM Digital Repository. For more information, please contact disc@unm.edu.

John Montoya

Candidate

Electrical and Computer Engineering

Department

This dissertation is approved, and it is acceptable in quality and form for publication:

Approved by the Dissertation Committee:

Sanjay Krishna, Ph.D., UNM, ECE , Chairperson

Steve Brueck, Ph.D., UNM, ECE

Terefe Habteyes, Ph.D., UNM, Chemistry

Willie Padilla, Ph.D., Duke University, ECE

David Peters, Ph.D., SNL

MULTISPECTRAL METAMATERIAL DETECTORS FOR SMART IMAGING

By

JOHN A. MONTOYA

DISSERTATION

Submitted in Partial Fulfillment of the
Requirements for the Degree of

**Doctor of Philosophy
Engineering**

The University of New Mexico
Albuquerque, New Mexico

May, 2015

© John A. Montoya, 2015

Dedication

To my parents, Debbie and Ronald.

“What does a fish know about the water in which he swims all his life?”

- A. Einstein

Acknowledgments

First, I would like to thank my parents for giving me their love and support. Despite breaking many new electronic toys and hoarding broken home appliances in my bedroom closet for parts as a child, my parents never gave up on me. They knew I was “different.” I would also like to thank Berenice, the love of my life, for allowing me to be myself and for reminding me of who I am when I lost sight. I can’t wait to meet our son Johnny and to help guide him through this wild, crazy, highly rewarding world. I would also like to thank my best friend Anthony Salvagno for the countless coffee breaks to talk about physics without preconceived boundaries. If the past, present, and future exist simultaneously, this suggests that our friendship is imprinted into the fabric of space-time indefinitely.

To my fellow graduate students, thank you for all of your help and support throughout this journey. Senior Myers, Pankaj Ahirwar, Stephen Clark, Freddy Santiago, Lilian Casias, and Alireza Kazemi, thank you for your friendship and the many beers at Marble. Brianna Klein, you are a La Cumbre fan, so thank you for La Cumbre beer and the many jokes. Sebastian Godoy and David Ramirez, you guys preferred Tractor Brewing for very obvious reasons. Thanks for the many great times. Ajit Barve, you actually don’t like beer at all, so I would like to thank you for many great conversations at Fuddruckers. Nutan Gautam, you don’t like beer or meat-related restaurants, so I will have to thank you for our many conversations at Namaste. And finally, Ted Schuler-Sandy, because you live too far from modern society to hang out after hours, thank you for being my office buddy and for our many lunch breaks together.

I would also like to thank the many people who helped train me in the cleanroom. First, I would like to thank Vincent Chow. You taught me to be bold and aggressive with how I approach research. Ha Sul Kim, thank you for teaching me patience and that a steady hand is my key to success. Sang Jun Lee, you taught me to never give up trying and to try to see the big picture, the really big picture. Also, thank you Steve Wawrzyniec, Doug Wozniak, Beth Fuchs, and Rick Bradley for allowing me to test the boundaries of cleanroom policy. Your patience and willingness to accommodate my research endeavors made my graduation possible.

I would like to sincerely thank my committee members, Prof. Steven R. J. Brueck, Prof. Terefe Habteyes, Prof. Willie Padilla, and Dr. David Peters. Your time and

constructive inputs are incredibly valuable to me. Also, thank you Prof. Padilla for giving me a path to further express myself in science. I'm looking forward to it. And finally, I would also like to thank my research advisor, Prof. Sanjay Krishna, for his guidance and support throughout my graduate studies. Despite breaking my new electronic toys, he never gave up on me. He knew I was "different."

Abstract

The ability to produce a high quality infrared image has significantly improved since its initial development in the 1950's [1]. The first generation consisted of a single pixel that required a two-dimensional raster scan to produce an image. The second generation comprised of a linear array of pixels that required a mechanical sweep to produce an image. The third generation utilizes a two-dimensional array of pixels to eliminate the need for a mechanical sweep. Third generation imaging technology incorporates pixels with single color or broadband sensitivity, which results in "black and white" images. The research presented in this dissertation focuses on the development of 4th generation infrared detectors for the realization of a new generation of infrared focal plane array. To achieve this goal, we investigate metamaterials to realize multicolor detectors with enhanced quantum efficiency for similar function to a human retina. The key idea is to engineer the pixel such that it not only has the ability to sense multimodal data such as color, polarization, dynamic range and phase but also the intelligence to transmit a reduced data set to the central processing unit (neuromeritics). In this dissertation, we utilize both a quantum well infrared photodetector (QWIP) and interband cascade detector (ICD) hybridized with a metamaterial absorber for enhanced multicolor sensitivity in the infrared regime. Through this work, along with some design lessons throughout this iterative process, we design, fabricate and demonstrate the first deep-subwavelength multispectral infrared detector using an ultra-thin type-II superlattice (T2-SL) detector coupled with a metamaterial absorber with 7X enhanced quantum efficiency. We also identify useful versus non-useful absorption through a combination of absolute absorption and quantum efficiency measurements. In addition to these research efforts, we also demonstrate a dynamic multicolor metamaterial in the

terahertz regime with electronically tunable frequency and gain for the first time. Utilizing an electronically tunable metamaterial, one can design an imaging system that can take multiple spectral responses within one frame for the classification of objects based on their spectral fingerprint.

Table of Contents

List of Figures	xii
List of Tables	xviii
Chapter 1 : Introduction	1
1.2 Prior Multicolor Detector Art	4
1.3 New Research Thrust	7
1.4 Contribution and Organization of This Work	9
1.5 Summary	11
Chapter 2 : Materials and Methods	12
2.1 Dark Current	12
2.2 Responsivity	15
2.3 Electrical Noise	17
2.4 Specific Detectivity	18
2.5 Quantum Efficiency	20
2.6 Absolute Absorption Measurement	20
2.7 Quantum Well Infrared Photodetectors (QWIPs)	21
2.7.1 Dark Current in QWIPs	22
2.8 Type-II Superlattice Photodetectors	24
2.8.1 Interband Quantum Cascade Photodetector	26
2.9 Summary	29
Chapter 3 : Metamaterial Photodetector Theory and Design	30
3.1 Overview of Metamaterials	30
3.1.1 Effective Permeability	31

3.1.2 Effective Permittivity	33
3.2 Metamaterial Absorber	34
3.3 Metamaterial Photodetector	36
3.3.1 Absorption Coefficient Measurement.....	37
3.3.2 Metamaterial Photodetector Design Scheme	40
3.3.3 Power Loss Density Profile	45
3.3.4 Angle Dependence	46
3.4 Summary	47
Chapter 4 : Detector Fabrication.....	49
4.1 Conventional IR FPA Fabrication Process	49
4.1.1 Conventional IR FPA Fabrication Issues.....	62
4.2 Prototype Chip Fabrication Process.....	64
4.2.1 Prototype Chip Fabrication Issues	69
4.3 Next Generation FPA: The Smart Imager	70
4.4 Summary	75
Chapter 5 : Metamaterial QWIP	77
5.1 Detector Design	77
5.2 Experimental Realization.....	81
5.3 Summary	86
Chapter 6 : Metamaterial Type II Superlattice	88
6.1 Detector Design	89
6.2 Experimental Realization.....	90
6.2.1 Specific Detectivity Measurement.....	92

6.2.2 Dark Current Measurement.....	93
6.3 Summary	95
Chapter 7 : Vision for a Dynamic IR Photodetector.....	96
7.1 Dynamic Terahertz Spatial Light Modulator.....	98
7.1.1 Design and Fabrication	99
7.1.2 Results and Discussion	102
7.2 Experimental Methods	106
7.3 Electromagnetic Simulation.....	107
7.4 Summary	111
Chapter 8 : Summary and Future Work.....	113
8.1 Specific Detectivity Enhancement	114
References	116

List of Figures

Figure 1.1: 1 st , 2 nd and 3 rd Generation FPA Technology	1
Figure 1.2: (A) A typical imaging system versus (B) an ideal imaging system for the classification of objects.....	3
Figure 1.3: Schematic of a two color MW/LWIR MCT FPA with (A) sequential and (B) simultaneous mode operation	5
Figure 1.4: Schematic of two color MW/LWIR QWIP FPA	6
Figure 1.5: (A) Dual-color InAs/GaSb SL FPA and (B) captured image for the detection of carbon dioxide.....	7
Figure 1.6: Example of smart pixels with their colors tuned to the spectral response of granite	8
Figure 2.1: Voltage versus current measurement setup for infrared photodetector dark current measurements	13
Figure 2.2: Illustration of SRH generation-recombination current, band to band tunneling current, and trap assisted tunneling current in a narrow bandgap PIN diode	15
Figure 2.3: Responsivity measurement setup to determine an electrical output signal to an optical input signal ratio.....	16
Figure 2.4: Noise measurement setup for the characterization of infrared photodetectors ...	18
Figure 2.5: Absolute absorption measurement of a photodetector with an infrared microscope	21
Figure 2.6: Schematic diagram of GaAs/AlGaAs QWIP	22
Figure 2.7: Three dark current mechanisms in an inter-sub-band photodetector: 1-ground state tunneling, 2-thermally assisted tunneling and 3-thermionic emission.	23

Figure 2.8: Band structure diagram in (two stages of) interband cascade photodetectors. ...	28
Figure 3.1: Illustration of a multicolor metamaterial photodetector.....	30
Figure 3.2: Illustration of a split-ring resonator at resonance.....	31
Figure 3.3: Illustration of an electric split-ring resonator at resonance	33
Figure 3.4: (A) Schematic of a MMA unit cell and its dimensions are $a = 2\mu\text{m}$, $l = 1.5\mu\text{m}$, $w = 0.3\mu\text{m}$, and $t=0.4\mu\text{m}$. Power loss density profile from (B) the top and (C) the side of the MMA with vertically polarized incoming radiation	35
Figure 3.5: Calculated effective parameters for the proposed metamaterial absorber	36
Figure 3.6: Experimental setup for measuring the absorption coefficient of an epi-layer	38
Figure 3.7: Approximate absorption coefficient for a 10-ML InAs / 10 ML GaSb T2-SL...	39
Figure 3.8: Growth profile of our simulated interband quantum cascade photodetector	40
Figure 3.9: Illustration of the simulated QCD structure and its various layers, which include a backside pattern, a contact and hole barrier, an absorber, a contact and electron barrier, and ground plane metal	41
Figure 3.10: (A) Simulated spectral response of a metamaterial photodetector and its (B) impedance matching curve	42
Figure 3.11: Simulated absorption coefficient for impedance matching the cavity to free space and simulated absolute absorption spectrum	43
Figure 3.12: Mathematical relationships between complex permittivity, refractive index, and absorption coefficient.....	43
Figure 3.13: Illustration of how a metamaterial photodetectors geometry can be tuned to the absorption coefficient of the cavity (assuming the absorption coefficient of the T2-SL absorber is the dominant effect).....	44

Figure 3.14: Simulated absolute absorption response of each geometry with an absorption coefficient of 3500cm^{-1}	45
Figure 3.15: (A) Simulated power loss density profile of an interband cascade photodetector at the absorption peak and (B) spectral response with an active region absorption coefficient of 3500cm^{-1} and dispersive metals	46
Figure 3.16: (A) Simulated TE response and (B) TM response as a function of incident angle for a metamaterial photodetector with $a = 200\text{nm}$	47
Figure 4.1: Conventional infrared focal plane array architecture	50
Figure 4.2: Fabrication steps to define a pixel array beginning with a mesa etch, passivation layer, contact layer, and under bump metal	53
Figure 4.3: Fabrication steps to define an indium bump for flip-chip bonding	54
Figure 4.4: (A) FPA and ROIC alignment with a split-screen microscope (B) FPA and ROIC bonding	55
Figure 4.5: FPA flip-chip bonding recipe with 400g of applied force and 170C of applied heat	56
Figure 4.6: Placement of underfill epoxy between the ROIC and FPA	56
Figure 4.7: Chemical mechanical polishing of an FPA down to $20\mu\text{m}$	57
Figure 4.8: Selective substrate removal of GaSb with an AlAsSb etch stop layer	59
Figure 4.9: GaSb and AlAsSb etch rates with varying SF ₆ to BCl ₃ gas ratios for 100W RF power and 100mTorr chamber pressure	60
Figure 4.10: Selective substrate removal of GaSb on AlAsSb	61
Figure 4.11: Corner image of an FPA during substrate removal with the AlAsSb etch stop partially exposed	62

Figure 4.12: Completed fabrication of a conventional infrared focal plane array.....	62
Figure 4.13: FPA with a cracked semiconductor ground plane due to thermal stress.....	63
Figure 4.14: (A) Side profile and (B) SEM image of the backside of a conventional IR FPA after substrate removal with excess epoxy along its boundary.....	64
Figure 4.15: Next generation FPA architecture	65
Figure 4.16: Fabrication of a pixel mesa with contact metal and a passivation layer	66
Figure 4.17: UBM on the pixel array.....	66
Figure 4.18: Silicon control chip with 40 μ m indium bumps.....	67
Figure 4.19: Flip-chip bonding optimization scheme for 40 μ m indium bumps.....	68
Figure 4.20: Excess epoxy removal with a dicing saw	68
Figure 4.21: Completed prototype FPA / Test chip.....	69
Figure 4.22: Fabrication steps to define a pixel array beginning with metamaterial patterning, mesa etch, passivation layer, and contact layer	72
Figure 4.23: Illustration of the pixel array temporarily bonded to a flexible handle wafer...	73
Figure 4.24: Premise behind epitaxial liftoff with phosphorus containing lift-off layers	73
Figure 4.25: Metal deposition step to define a metal contact onto the bottom side of each pixel in the array	74
Figure 4.26: An advanced FPA bonded to a ROIC is exposed to a solvent to remove the temporary bonding polymer.....	75
Figure 4.27: Advantages gained with the proposed FPA design and fabrication process.....	76
Figure 5.1: Broadband quantum well infrared photodetector design	78
Figure 5.2: Spectral response of the QWIP with a 45 degree facet	79

Figure 5.3: Simulated absorption coefficient for impedance matching the cavity to free space and simulated absolute absorption spectrum	80
Figure 5.4: Simulated QWIP response with different backside patterns	81
Figure 5.5: Z-contrast images of AuGe/Ni/Au Ohmic contact metal with different rapid thermal anneal temperatures: (A) 265C and (B) 300C [73]	82
Figure 5.6: E-beam photolithography on the backside of the QWIP test chip	83
Figure 5.7: Measured photocurrent response of a metamaterial QWIP	84
Figure 5.8: Electromagnetic field penetration and radiation absorption efficiency as a function of photodetector thickness	85
Figure 5.9: Photocurrent response of multiple pixels with each graph containing multiple photocurrent measurements of pixels with the same backside pattern	86
Figure 6.1: (A) 375nm thick infrared photodetector pixel (B) Power loss density profile of a few metamaterial absorber unit cells that results from incoming radiation.....	88
Figure 6.2: Heterostructure schematic of the Interband Cascade Detector and SEM images of the backside of each fabricated pixel with varying geometry.....	90
Figure 6.3: (a) Total absorption obtained from the detectors using an IR microscope and (b) quantum efficiency extracted from the photocurrent.....	91
Figure 6.4: Specific detectivity measurement for metamaterial detector geometries $a = 200\text{nm}$, $a = 300\text{nm}$, $a = 400\text{nm}$ and a reference pixel with no backside pattern.....	93
Figure 6.5: Dark current measurement for all detector pixels to demonstrate a consistent response.....	94
Figure 6.6: Arrhenius plot of a thin interband cascade photodetector	95
Figure 7.1: Dynamic metamaterial photodetector concept	97

Figure 7.2: Design and structure detail of the electronically controlled THz metamaterial absorber based spatial light modulator (MMA-SLM).	100
Figure 7.3: Experimentally measured and computationally simulated frequency dependent reflectance and modulation index (defined in the text) of the metamaterial absorber shown for each color sub-pixel.	103
Figure 7.4: Spatial light modulator performance.	105
Figure 7.5: Voltage dependent current (IV) profile shown with the standard deviation plotted as the error bars for the 62 functioning pixels.	107
Figure 7.6: Numerical simulation results of the metamaterial absorber.	110
Figure 8.1: Detectivity versus photodetector thickness with varying absorption coefficient values	114

List of Tables

Table 7.1: The dimensions for each frequency (THz) color pixel as relating to Figure 7.2c,d.
..... 102

Chapter 1 : Introduction

The ability to produce a high quality infrared image has significantly improved since its initial development in the 1950's [1]. The first generation consisted of a single pixel that required a two-dimensional raster scan to produce an image. The second generation comprised of a linear array of pixels that required a mechanical sweep to produce an image. The third generation utilizes a two-dimensional array of pixels to eliminate the need for a mechanical sweep. Third generation imaging technology incorporates pixels with single color or broadband sensitivity, which results in "black and white" images. Figure 1.1 is an illustration of all prior infrared pixel array technologies.

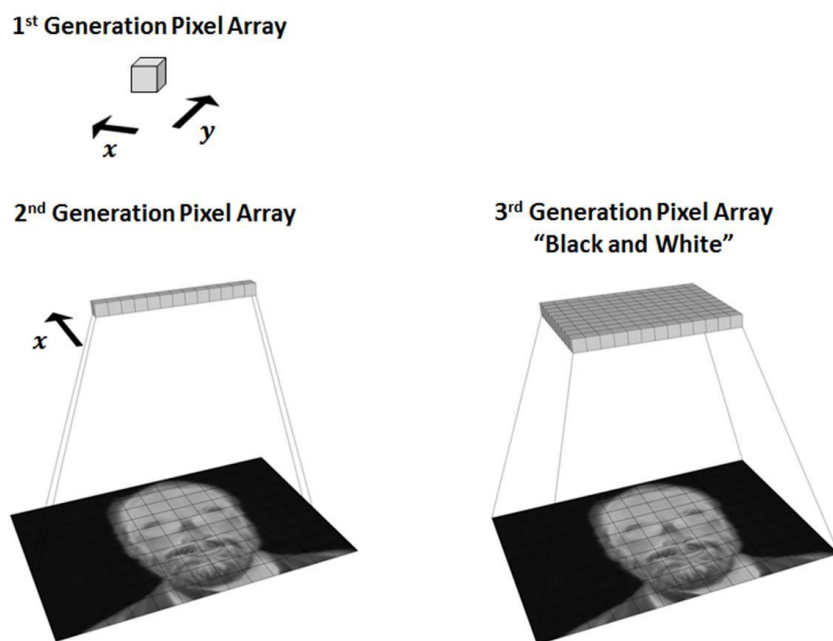


Figure 1.1: 1st, 2nd and 3rd Generation FPA Technology

Over the years infrared imaging technology has improved significantly and many new applications, such as multicolor infrared imaging, thermal medical diagnostics, and remote sensing have emerged [1]. This growth has been made possible by dramatic technical

advances in infrared sensor manufacturing as well as remarkable improvements in algorithms for image recognition, analysis and processing. However, because of the use of traditional system implementation, these existing image processing systems are far from being efficient.

Traditional imaging systems often utilize a complex network of external optics and computer algorithms for “advanced” image processing. For example, current imagers utilize mechanical filter wheels and dichroic filters to select a region of the infrared spectrum where a series of beam splitters and lenses guide the incoming radiation to one or more focal plane arrays (FPAs) for hyperspectral imaging [2]. Traditional systems are characterized by temporal and spatial registration problems which are costly, large, and complex. In addition, in this system, the readout integrated circuit (ROIC) transmits raw data to an external memory unit, where it can be processed externally by a central processing unit for image classification. Although the classified processed data is very compressed, the readout circuit has to transmit excessive amounts of raw data to the external memory unit. This requires a very high bandwidth data transmission channel, which unnecessarily consumes a large amount of the system’s power. Moreover, the external data processing unit adds extra latency in producing the final classified image. This system is shown in Figure 1.2a. Instead, Figure 1.2b shows an ideal imaging system for classification.

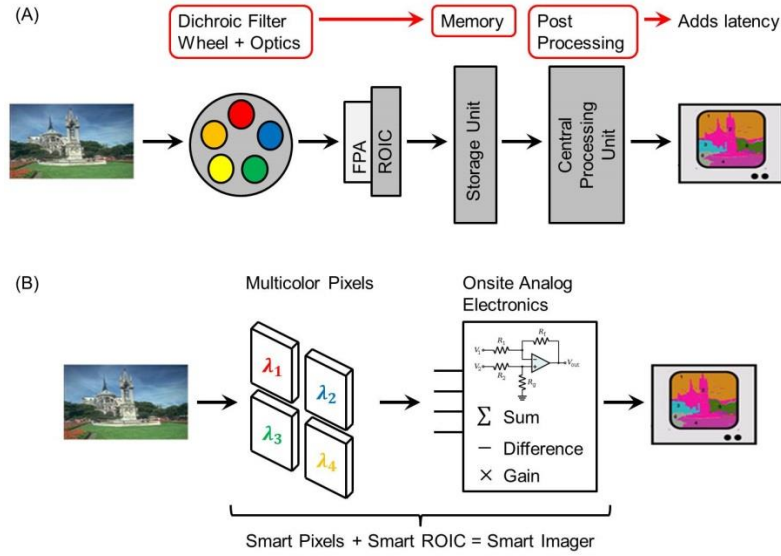


Figure 1.2: (A) A typical imaging system versus (B) an ideal imaging system for the classification of objects

In this *smart, 4th generation imaging system*, the data processing is performed directly on each pixel with the aid of onsite analog electronics for mathematical operations. As a result, the compressed and classified image data can be produced instantaneously and efficiently with similar function to the inner retina of the human eye [3]. This will offer tremendous opportunities for the on-sensor implementation of powerful image analysis and processing algorithms, which would not have been possible using existing imaging systems. Unlike conventional ROICs whose task is to simply read the pixels and send their raw outputs serially to a computer port, a smart infrared imager can also control the operating condition of each detector and process its data based upon prescribed algorithms on the pixel level. In addition, the use of pixel-integrated resonators for enhanced spectral sensitivity can also increase the efficiency of the detector significantly. Under precise design conditions, pixel-integrated resonators can increase the amount of incoming radiation absorbed in the active region of a photodetector for an improved signal-to-noise ratio.

1.2 Prior Multicolor Detector Art

Most present day sensors are single or broadband color detectors that monitor the emission from a given scene. However, there have been attempts to make two-color detectors on the pixel level. In contrast to single color or broadband IR sensors, two-color imaging provides several advantages like remote absolute temperature measurement, operation in a wide range of ambient conditions, chemical analysis and spectral discrimination of unique object features.

Recently, multicolor HgCdTe (MCT) FPAs have been demonstrated for both sequential mode and simultaneous mode operation [4-5]. The cross-section schematic of a sequential mode (or bias-selectable) backside illuminated FPA, shown in Figure 1.3a, is formed by two co-located detectors, with the long-wavelength infrared (LWIR) photodetector grown on the top of the mid-wavelength infrared (MWIR) photodetector. In such a device, the bottom (MWIR) photodetector serves as a longwave-pass filter for the top (LWIR) photodetector. For FPA polarity shown in Figure 1.3a, the operation is performed as follows: with positive bias voltage applied to the bump contact, the top (LWIR) detector is reverse biased and the bottom (MWIR) detector is forward biased. The MWIR photocurrent is shunted by the low resistance of the forward biased MWIR photodetector so that only LWIR photocurrent emerges in the external circuit. With negative polarity of applied bias, the situation reverses; only MWIR current is available in the external circuit. Since bias-selectable FPAs require a single indium bump per pixel, they are compatible with commercially available silicon read-out integration circuits (ROICs). However, design of sequential-mode FPAs does not allow independent selection of the optimum bias voltage for each photodetector thereby the probability of MWIR crosstalk in LWIR detector is large.

The cross-section schematic of simultaneous mode backside illuminated FPA is shown in the Figure 1.3b.

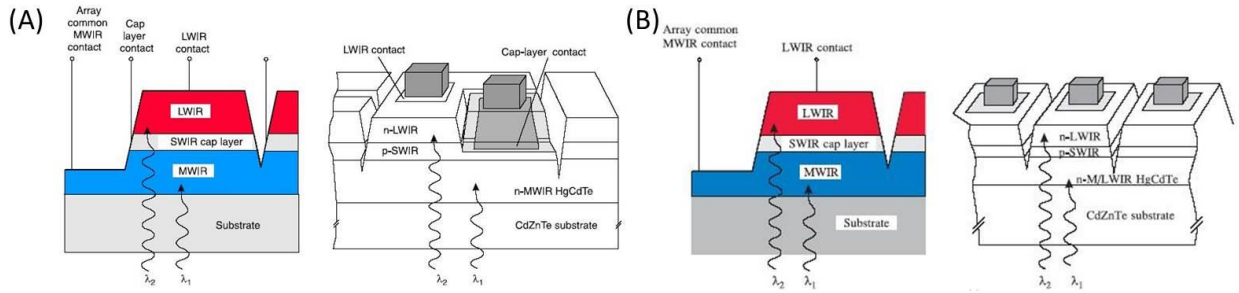


Figure 1.3: Schematic of a two color MW/LWIR MCT FPA with (A) sequential and (B) simultaneous mode operation

Simultaneous detection in the two spectral bands requires an additional electrical contact and, consequently, the second readout circuit in each unit cell. Difficulties in the epitaxial growth of MCT, need for a constant effusion cell temperature feedback and control, and non-uniform dopant incorporation adversely affect the development of multispectral cameras based on MCT.

Two color QWIP FPAs for LWIR/LWIR, MWIR/LWIR, near IR (NIR)/LWIR and MWIR/MWIR were developed by Sanders [6]. Since then, the two color QWIP FPA has had significant efforts focused on increasing the size and improving the performance [7-8]. An FPA that is capable of simultaneously detecting two separate wavelengths is fabricated by vertically stacking two QWIP layers during epitaxial growth. The photosensitive multi-quantum-well (MQW) region of each QWIP device is transparent at other wavelengths. Thus, the optical crosstalk between neighboring bands is negligible. Each QWIP simultaneously has bias voltages applied through the heavily doped contact layers that separate the MQW regions. For dual-band QWIP FPAs usually the three bumps per pixel

technology is used. Figure 1.4 presents the schematic of a dual-band MW/LWIR QWIP device with independent access to the MWIR and LWIR detectors.

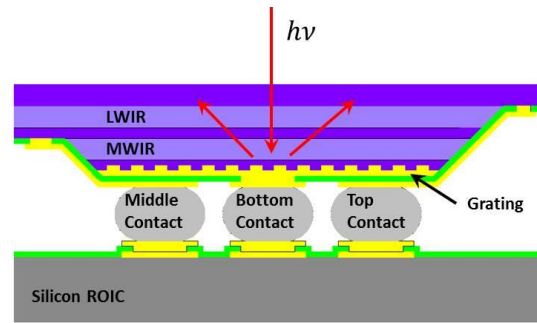


Figure 1.4: Schematic of two color MW/LWIR QWIP FPA

However, due to polarization sensitivity of absorption, most QWIP arrays use two-dimensional (2D) gratings for light coupling. The efficiency of the grating is lower for smaller pixel sizes because smaller pixels allow a smaller number of grating elements. Low temperature operation ($<70\text{K}$) is still an issue for multicolor QWIP FPAs due to the fundamental limitations associated with intersubband transitions [9].

Modern dual-color (MWIR/MWIR and LWIR/LWIR) Type II superlattice (T2-SL) cameras are a vertical detector based on two “back-to-back” InAs/GaSb T2-SL photodetectors separated by a common ground contact layer [10-12]. The absorption region for higher energy photons (“blue channel”) is formed by an InAs/GaSb T2-SL with a wider bandgap than the absorption region for the lower energy photons (“red channel”). Since the thickness of the entire structure is lower than a typical multicolor MCT FPA ($15\mu\text{m}$), the technological aspect of a T2-SL FPA is simplified. Figure 1.5 shows a SEM picture of a processed InAs/GaSb T2-SL dual-color (MWIR/MWIR) FPA and sample image delivered by the same camera.

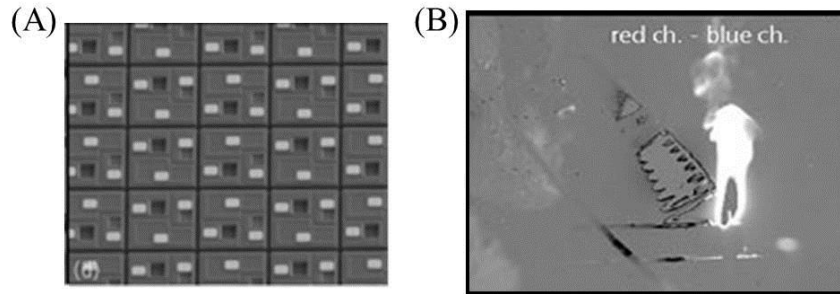


Figure 1.5: (A) Dual-color InAs/GaSb SL FPA and (B) captured image for the detection of carbon dioxide

The existing multi-spectral T2-SL technology has several limitations. First, in order to improve the signal to noise ratio of a bi-color FPA, the MWIR and, especially, the LWIR photodetectors need to be passivated. Second, the presented dual-color T2-SL FPA requires three indium bump contacts per pixel. These issues can lead to a complicated processing scheme and expensive read-out circuits.

1.3 New Research Thrust

The main objective of this research initiative is to design and demonstrate a multispectral, high quantum efficiency infrared detector. The spectral response of an individual pixel can be tuned to individual colors for pixel-level image processing at the sensor and within the ROIC, thereby enabling the sensor to output “compressed and important information” directly. An advanced application, for example, can incorporate custom spectral filters that are tuned to the spectral response or “fingerprint” of an object on the pixel-level, as illustrated in Figure 1.6 for the classification of granite rock.

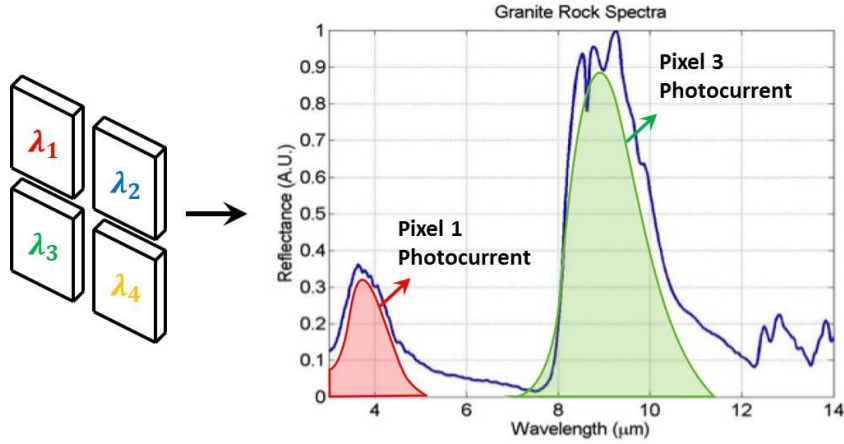


Figure 1.6: Example of smart pixels with their colors tuned to the spectral response of granite

This new “spectral fingerprinting” technology will enable the user to target desired objects in an unknown environment instantaneously because those objects will appear brighter than their background.

To design a multispectral detector with enhanced quantum efficiency, we utilize an emerging new class of metamaterials, the metamaterial absorber (MMA), hybridized with an infrared photodetector. A metamaterial is an electromagnetic structure that is much smaller than the wavelength of interest that can exhibit electromagnetic properties not generally found in nature. Due to their inherent design flexibility, MMs have been demonstrated over a range that spans several orders of magnitude in frequency from radio frequencies (RFs) [13] to mm-wave [14], far infrared (FIR) [15], mid-infrared (MIR) [16-17], near infrared (NIR) [18-19] and optical wavelengths [20-22]. Metamaterial absorbers have sparked significant interest since their first demonstration [23-24] and hold great potential for use in applications ranging from thermal emitters [25] and energy harvesting [26], to sensors and spatial light modulators [27]. As a result of this new engineering degree of freedom, a

metamaterial absorber hybridized with an infrared photodetector has the potential to significantly enhance infrared photodetectors on the pixel level for improved system functionality. For example, metamaterial absorbers can be designed as impedance matching layers for eliminating surface reflection and increasing received signal to the photodetector. In addition, dynamic metamaterials can be thought of as a spinning-wheel spectral filter, albeit with highly overlapping spectral bands, that can be used for panchromatic imagery, multi-color imagery at arbitrary wavelengths, multispectral imagery with arbitrary numbers, locations, and widths of spectral bands, and coarse resolution hyperspectral imagery.

1.4 Contribution and Organization of This Work

The author of this work has been involved in numerous projects with infrared and terahertz imaging technology. Contributions have been made with regards to characterization of materials, fabrication of detectors, and characterization of detectors. He has co-authored work concerning quantum well infrared photodetectors (QWIP) [27], quantum dots-in-a-well (DWELL) detectors [28-31], MWIR Type II SL interband cascade detectors (ICD) [32-35], and dynamic terahertz metamaterials for compressive sensing [36-39]. More specifically, contributions by this author can be regarded in the following list:

1. First to establish a novel metamaterial photodetector design scheme for impedance matching to free space and quantum efficiency enhancement.
2. First to fabricate a metamaterial photodetector test chip with ultra thin semiconductor contacts for improved optical mode overlap with the active region of a photodetector.
3. First to demonstrate a multicolor metamaterial absorber hybridized with a QWIP and T2-SL ICD infrared photodetector. The T2-SL ICD showed 7 x quantum efficiency enhancement.

4. First to identify useful absorption versus non-useful absorption experimentally for a metamaterial photodetector and metamaterial absorber
5. First to show an all electronic, multicolor dynamic metamaterial absorber. This dynamic metamaterial absorber was used to demonstrate the first metamaterial compressive imager in the terahertz regime.

In this dissertation, we examine both a QWIP and ICD detector hybridized with a metamaterial absorber for multicolor signal enhancement in the infrared regime. We also explore dynamic multicolor metamaterials in the terahertz regime with electronically tunable gain. In Chapter 2, we discuss QWIP and ICD photodetectors used for the fabrication of a metamaterial photodetector and methods for their experimental characterization. In Chapter 3, we present a rigorous computational study that investigates the hybridization of a metamaterial absorber with an infrared photodetector for impedance matching to free space. Chapter 4 presents the fabrication of a conventional FPA, its transformation into a prototype test chip for the characterization of metamaterial devices, and an in-depth (patent pending) discussion on the fabrication of a metamaterial FPA on the wafer level. In Chapter 5, we experimentally analyze a QWIP photodetector in a metamaterial absorber cavity and discuss its design limitations for quantum efficiency enhancement. In Chapter 6, we incorporate design lessons from the QWIP metamaterial detector and design, fabricate and demonstrate the first deep-subwavelength multispectral infrared detector using an ultra-thin T2-SL detector coupled with a metamaterial absorber with high quantum efficiency. We also identify useful versus non-useful absorption through a combination of absolute absorption and quantum efficiency measurements. In Chapter 7, we demonstrate a spatial light modulator (SLM) with multicolor super-pixels composed of arrays of electronically

controlled terahertz (THz) MMAs. The device created here shows that fundamental light interactions of surfaces can be electronically controlled and provides a path forward for future designs. In Chapter 8, we summarize the achievements of the research presented and discuss future directions of this work.

1.5 Summary

The following innovations are enabled by metamaterial absorbers in this research effort for its application in an infrared imaging system:

1. The incoming signal to the photodetector is significantly enhanced due to the resonant nature of a metamaterial based cavity.
2. Individual pixels in a FPA can contain a subset of fundamental “colors” that are enabled through metamaterial patterns on each pixel for identifying spectral features in a scene. An advanced design, for example, can encode the spectral fingerprint of an object.
3. Pixel-level processing at the sensor and within the ROIC on each pixel would enable high-performance processing inside the *smart imager* hardware, thereby enabling the sensor to output “compressed and important information” directly.
4. By adding basic image processing capability on the pixel level, a lower system size and cost should result.

Metamaterials offer a new engineering degree of freedom that has yet to be explored in the infrared photodetector community.

Chapter 2 : Materials and Methods

In this chapter, we discuss infrared photodetectors used for the fabrication of a metamaterial photodetector and their experimental measurement. This discussion should provide some broad perspective between classical photodetectors with low quantum efficiency and new material systems that operate at high operating temperatures. These photodetectors include Quantum Well Infrared Photodetectors (QWIPs) and Type II Superlattice (T2-SL) detectors with each category having advantages and disadvantages. QWIPs suffer from low quantum efficiency, with values typically less than 10%. In addition, they require diffraction gratings since normal incidence absorption is prevented by quantum selection rules. T2-SL detectors have shown promising results as a competing technology, with good spatial uniformity and higher operating temperature compared to HgCdTe (MCT), which is the dominant IR detector technology. Theoretically, T2-SL based detectors should outperform MCT based detectors. However, T2-SL detectors have not yet experimentally achieved its potential in terms of dark current or quantum efficiency. Although there are many areas for improvement for each type of infrared detector in terms of growth and fabrication processes, the quantum efficiency and signal-to-noise ratio of detectors can be greatly improved.

2.1 Dark Current

Dark current is one of the most important parameters which limit the performance of IR photodetectors. Dark current is the current that flows in a biased detector in the absence of IR radiation. Dark current is the main limiting factor of a detector's performance at higher operating temperatures. As a result, detectors have to be cooled in the range of 50-77K to reduce dark current, resulting in expensive commercial photodetectors with large cooling systems. Here, we discuss how dark current is experimentally determined. As illustrated in

Figure 2.1, a dark current measurement is performed by mounting a photodetector sample in a cryostat and cooling it to a desired temperature. A source-measure-unit (SMU) is then connected to the top and bottom contacts of the photodetector. The SMU is programmed to apply a bias and to measure the current passing through the device so that a current versus voltage curve results. Data from the SMU is captured with a computer with data acquisition software, like Labview.

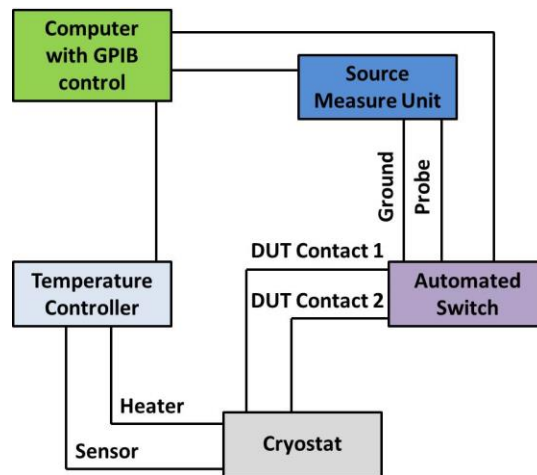


Figure 2.1: Voltage versus current measurement setup for infrared photodetector dark current measurements

Dark current is often measured at different temperatures because current-versus-voltage curves can provide clues into the detectors limiting dark current mechanism, such as Shockley-Read-Hall (SRH), diffusion, or tunneling (see Figure 2.2) dark current. Different dark current mechanisms have different temperature dependencies, so by collecting dark current data as a function of temperature, these various mechanisms can be determined by fitting a dark current model to them.

Perhaps the most straightforward method to determine the mechanism behind a particular photodetectors dark current is by creating an Arrhenius plot. An Arrhenius plot is

simply a plot of dark current as a function of temperature. However, the dark current, or vertical axis, is plotted on a log scale and the temperature, or horizontal axis, is plotted as an inverse. The inverse temperature scale can also include the Boltzmann factor “1/k” such that the axis becomes “1/kT” which will make the slope of the curve have the units of eV or energy. Plotting the dark current in this way is useful since it has an exponential dependence on temperature as indicated by the equation:

$$J \propto \exp\left(\frac{E_A}{kT}\right)$$

The slope of the curve is the activation energy, E_A , which can indicate the limiting current mechanism. For instance, if E_A is approximately equal to the band gap energy of the absorber material, diffusion dark current is the limiting mechanism. Diffusion current is the process where carriers move across a device as a result of carrier concentration gradients. If E_A is approximately half the band gap energy, then the limiting mechanism is Shockley-Read-Hall (SRH). SRH is a mechanism where carriers (electrons and holes) recombine or generate with the assistance of a trap near the center of the semiconductor band gap. If E_A is on the order of ten percent of the band gap energy, then the limiting mechanism tends to be tunneling or surface leakage current. Tunneling current is caused by carriers tunneling across a junction due to an applied bias and/or a built-in potential in the heterostructure. Tunneling current can take place directly through a band-to-band (BTB) process or indirectly with a trap-assisted-tunneling (TAT) process with the aid of an energy trap. Surface leakage currents result from defects on the sidewalls of the detector that provide paths for current to flow.

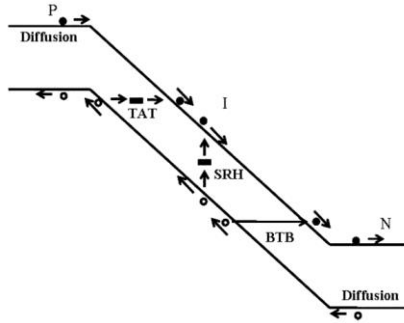


Figure 2.2: Illustration of SRH generation-recombination current, band to band tunneling current, and trap assisted tunneling current in a narrow bandgap PIN diode

2.2 Responsivity

Responsivity is defined as the ratio of an electrical output signal to an optical input signal or power and can be presented with the units of A/W or V/W. In general, the formula describing responsivity is as follows:

$$R_{\lambda} = \frac{G\eta\lambda}{hc}$$

where R_{λ} is the responsivity, G is the photoconductive gain, η is the quantum efficiency, λ is the wavelength, h is Planck's constant, and c is the speed of light. This definition is useful because it provides us with a relationship between responsivity and quantum efficiency. However, in order to experimentally determine the responsivity we have to make a carefully constructed measurement in which we measure the electrical signal of the detector in response to a calibrated optical source. This experiment is mathematically shown with the following formula:

$$R_{\lambda} = \frac{I}{A_{BB} \times \frac{A_{det}}{r^2} \times \int_0^{\lambda_{cut}} M_{e,\lambda}(\lambda, T) \times NR(\lambda) d\lambda}$$

where I is the current of the measured signal, A_{BB} is the area of the black body aperture, A_{det} is the detector aperture area, r is the distance between the detector and black body, λ_{cut} is the cut-off wavelength, $M_{e,\lambda}$ is the black body spectral exitance as a function of wavelength and temperature, and NR is the normalized spectral response as a function of wavelength of the detector being tested. The measurement, as illustrated in Figure 2.3, is performed by mounting the detector being tested in a cryostat and cooling it to a desired temperature. A calibrated black body source is placed in front of the detector and set at some temperature. An optical chopper is placed between the detector and the black body source and set to some frequency. This is done in order to isolate the detector signal, due to the black body, from the background signal, due to ambient room conditions. The signal from the detector is fed through a voltage amplifier to a network analyzer or lock-in amplifier where the signal is recorded.

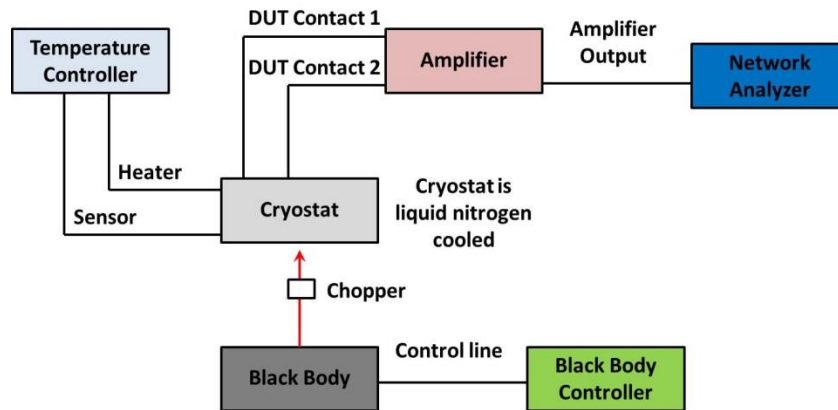


Figure 2.3: Responsivity measurement setup to determine an electrical output signal to an optical input signal ratio

2.3 Electrical Noise

Noise measurements are conducted in similar fashion to responsivity measurements (see Figure 2.4). The sample is mounted in a cryostat and cooled to some desired temperature. The device under test is then connected to a voltage amplifier in which a voltage can be applied across it. The signal from the amplifier is fed to a network analyzer where the signal is measured. The frequency on the network analyzer is varied such that you can produce noise measurements as a function of frequency and it allows one to potentially investigate such characteristics as $1/f$ noise. Spikes in the measurement may be present due to noise from the system or building electricity so care must be taken to avoid those frequencies. Such frequencies are quite apparent due to them being located every 60 Hz. The noise of the detector can be measured as a response to the room temperature background or due to some other source such as well controlled black body. It is very important that the field of view and background is known since both those parameters will affect the noise magnitude. As an additional comment, it is noted that noise measurements are very difficult to accurately measure due to a variety of factors especially the presence of noise in the measurement system itself. Some research facilities even incorporate amplifiers that are cooled in the cryostat with the detector in order to reduce such noise sources.

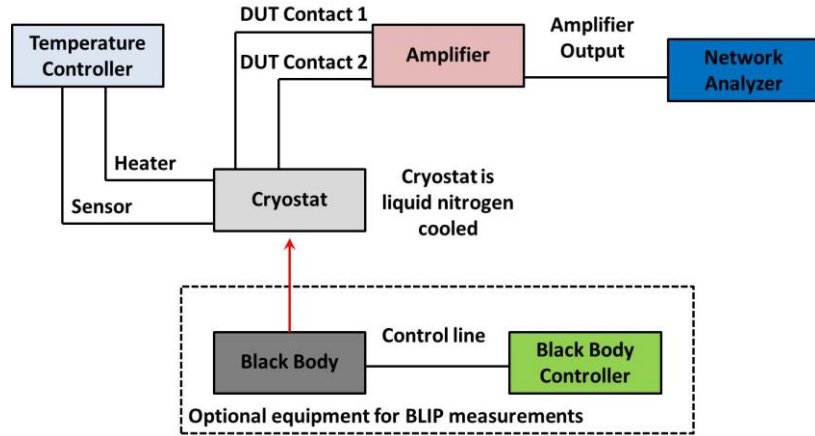


Figure 2.4: Noise measurement setup for the characterization of infrared photodetectors

2.4 Specific Detectivity

Specific Detectivity can be interpreted as the signal-to-noise ratio (SNR) of a detector when 1W of radiant power is incident on a detector, with an area equal to 1 cm² and noise equivalent bandwidth of 1 Hz. Units of specific detectivity are Jones (cm Hz^{1/2}/Watt). The detectivity for a double pass of radiation for a photodetector is as follows:

$$D^* = 0.31 \frac{\lambda}{hc} k \frac{\eta}{\sqrt{t}}$$

where $1 \leq k \leq 2$ depends on the contribution of recombination and backside reflection. The ratio of absorption efficiency to the thermal generation rate determines the detectivity limits of the device. Specific detectivity is calculated from responsivity and noise. The responsivity is determined by measuring the response signal of a given detector with reference to a calibrated blackbody source. The noise can be determined by either estimating it from DC current measurements or measuring it directly. Estimating noise from current measurements is often done due to the relative ease of the current-voltage measurement. However, it lacks certainty in its value due possible missing noise sources. Measuring noise

directly may be more reliable in terms of the noise or detectivity value produced, however, direct noise measurements are difficult to conduct due to various noise sources in a measurement setup. The formula for calculating specific detectivity from direct noise measurements is shown below:

$$D^* = \frac{R_\lambda \sqrt{A \Delta f}}{i_{noise}} = \frac{\sqrt{A \Delta f}}{NEP}$$

where R_λ represents responsivity, A is the detector area, Δf is the measurement bandwidth, i_{noise} is the noise current from the measurement, and NEP is the noise equivalent power which is defined as the ratio of the noise and the responsivity as indicated in the equation. Measuring the noise directly requires the use of the device in question mounted in a cryostat cooled to a desired temperature, a pre-amplifier, and a network analyzer or lock-in amplifier. In addition, the field of view of the device during the measurement must be known and presented with the results since it will affect the specific detectivity value. The formula for calculating the specific detectivity using current-voltage measurements is shown below:

$$D^* = \frac{R_\lambda}{\sqrt{2qJ + 4kT/R_D A}}$$

where q is the charge of an electron, J is the dark current density for a given bias, k is Boltzmann's constant, T is temperature, and R_D is the dynamic resistance, which is calculated by determining the inverse of the slope of the current-voltage curve at a given bias. This method generally overestimates the specific detectivity, so the theoretical background limited (BLIP) detectivity is also presented as a performance metric.

2.5 Quantum Efficiency

Incident radiation can excite an electron-hole pair. Under the presence of an electric field, electrons and holes are collected to produce a photocurrent. Quantum efficiency (QE) is a measure of the number of photons that result in collected photocurrent versus the total number of photons that strike the photodetector. In other words, it is an accurate measurement of the device's electrical sensitivity to light. Since the energy of a photon depends on its wavelength, QE is often measured over a range of different wavelengths.

$$\eta = \frac{N_e}{N_v} = \frac{R_\lambda hc}{G\lambda}$$

where N_e is number of electrons produced and N_v is number of incident photons.

2.6 Absolute Absorption Measurement

A Thermo Scientific iN10MX infrared microscope is used to measure the reflectance of a metamaterial photodetector to determine the amount of incoming radiation absorbed. A transmission measurement is not necessary because we incorporate a thick metal ground plane in our metamaterial photodetectors. A measurement is performed by cooling down the sample to 77K with a Linkam cooling stage that is designed to work with an infrared microscope. The Linkam cooling stage incorporates potassium bromide windows for transmission of infrared radiation to the sample. The reflectance of each pixel is measured to calculate the metamaterial photodetectors absolute absorption response. This absolute absorption response occurs due to losses in the metal, contact layers, and active region of the photodetector.

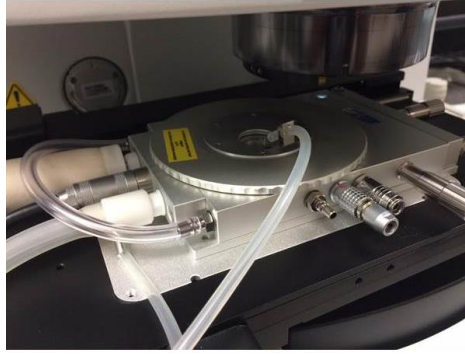


Figure 2.5: Absolute absorption measurement of a photodetector with an infrared microscope

2.7 Quantum Well Infrared Photodetectors (QWIPs)

QWIP infrared detectors use intersubband transitions in hetero-engineered structures. QWIPs are based on III-V material systems with the most common material system being AlGaAs/GaAs. A QWIP produces photocurrent when an electron at a discrete energy level in a quantum well is excited to a continuum or quasi-bound state by incoming photons. An applied voltage is typically applied to a quantum well to sweep excited electrons and holes to their respective contacts. The number and location of discrete energy states in a well can be tuned by varying the width of the well (GaAs) and depth of its barriers ($\text{Al}_x\text{Ga}_{1-x}\text{As}$). A schematic diagram of a GaAs/AlGaAs QWIP is shown in Figure 2.6.

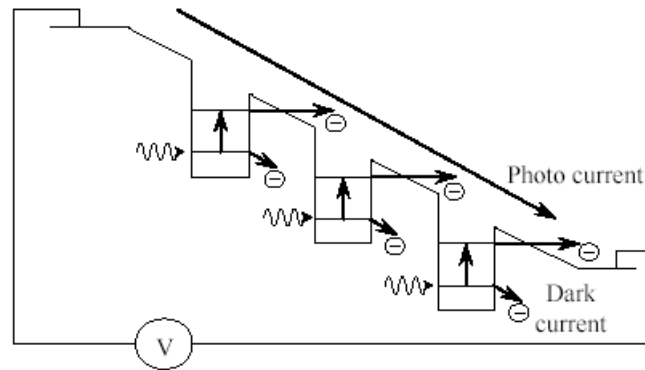


Figure 2.6: Schematic diagram of GaAs/AlGaAs QWIP

GaAs/AlGaAs QWIPs have the following advantages:

- Use of standard manufacturing techniques based on mature GaAs growth and processing techniques
- Highly uniform and well-controlled MBE growth
- GaAs wafers are low in cost, and have high thermal stability

However, QWIP detectors suffer from low quantum efficiency due to high values of thermally generated dark current generated by electrons tunneling between wells. Due to intersubband transitions in QWIPs, long-wavelength infrared photodetection is limited to lower operating temperatures. In addition, the quantum efficiency of a QWIP is limited to off-angle incident light due to absorption selection rules. Although this limitation is usually overcome by incorporating a diffraction grating on the detector surface, the quantum efficiency of a QWIP remains insufficient (typically less than 10%).

2.7.1 Dark Current in QWIPs

Electrons are typically confined to the growth direction of a quantum well. Taking the z-axis as the growth direction, electrons are free to move across the x-y plane. These electrons have

a higher energy than the ground state (E_o) of the quantum well and contribute to three predominant dark current mechanisms.

1. Ground state tunneling
2. Thermally assisted tunneling
3. Thermionic emission

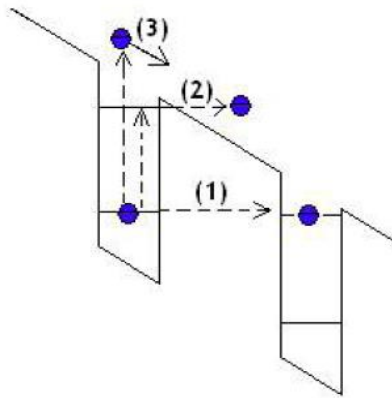


Figure 2.7: Three dark current mechanisms in an inter-sub-band photodetector: 1-ground state tunneling, 2-thermally assisted tunneling and 3-thermionic emission.

Ground state tunneling occurs when electrons in the ground state move through the barrier into neighboring quantum wells. To overcome this tunneling effect, thick barriers, in the range of 25-50nm, are used between quantum wells. However, the thickness of the barriers should be smaller than a critical growth thickness for a practical material system; otherwise built-in strain due to lattice mismatch will result with poor sample quality. Another form of dark current occurs when a low energy electron is thermally excited and tunneled out of the quantum well. Thermally assisted tunneling is considered a major source of dark current. To overcome this effect, bias voltage and the tunneling barriers must be optimized. Finally, when the electrons get thermally excited out of the well into the continuum, thermionic

emission takes place. To calculate the actual dark current density flowing through a biased detector, we need to calculate the current density produced by the thermionic emission, J_{em} , as well as the reduction in the photocurrent caused by the trapping of electrons, J_{trap} , into the neighboring well. Under steady-state conditions, both current densities are approximately equal. The total dark current density can be calculated from the following relation:

$$J_{dark} = \frac{J_{em}}{p}$$

where p is the trapping probability for an electron traversing a potential well. The trapping probability can be expressed as:

$$p = \frac{\tau_{transit}}{\tau_{transit} + \tau_{life}}$$

Here $\tau_{transit}$ and τ_{life} are transition time and lifetime of the electrons in a quantum well.

2.8 Type-II Superlattice Photodetectors

The InAs/GaSb SL material system was first proposed as an IR sensing material in 1977 by Tsu, Sai-Halaszi and Esaki [40]. IR detectors based on InAs/(In,Ga)Sb SL have been investigated for the past 30 years, ever since they were proposed by Smith and Malhiot for infrared detection [41]. In 1990, Chow and co-workers first reported Ga_{1-x}In_xSb/InAs superlattice materials with high structural quality, LWIR photoresponse, and LWIR photoluminescence [42]. While theoretical predictions seem to favor the InAs/InGaSb system due to the additional strain provided by the InGaSb layer, most of the experimental results in the past five years have been on the binary InAs/GaSb system. It is attributed to the critical thickness limitations imposed upon strained material during the growth of In_xGa_{1-x}Sb layers with a large mole fraction of In.

InAs/GaSb SL material is characterized by the broken-gap type-II alignment, with electrons and holes localized in InAs and GaSb layers, respectively. The overlap of electron (hole) wave functions between adjacent InAs (GaSb) layers results in the formation of electron (hole) minibands in the conduction (valence) band. Optical transition between the highest hole (heavy-hole) and the lowest conduction miniband is employed for the detection of incoming IR radiation. The effective bandgap of the InAs/ (In,Ga)Sb SLs can be tailored from 3 μm to 30 μm by varying the thickness of constituent layers thus allowing fabrication of devices with operating wavelengths spanning the entire IR region. By controlling the strain at the interfaces, extremely thick ($\sim 6 \mu\text{m}$) active regions can be grown resulting in a large quantum efficiency and responsivity [43]. Tunneling currents in a SL are reduced due to a large electron effective mass. Large splitting between heavy-hole and light-hole valence subbands due to strain in the SL contributes to the suppression of Auger recombination [44]. The strain layer superlattice (SLS) material system is less sensitive to bandgap variations due to compositional non-uniformities compared to MCT alloys with the same bandgap [45]. Commercial availability of low defect density substrates and a high degree of uniformity for III-V processing over a large area also offers technological advantages for the SLS material system. Finally, in contrast with QWIPs, normal incidence absorption is permitted in SLSs, contributing to high quantum efficiency. InAs/GaSb SLSs have been widely used for making optoelectronic devices such as edge-emitting lasers and IR detectors operating in the mid-wave (MWIR, 3-5 μm) [46-48], long-wave (LWIR 8-12 μm) [49-51] and very long-wave (VLWIR, 12-32 μm) [52-53] IR regions. The band-engineering suppression of Auger recombination rates leads to improved temperature limits of spectral detectivities. Moreover, the commercial availability of substrates with good electro-optical homogeneity, and without

large cluster defects, also offers advantages for the T2SL technology. Even though this research effort is detector agnostic, we wanted to wisely choose a MWIR detector with the following metrics in mind:

1. The photodetector should have a broadband spectral response for the design of metamaterial pixels with multiple colors
2. The active region of the photodetector should have a large absorption coefficient
3. Electromagnetic losses in the metamaterial photodetector can be reduced if a gold Ohmic contact layer is used
4. The photodetector should be competitive with HgCdTe detectors in terms of fabrication and efficiency

2.8.1 Interband Quantum Cascade Photodetector

Although SL based photodetectors offer great potential for high temperature operation, like all detectors, their heterostructure design must be engineered to reduce dark current. Dark current in a T2-SL can be significantly reduced by incorporating a quantum cascade region in the photodetector. A higher operating temperature generally increases thermal generation and scattering rates which degrade both the electrical and optical performance of T2-SL photodetectors. Therefore, maintaining a reasonably high response (efficient photo-carrier extraction) and low noise at high operating temperatures (HOTs) is the primary research focus. For conventional IR photodetectors, the photo-carrier extraction process is dominated by the drift-diffusion process, which is highly dependent on the electric field distribution and carrier lifetime. Generally, the electric field distribution in a photodetector is determined by the device structure and operation bias. An increased bias could promote photo-carrier extraction, but will also introduce much unwanted shot noise. In MWIR T2-SL materials, the

Shockley-Read-Hall (SRH) lifetime will decrease to a few tens of nano-seconds at higher operating temperatures, which will also drastically increase thermal noise and affect the photo-carrier extraction, making it very challenging to obtain HOT operation for T2-SL.

One way to overcome these issues in T2-SL detectors is to use an interband cascade (IC) photodetector architecture for carrier transport in series with an absorber region. Similar to a multi-junction design, which is widely adopted in high efficiency photovoltaic solar cells, the IC structure is comprised of multiple stages (each stage contains a moderately thin absorber) electrically connected in series. This allows us to slice the absorber into relatively thin segments. Unipolar barriers, which block the majority carriers without blocking the photo-generated carrier transport, are placed at each side of the thin absorbers. Due to the much shorter transport distance, the photo-carriers generated in these thin absorbers can be efficiently collected, even at very high operating temperatures where the diffusion length is greatly reduced. Furthermore, an ultra-fast (*sub-ps*) photo-generated carrier extraction channel – longitudinal optical (LO) photon assisted inter-subband relaxation, is utilized to provide very efficient photo-carrier transport. This is achieved by carefully constructing an electron stair-case energy ladder in the conduction band of the electron relaxation regions. The device operation is shown in the schematic drawing of IC detectors in Figure 2.8.

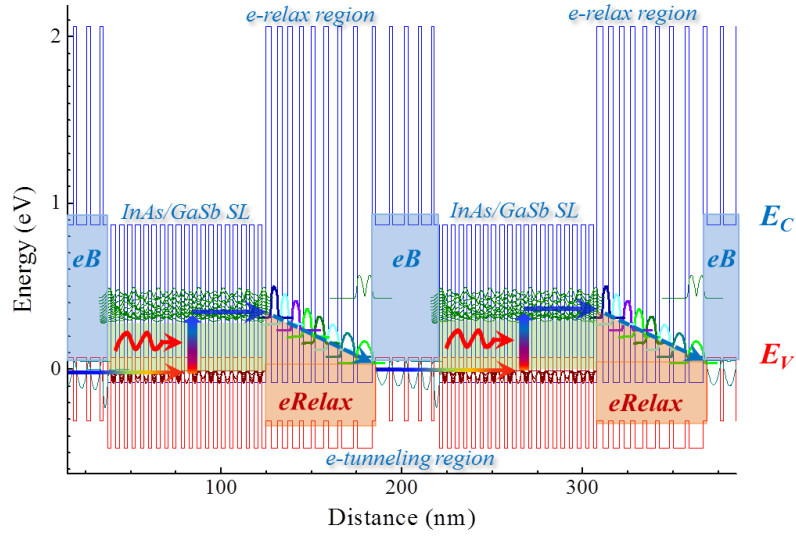


Figure 2.8: Band structure diagram in (two stages of) interband cascade photodetectors. The transport of carriers is shown by arrows. The incoming photons are absorbed in the InAs/GaSb T2-SL absorbers, generating electron-hole pairs. The electrons will diffuse into the electron relaxation region, and then effectively transport into the valence band of the next stage, through fast LO-phonon assist intraband relaxation and interband tunneling.

Unlike conventional multi-junction devices, where carrier transport between junctions/stages are realized by interband tunneling in highly doped P-N junctions, interband cascade detectors take advantage of the inherent type-II broken-gap alignment in the “6.1-Å-family” material system. In interband cascade detectors, each cascade stage is composed of three regions. The first region is a finite T2-SL absorber region in which photo-excited carriers are generated; the second region is an electron relaxation (eR) region, which allows the photo-generated electrons to efficiently pass through via LO-phonon assisted fast relaxation; and the third region is an electron tunneling (eT) region which presents an electron barrier (eB) in the conduction band and in the meantime enables the electron to tunnel into the valence band of the next stage via interband tunneling. The eR region is

composed of carefully engineered coupled multiple-quantum-wells (MQWs), such that a series of stair-case energy ladders is formed in the conduction band, and the energy separations are close to an LO phonon energy. As mentioned earlier, a type-II broken-gap band alignment, between the eR region (in this stage) and eT (in the next stage) is adopted. Such a broken-gap design facilitates a fast carrier relaxation path for photo-generated electrons, leading to very efficient collection of photo-generated carriers.

2.9 Summary

This chapter discussed detection figures of merit and methods used to characterize an infrared photodetector. Also, QWIPs and T2-SL detectors were discussed and some of their advantages and disadvantages were highlighted. We also reviewed the operation and design of a QWIP detector and noted their inability to absorb normally incident infrared radiation due to quantum selection rules. In addition, QWIP detectors suffer from large dark current due to poor carrier confinement in the x-y plane, electrons have a higher energy than the ground state (E_o) of the quantum well and contribute to dark current mechanisms. We also examined T2-SL for high temperature operation. T2-SL detectors have shown promising results as a competing technology, with good spatial uniformity and higher operating temperature compared to MCT. In addition, the performance of a T2-SL can be significantly improved by incorporating a quantum cascade region in series with the SL for room temperature operation in the MWIR part of the spectrum. This discussion should provide some broad perspective between classical photodetectors with low quantum efficiency and new material systems that operate at high operating temperatures.

Chapter 3 : Metamaterial Photodetector Theory and Design

Infrared imagers require new technologies on the pixel level to provide enhanced spectral information. In this chapter, we introduce metamaterials as an electromagnetic design tool for enhancing the spectral response of a photodetector with enhanced quantum efficiency. As illustrated in Figure 3.1, a multicolor camera system can be accomplished by tuning individual pixels to a specific infrared “color” with the aid of metamaterial designs hybridized with an infrared photodetector. We also investigate impedance matching metamaterial photodetectors to free space and establish a design scheme through a series of electromagnetic simulations that can be applied to nearly any photodetector.

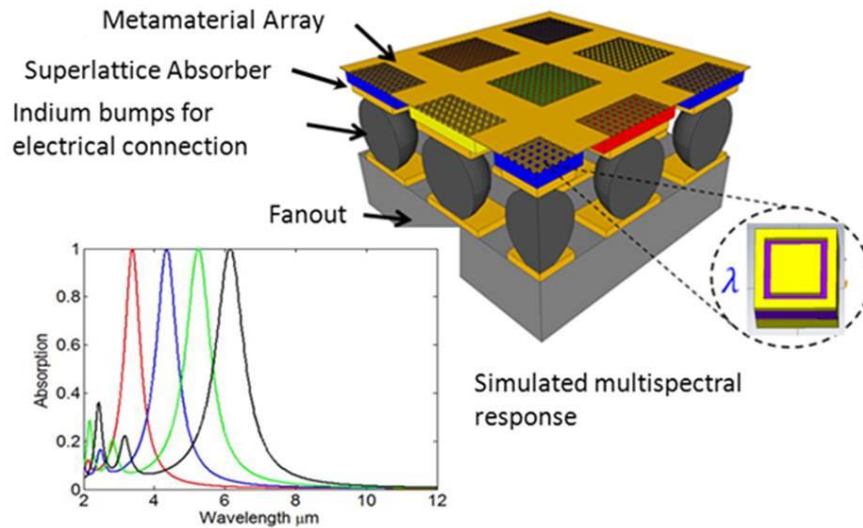


Figure 3.1: Illustration of a multicolor metamaterial photodetector

3.1 Overview of Metamaterials

Electromagnetic metamaterials can be regarded as an effective media with a complex electric permittivity $\epsilon(\omega)$ and magnetic permeability $\mu(\omega)$ that obtain their electromagnetic properties from their geometry and not solely from their constituent materials. Interest in metamaterials as a new electromagnetic engineering design tool has increased after their demonstration to

achieve negative index of refraction [54-56], invisibility cloaks [57], and perfect lensing [58, 59], which are not possible to achieve with naturally occurring materials. Metamaterial design theory enables a fundamentally new approach to control the flow of light. For example, natural dielectric materials are typically modeled as a mass-spring system where incoming radiation interacts with nucleus bound electrons to produce oscillating electric and/or magnetic dipole moments. These oscillating dipole moments, which are dependent on the materials atomic structure, are recognized as the cause for a materials dispersive behavior. As a result, the optical properties of a material for a desired application are restricted to the natural world. A metamaterial, on the other hand, is essentially an artificial atom that can provide a desired refractive index not typically found in nature. These artificial atoms are generally much smaller than the wavelength of interest and are composed of metal structures with similar behavior to an RLC circuit.

3.1.1 Effective Permeability

An artificial magnetic element possessing an effective magnetic permeability was first demonstrated by Pendry in his pioneering publication on conductors with magnetism in 1999 [60]. An artificial magnetic element can be thought of as an RLC resonator that induces a magnetic dipole at the resonance wavelength.

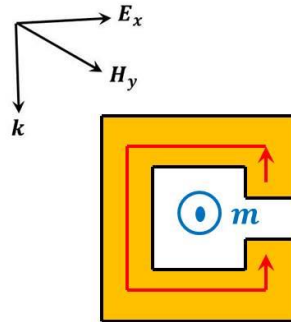


Figure 3.2: Illustration of a split-ring resonator at resonance

In order to explain the origins of magnetism for a SRR, it is desirable to derive permeability from fundamental electromagnetic theory. Circuit theory (in Faraday's form) for an artificial electromagnetic resonator is an exact solution if the elements within a circuit can be precisely defined and the individual elements are much smaller than the wavelength of interest so that the time dependent fields are homogeneous across the resonator [60]. As described in Pendry's pioneering paper, a time varying magnetic field perpendicularly incident on a split ring resonator can induce circulating currents according to Faraday's law.

$$\oint \mathbf{E} \cdot d\mathbf{l} = -\frac{d}{dt} \iint \mathbf{B} \cdot d\mathbf{S} = L \frac{dI}{dt} + \frac{1}{C} \int I dt + RI = -\frac{d\phi}{dt}$$

The magnetic flux ϕ through the surface S of the circuit will induce a circulating current I and a voltage drop across each element. The gap in the split ring resonator behaves like a capacitor that builds up charge. The metallic ring behaves as an inductor. Assuming the geometry of the resonator is within the quasi-static limit, the magnetic dipole of an individual unit cell is given by

$$m = SI$$

The sum of all "magnetic atoms" N per unit volume V leads to an overall magnetization

$$M = \frac{N}{V} m$$

The magnetic susceptibility that results is $\chi_{eff} = M/H$. Relating magnetic susceptibility to magnetic permeability, we obtain following relationship for an artificial medium.

$$\mu_r(\omega) = 1 + \frac{M}{H} = 1 + \frac{N_{LC}/V \mu_0 S^2 / L \omega^2}{1/LC - \omega^2 - j\omega R/L} = 1 + \frac{F\omega^2}{\omega_0^2 - \omega^2 - j\omega\gamma_\mu}$$

where F is the geometrical factor, ω_0 is the resonance frequency and γ_μ is the resistive damping factor.

3.1.2 Effective Permittivity

To achieve a metamaterial with negative refractive index, we require metamaterials with both negative permeability and permittivity at a desired wavelength [54-56]. As discussed earlier, the split ring resonator can be utilized to achieve negative permeability. Although Pendry also proposed negative permittivity with a 3-dimensinal grid of wires [61], a variation of the split ring resonator can be constructed to also achieve negative permittivity [62-63]. This structure, illustrated in Figure 3.3, is known as the electric split ring resonator (ESRR).

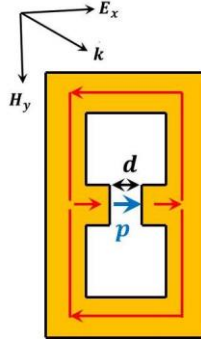


Figure 3.3: Illustration of an electric split-ring resonator at resonance

A time varying electric field parallel to the flow of current across the gap d can induce circulating currents. The induced magnetic flux through each loop produces magnetic dipoles that effectively cancel each other. In this way, the ESRR can only couple to incoming electric fields. Assuming the geometry of the resonator is within the quasi-static limit, an electric dipole is induced in the gap of the ESRR. As a result of this induced

electric dipole, the electric permittivity of the artificial medium is given by the following relationship.

$$\varepsilon_r(\omega) = \varepsilon_\infty + \frac{G\omega^2}{\omega_0^2 - \omega^2 - j\omega\gamma_\varepsilon}$$

where ε_∞ accounts for the frequency independent permittivity of the supporting dielectric substrate, G is the geometrical factor, ω_0 is the resonance frequency, and γ_ε is the resistive damping factor.

3.2 Metamaterial Absorber

The idea behind metamaterials is that they permit the construction of materials with a desired electric and magnetic response. By fabricating bilayer metamaterial structures it becomes possible to simultaneously tune $\varepsilon(\omega)$ and $\mu(\omega)$ for zero reflection. While typically it has been important to minimize losses in the metamaterial over the operating wavelength range, however, for some applications it is desirable to instead maximize loss and increase the devices absorptivity. The metamaterial perfect absorber takes advantage of the engineering flexibility of metamaterials to permit the construction of materials that are impedance matched to free space, thus minimizing the reflectance, and, at the same time, arranging the structure so that transmission goes to zero [64-65]. Such a metamaterial is shown in Figure 3.4 where a single periodic unit cell consists of three distinct elements: a metal cross, a dielectric layer, and a metal ground plane. The structure presented in Figure 3.4 was simulated using the commercial software CST Microwave Studio 2012. A time domain simulation was utilized and a Drude model was used to optically simulate gold with a plasma frequency $\omega_p = 2\pi \times 2175 \text{ THz}$ and collision frequency $\omega_c = 2\pi \times 18 \text{ THz}$. The permittivity of the dielectric layer is 13 with a loss tangent of 0.1. This structure achieves

perfect absorption with dimensions $a = 2\mu\text{m}$, $l = 1.5\mu\text{m}$, $w = 0.3\mu\text{m}$, and $t=0.4\mu\text{m}$. A simulated power loss density profile of the structure clearly shows that a majority of incoming radiation is lost in the dielectric layer.

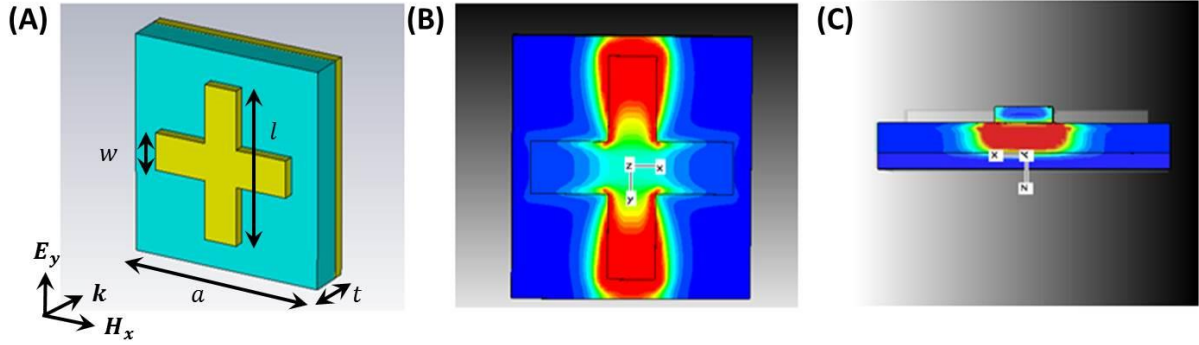


Figure 3.4: (A) Schematic of a MMA unit cell and its dimensions are $a = 2\mu\text{m}$, $l = 1.5\mu\text{m}$, $w = 0.3\mu\text{m}$, and $t=0.4\mu\text{m}$. Power loss density profile from (B) the top and (C) the side of the MMA with vertically polarized incoming radiation

The metamaterial perfect absorber can also be modeled with RLC circuit models to understand its electromagnetic behavior. For example, a time-varying magnetic flux penetrating the region between the metallic cross and the ground plane generates anti-parallel currents (inductance) that build up a charge at its dielectric gap (capacitance), resulting with an induced magnetic dipole for an effective $\mu(\omega)$ response. A second RLC circuit model can be used to define an effective permittivity $\varepsilon(\omega)$ response that occurs between metallic crosses and its neighbors. The array of crosses strongly couples to a time-varying electric field and results with a current along the length of the metal (inductance) and a charge builds up at the gap between neighboring crosses (capacitance), resulting with an induced electric dipole for an effective $\varepsilon(\omega)$ response. The resistive loss in the structure is due to the dispersive nature of the metal layers and losses in the dielectric layer. By tuning each of

these resonances, it is possible to impedance match the metamaterial absorber to free space for zero reflection and high absorptivity. The effective parameters for a metamaterial absorber with a cross pattern are calculated using the method proposed by Smith [66] in Figure 3.5 to demonstrate the relationship between magnetic and electric field coupling.

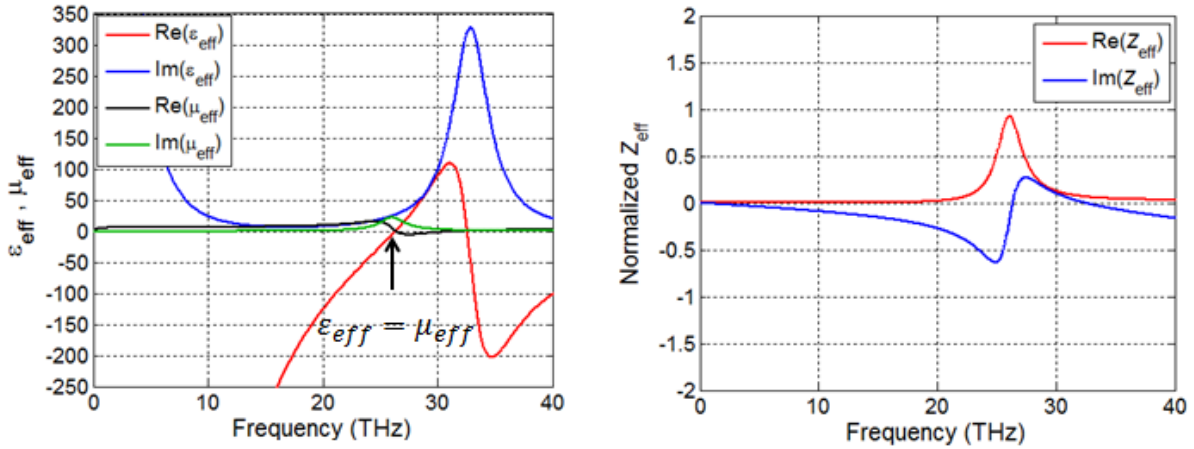


Figure 3.5: Calculated effective parameters for the proposed metamaterial absorber

3.3 Metamaterial Photodetector

In the design of a metamaterial photodetector, the absorption of all incoming radiation must be maximized to meet its full potential. Once maximized, we assume that a significant amount of this absorbed radiation is lost to the active region of our photodetector to enhance its optical response. The absolute absorption efficiency of a metamaterial photodetector is determined by the loss behavior of its encased materials with the active region dominating its overall behavior. If the absorption coefficient of the active region is too low or too high, a significant amount of reflection occurs, which reduces the amount of incoming radiation absorbed. To help the metamaterial photodetector achieve 100% absorption of all incoming radiation, the absorption coefficient of the active region must be critically tuned to a precise value that is defined by the metamaterial absorber geometry. However, the optical properties

of the encased materials are typically fixed and determining the optical properties of a heterostructure is not often a straightforward process because its 1) anisotropic 2) temperature dependent and 3) highly dependent on the growth conditions of an MBE. As a result, we present a design scheme where we tailor the metamaterials geometry until impedance matching to free space occurs with a given photodetector. In the remaining sections of this chapter, we demonstrate a metamaterial photodetector design scheme with a Type II superlattice (T2-SL) active region. We demonstrate this concept by first measuring the absorption coefficient of our T2-SL and then show that impedance matching to free space occurs when the geometry is precisely tailored to this measured absorption coefficient. Once this design scheme is demonstrated, one will see how this method can even be applied to a photodetector where the optical properties of the infrared photodetector are *not* entirely known. In this way, we can impedance match *any* infrared photodetector with a metamaterial absorber cavity to free space.

3.3.1 Absorption Coefficient Measurement

In this section, we measure the absorption coefficient of a thin 10-ML InAs / 10-ML GaSb T2-SL epitaxially grown on a GaSb substrate. On one half of this substrate, the superlattice layer is etched away so that this side of the substrate can serve as a reference layer for transmitted radiation. As shown in Figure 3.6 the sample is loaded into a liquid nitrogen cooled Dewar with infrared windows to allow transmission of radiation from a FTIR through the sample.

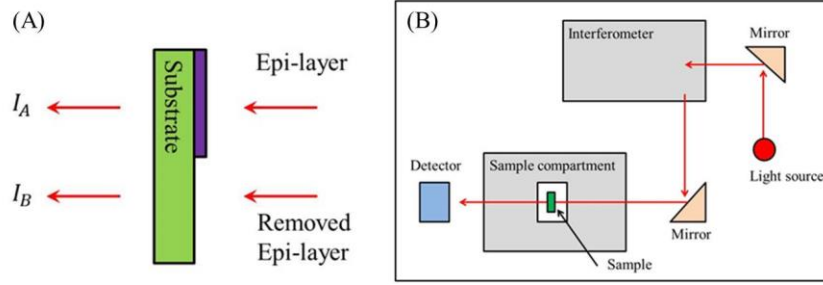


Figure 3.6: Experimental setup for measuring the absorption coefficient of an epi-layer

Before beginning any measurements, a background measurement is performed to remove any atmospheric effects from the measurement. Next, radiation is transmitted through the epitaxial side of the substrate and measured with a detector. This transmitted radiation I_A is described by the following equation:

$$I_A = I_0 e^{-\alpha_0 d_s - \alpha_e d_e}$$

where α_0 is the absorption coefficient of the substrate, d_s is the substrate thickness, α_e is the absorption coefficient of the epitaxial layer, d_e is the epitaxial layer thickness and I_0 is the initial intensity from the FTIR. The radiation I_B that passes through the substrate with the epitaxial layer removed is given by

$$I_B = I_0 e^{-\alpha_0 d_s}$$

If we know the thickness of the epitaxial layer and the amount of radiation transmitted from the epitaxial and non-epitaxial sides of the substrate, we can approximately determine the absorption coefficient of the epitaxial layer with the following equation.

$$\alpha_e = -\frac{1}{d_e} \ln \left(\frac{I_A}{I_B} \right)$$

Next, the absorption coefficient is measured for a wide range of temperatures. As shown in Figure 3.7, the absorption coefficient of the 10-ML InAs / 10-ML GaSb T2-SL increases with rising temperature. This is attributed to narrowing of the superlattice bandgap as temperature rises, which leads to an increase in the joint density of states between the conduction and valence bands of the superlattice.

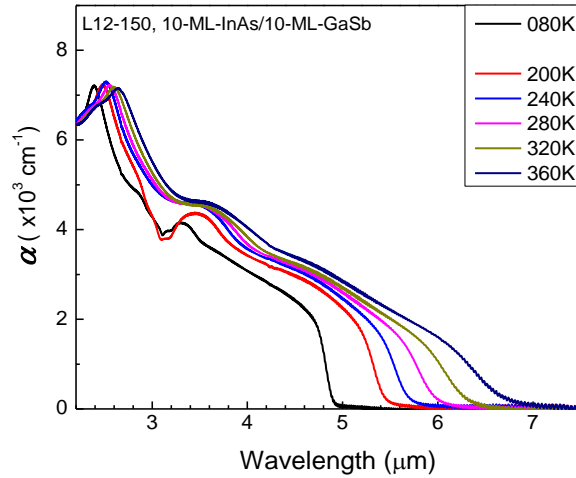


Figure 3.7: Approximate absorption coefficient for a 10-ML InAs / 10 ML GaSb T2-SL

It is important to note that this is the absorption coefficient for normal incidence. The optical absorption in InAs/GaSb superlattice is related to the overlap of electron and hole wavefunctions. Thin layers of superlattice have large overlap wavefunctions and therefore a large absorption coefficient. The overlap between the wavefunction appears near the hetero-interfaces and therefore the optical absorption is restricted to the vicinity of interfaces [67]. However, the absorption coefficient measurement does not take into account the anisotropic nature of a quantum well. Accurate ellipsometry measurements are possible, but expensive liquid nitrogen cooling equipment is required. As a result, designing a metamaterial cavity that is critically tuned to free space for optimum absorption of incoming radiation will be

difficult to achieve with a single metamaterial photodetector design. As a result, the metamaterial geometry must be tailored in order to experimentally determine an optimum response. In section 3.3.2, we determine an approximate geometry and its parameter space.

3.3.2 Metamaterial Photodetector Design Scheme

Next, we perform a rigorous electromagnetic simulation to understand the relationship between the metamaterial photodetectors geometry and the absorption coefficient required to achieve impedance matching to free space. As shown in Figure 3.8, our infrared quantum cascade photodetector is composed of a highly doped top contact, a graded hole barrier, an active superlattice absorber region, a graded electron barrier, and a highly doped bottom contact.

QCD Design

Layer name	Composition	Width (nm)	Doping (cm^{-3})	Repeat
Top Contact	GaSb (p doped)	50	$2\text{e}18$	1
Graded Hole Barrier	AlSb/InAs	43.5	None	1
Absorber	InAs (p doped)	3.5	$8\text{e}15$	40
Absorber	GaSb (p doped)	2.6	$8\text{e}15$	40
Absorber	InSb (p doped)	0.2	$8\text{e}15$	40
Graded Electron Barrier	AlSb/GaSb	32.6	None	1
Bottom Contact	InAs (n doped)	15	$2\text{e}18$	1

Figure 3.8: Growth profile of our simulated interband quantum cascade photodetector

For the simulation of a quantum cascade photodetector, we model its various semiconductor layers as a dielectric with loss. Although vigorous simulations that couple the electromagnetic behavior of the cavity and the quantum properties of the heterostructure are possible, an approximate simulation is adequate enough to locate a parameter space for the detectors experimental optimization. A square loop design, illustrated in Figure 3.9, was chosen because it can be designed to absorb all incoming radiation and serve as a continuous

electrical contact plane on the backside of a photodetector. In addition, this geometry was the safest choice for a conceptual demonstration although other geometries are possible because we wanted to ensure a proper electrical contact to the photodetector during the fabrication process.

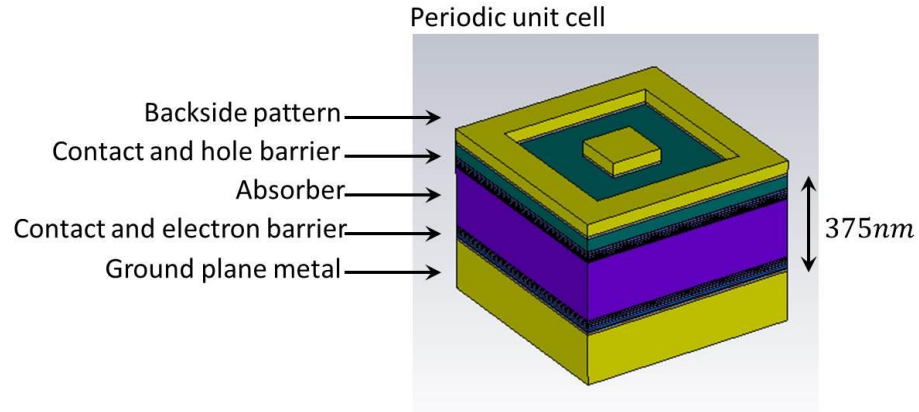


Figure 3.9: Illustration of the simulated QCD structure and its various layers, which include a backside pattern, a contact and hole barrier, an absorber, a contact and electron barrier, and ground plane metal

Next, we systematically vary the loss tangent to the active region of our metamaterial photodetector in an electromagnetic simulator and plot the absorption peak. The structure presented in Figure 3.9 was simulated using the commercial software CST Microwave Studio 2012. A time domain simulation was utilized and a Drude model was used to optically simulate gold with a plasma frequency $\omega_p = 2\pi \times 2175 \text{ THz}$ and collision frequency $\omega_c = 2\pi \times 18 \text{ THz}$. The permittivity of the dielectric absorber layer is 14 with a loss tangent of 0.07 for all wavelengths. The many other various layers utilize bulk semiconductor optical permittivity constants. A loss tangent is used to model its dielectric loss because it is wavelength independent. The absorption response of our metamaterial photodetector, plotted

in Figure 3.10, is initially under coupled, then achieves critical coupling to some finite loss tangent value, and then becomes over coupled.

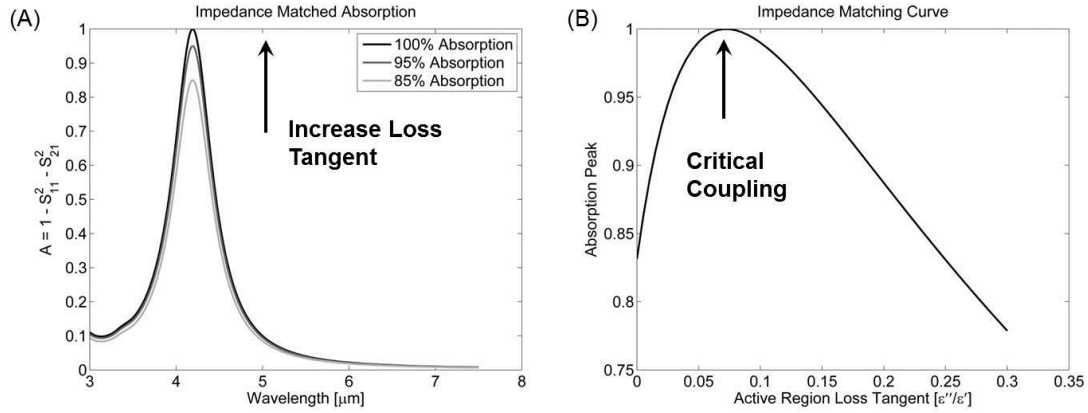


Figure 3.10: (A) Simulated spectral response of a metamaterial photodetector and its (B) impedance matching curve

When the loss tangent of the dielectric layer reaches a critical value, perfect absorption occurs. Based on an extensive simulation analysis, it appears that the amount of loss in the dielectric layer has a linear effect on the absorption peak (i.e. the resonant wavelength does not shift). Next, we perform the same rigorous electromagnetic simulation with different geometries. The design was varied from $a = 400\text{nm}$ to $a = 200\text{nm}$ with 100nm steps and an optimum loss tangent was found for each design. As illustrated in Figure 3.11, optimum loss tangent values are highly dependent on the geometry of our metamaterial. By varying the length of the square inside the metallic grid, we can tune the loss tangent required to achieve critical coupling to free space.

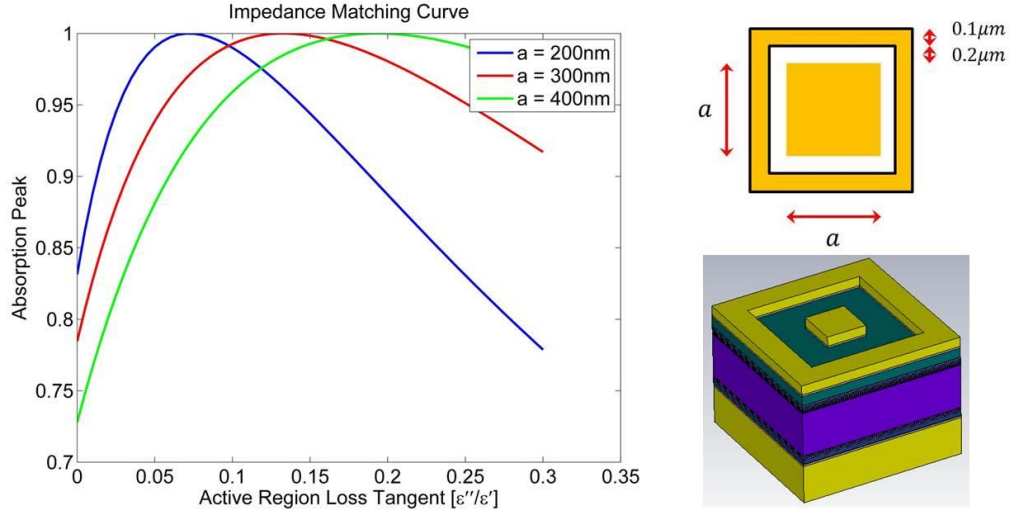


Figure 3.11: Simulated absorption coefficient for impedance matching the cavity to free space and simulated absolute absorption spectrum

Next, we convert each optimum loss tangent into a familiar, wavelength dependent absorption coefficient value using the mathematical relationships shown in Figure 3.12.

<p>Complex Permittivity</p> $\epsilon = \epsilon_1 + i\epsilon_2 = (n + i\kappa)^2$ $\epsilon_1 = n^2 - \kappa^2 \quad \epsilon_2 = 2n\kappa$	<p>→</p>	<p>Refractive Index</p> $n = \sqrt{\frac{\sqrt{\epsilon_1^2 + \epsilon_2^2} + \epsilon_1}{2}}$ $\kappa = \sqrt{\frac{\sqrt{\epsilon_1^2 + \epsilon_2^2} - \epsilon_1}{2}} = \sqrt{\frac{\epsilon_1 \sqrt{1 + (\epsilon_2/\epsilon_1)^2} - \epsilon_1}{2}}$ $= \sqrt{\frac{\epsilon_1 \sqrt{1 + (\tan \delta)^2} - \epsilon_1}{2}}$	<p>→</p>	<p>Absorption Coefficient</p> $\alpha = \frac{4\pi}{\lambda} \kappa$
---	----------	--	----------	--

Figure 3.12: Mathematical relationships between complex permittivity, refractive index, and absorption coefficient

Once converted to this familiar value, we plot it against our experimentally measured absorption coefficient. In this way, we are able to design a metamaterial cavity that is compatible with the absorption coefficient of an infrared photodetector. Even if our

measured absorption coefficient is not perfect, we now have a good understanding of how to tune the metamaterials geometry for impedance matching to free space, as illustrated in Figure 3.13.

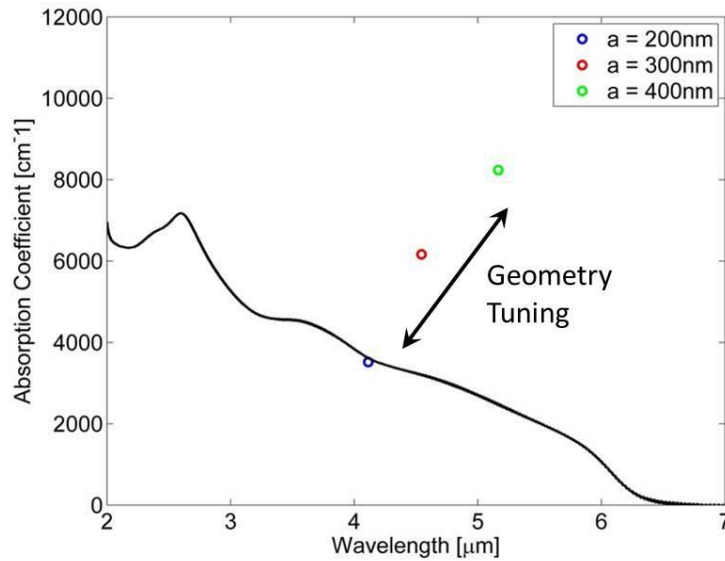


Figure 3.13: Illustration of how a metamaterial photodetectors geometry can be tuned to the absorption coefficient of the cavity (assuming the absorption coefficient of the T2-SL absorber is the dominant effect)

Next, we simulate the absorption response for each design with our measured absorption coefficient (approximately 3500cm^{-1}). As illustrated in Figure 3.14, the absorption peak is under coupled for geometries that have an inner square dimension larger than 200nm and should provide some insight into what to expect for an experimentally optimized photodetector.

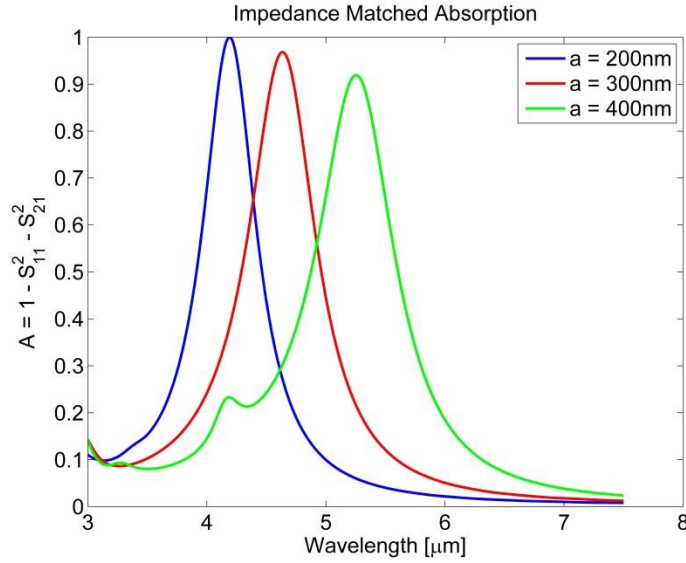


Figure 3.14: Simulated absolute absorption response of each geometry with an absorption coefficient of 3500cm^{-1}

3.3.3 Power Loss Density Profile

Once a metamaterial geometry is determined for impedance matching to free space, we perform an electromagnetic simulation at the resonance frequency for the optimized geometry ($a = 200\text{nm}$) to determine a power loss density profile to help understand useful absorption in the active region of our photodetector versus non-useful absorption in the doped contacts and dispersive metals. The dissipative power per unit volume is integrated for each layer in the metamaterial photodetector structure. Based on this simulation, we can calculate the amount of radiation lost in the active region of our photodetector and compare it to radiation lost in other layers. As computed in Figure 3.15, a significant amount of radiation is lost to materials other than the active region of our detector. We define materials other than the active region of our photodetector as “background loss” materials.

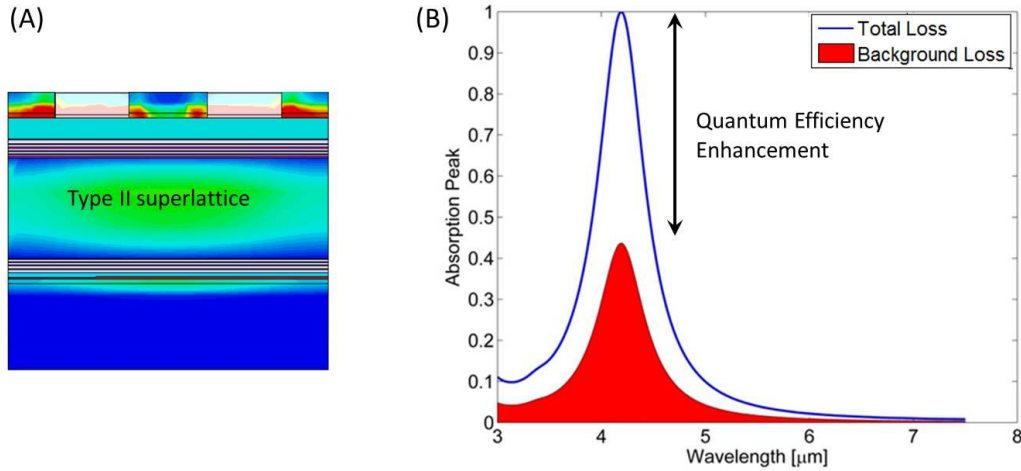


Figure 3.15: (A) Simulated power loss density profile of an interband cascade photodetector at the absorption peak and (B) spectral response with an active region absorption coefficient of 3500cm^{-1} and dispersive metals

Despite a significant amount of radiation lost to materials other than our Type II superlattice, there remains potential for significant quantum efficiency enhancement. In Chapter 6, we experimentally demonstrate this design scheme as well as measure the amount of radiation lost to background materials.

3.3.4 Angle Dependence

In this section, we determine the angle dependence of our metamaterial photodetector for our optimized geometry. This computer simulation can be used to predict abnormal effects during the characterization of our device. As illustrated in Figure 3.16, if the incident angle is greater than 20 degrees off normal, the absorption response of our metamaterial photodetector for TM polarization is disturbed and splits into two separate peaks. For TE polarization, the absorption strength of our metamaterial photodetector decreases.

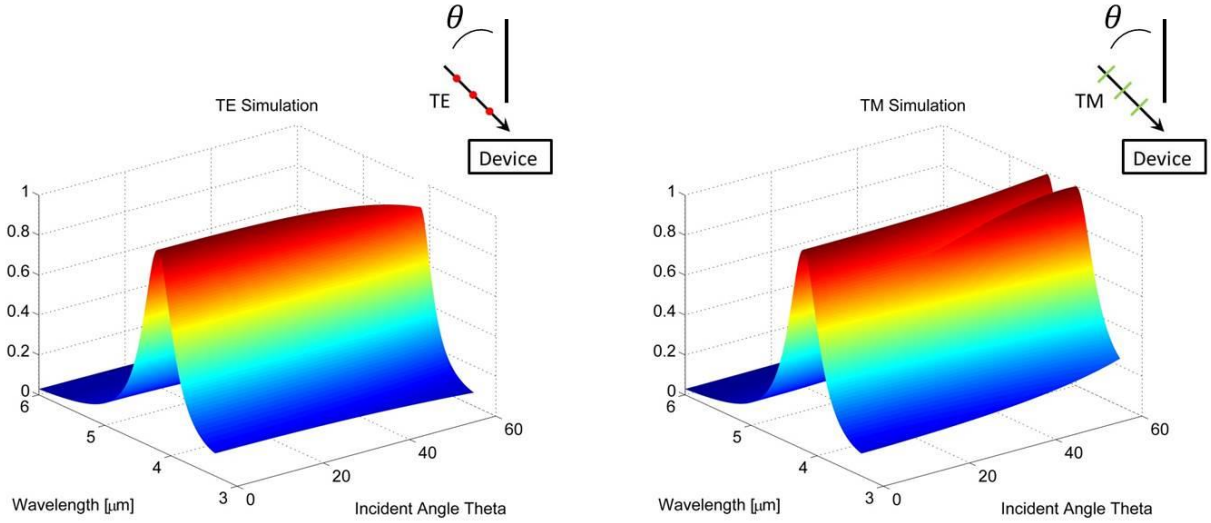


Figure 3.16: (A) Simulated TE response and (B) TM response as a function of incident angle for a metamaterial photodetector with $a = 200\text{nm}$

3.4 Summary

In this chapter, we introduced metamaterials as a new electromagnetic engineering design tool that enables a fundamentally new approach to control the flow of light. The metamaterial absorber, in particular, can be designed to absorb all incoming radiation. As a result, we thoroughly investigated metamaterial absorbers hybridized with an infrared photodetector for enhanced quantum efficiency. Based on our simulations, it was found that the absorption coefficient required to achieve impedance matching to free space is dependent on the metamaterial absorbers geometry. With this knowledge, we introduced a design scheme that can be applied to a photodetector to achieve critical coupling. However, 100% absorption doesn't necessarily mean 100% quantum efficiency. With an optimal geometry (the case for $a = 200\text{nm}$) we also computed a power loss density profile and determined that a significant amount of radiation is lost to the metal and doped contact layers. In the remaining part of this chapter, we also simulated the effects of off angle incident TM and TE radiation

on our metamaterial photodetector. It can be seen that the absorption peak of our structure remains stable until about 20 degrees.

Chapter 4 : Detector Fabrication

A new generation of infrared imaging systems that are capable of performing basic image-processing and image-recognition operations at the pixel-level are needed for chemical identification, noninvasive medical imaging, environmental monitoring, and night vision applications. Our ideal imaging system is based on the idea of a bio-inspired infrared retina, where basic image processing is directly performed on each pixel [68]. Performing pixel-level processing at the sensor and within the read-out integrated circuit (ROIC) would enable extremely high-performance processing inside the *smart imager* hardware, thereby enabling the sensor to output “compressed and important information” directly. However, the fabrication of a smart, 4th generation imager on an industrial and metamaterial design level is not practical with conventional FPA fabrication methods. To gain some insight into the technical challenges with conventional FPA technology and the development of a smart imaging system, in section 4.1, we demonstrate the fabrication process of a conventional FPA. In section 4.2, we attempt to address some conventional FPA design issues by fabricating a prototype test chip that also enables the characterization of a metamaterial photodetector and the initial development of a new FPA architecture. However, the fabrication process for this new FPA architecture is not optimized. In section 4.3, we discuss a highly advanced fabrication process that addresses all FPA design issues for the fabrication of next generation FPAs on the wafer level [69].

4.1 Conventional IR FPA Fabrication Process

A typical FPA is primarily composed of an array of pixels with a bottom electrical contact, a photodetector, and a top electrical contact. The bottom contact is formed on the bottom side of each pixel in the array. The top contact is defined at the base of the pixel array along its

boundary. The top contact makes electrical contact to the pixel array through a common, highly doped semiconductor ground plane. A completed FPA is flip-chip bonded to a read-out integrated circuit (ROIC) with conductive indium bumps and underfill epoxy. An illustration of a conventional FPA architecture is shown in Figure 4.1. This structure is illuminated from the substrate side of the pixel array.

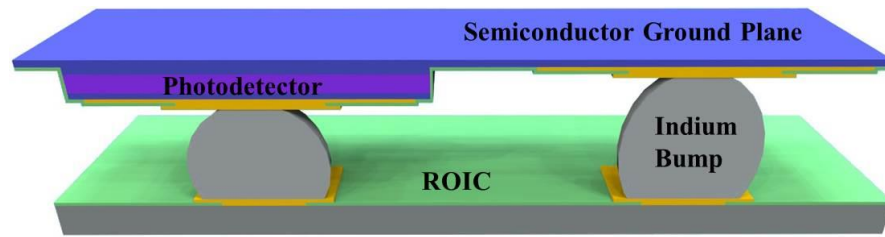


Figure 4.1: Conventional infrared focal plane array architecture

The following section is a fabrication procedure to define a conventional infrared FPA. The process begins by growing the crystal structure on epitaxial ready substrates in a solid source molecular beam epitaxy (MBE) system. In general, the growth procedure begins by desorbing native oxide from the substrate surface at an elevated temperature in a high vacuum chamber to expose the underlying crystal structure. Next, a lattice matched semiconductor smoothing layer is deposited to help reduce surface defects. After that, an etch stop layer (ESL) is deposited for selective substrate removal after flip-chip bonding the pixel array to a read-out integrated circuit (ROIC). The ESL layer is designed to have an etch rate that is significantly smaller than the etch rate of the host substrate in a wet or dry etching environment. Then a thick, highly doped semiconductor ground plane is deposited. A typical semiconductor ground plane is around 500nm to 1 μ m thick to provide some etch

tolerance during the pixel mesa etch step. The remaining layers define the active region of the infrared photodetector and a highly doped semiconductor contact layer.

Once the heterostructure has been defined by the MBE system, the pixel array and its electrical contacts are defined in a semiconductor processing cleanroom. The substrate is coated with AZ4330 photoresist, soft baked for 90 seconds, and then exposed to ultraviolet radiation with a chrome patterned quartz mask to define the pixel mesa array for 2 seconds. For this particular case, a 1 μm thick photoresist is used to accurately define the pixels and to survive the dry etching process. For a 320 x 256 FPA, each pixel is 24 μm x 24 μm in size with a 30 μm pitch. Next, the sample is placed in an inductively coupled plasma (ICP) etcher to define the array of pixel mesas. The etch depth is generally targeted to be halfway inside the highly doped semiconductor ground plane layer. A typical pixel height is between 1-2 μm . The etch recipe uses the following system settings on a PlasmaTherm 790 ICP system.

- BCl₃ flow: 35 sccm
- Chamber pressure: 2.5 mTorr
- Temperature: 25 C
- ICP power: 500 W
- RIE power: 90 W

After ICP etching, the sample is pretreated for 30 seconds with a 1:10 HCl:H₂O acid dip to remove oxides or free ions that may have formed at the device/air interface. These surface defects can create trap centers in the middle of the semiconductor bandgap that can ultimately reduce the efficiency of the photodetector. Immediately after pretreating the sample, a 100nm layer of silicon dioxide is deposited on the sample to electrically passivate the side walls of the pixel mesas. The passivation step takes place in a chemical vapor deposition (CVD) machine with the following system settings.

- N₂ flow: 40 sccm
- N₂O flow: 160 sccm

- SiH₄ flow: 20 sccm
- Chamber Pressure: 760 mTorr
- Temperature: 190 C
- RF Power: 70 W

Once completed, AZ5214-IR photoresist is spin coated onto the sample. A second mask is used to define the top and bottom electrical contacts to the FPA by exposing the resist for 2 seconds, post baking for 60 seconds, and then flood exposing for 30 seconds. Once the photoresist is developed, the exposed layer of silicon dioxide is etched away to expose the highly doped semiconductor contact layer. This is performed in a reactive ion etcher (RIE) with the following recipe.

- Ar flow: 5%
- O₂ flow: 5%
- CF₄ flow: 90%
- RF Power: 150W

Next, if the material system is based on a GaAs alloy family, Ohmic contact metal consisting of Ge(280 Å)/Au(540 Å)/Ni(200 Å)/Au(3,000 Å) is deposited onto each pixel. After metal liftoff, a rapid thermal anneal (RTA) at 370 degrees Celsius for one minute is performed to provide a low contact resistance. If the material system is based on a GaSb alloy family, Ohmic contact metal consisting of Ti(100 Å)/Au(1000 Å) is deposited. A RTA is typically not required for GaSb based alloys due to their small bandgap. It is desirable to place an indium bump onto the contact metal for hybridization to a read-out integrated circuit (ROIC). Before this can occur, an under bump metal (UBM) consisting of Ti(500 Å)/Ni(1500 Å)/Au(500 Å) is capped over the contact metal and silicon dioxide window to prevent indium from diffusing into the contact metal and mesa, which would result with a degraded Ohmic contact and high pixel dark current. The titanium layer acts as a metal adhesion layer, nickel serves as an indium diffusion barrier, and gold is used to wet and mount the indium bump.

The lithography step to achieve UBM is performed with AZ5214-IR resist. The fabrication steps to define a pixel array, beginning with a mesa etch, passivation layer, contact layer, and UBM, are shown in Figure 4.2.

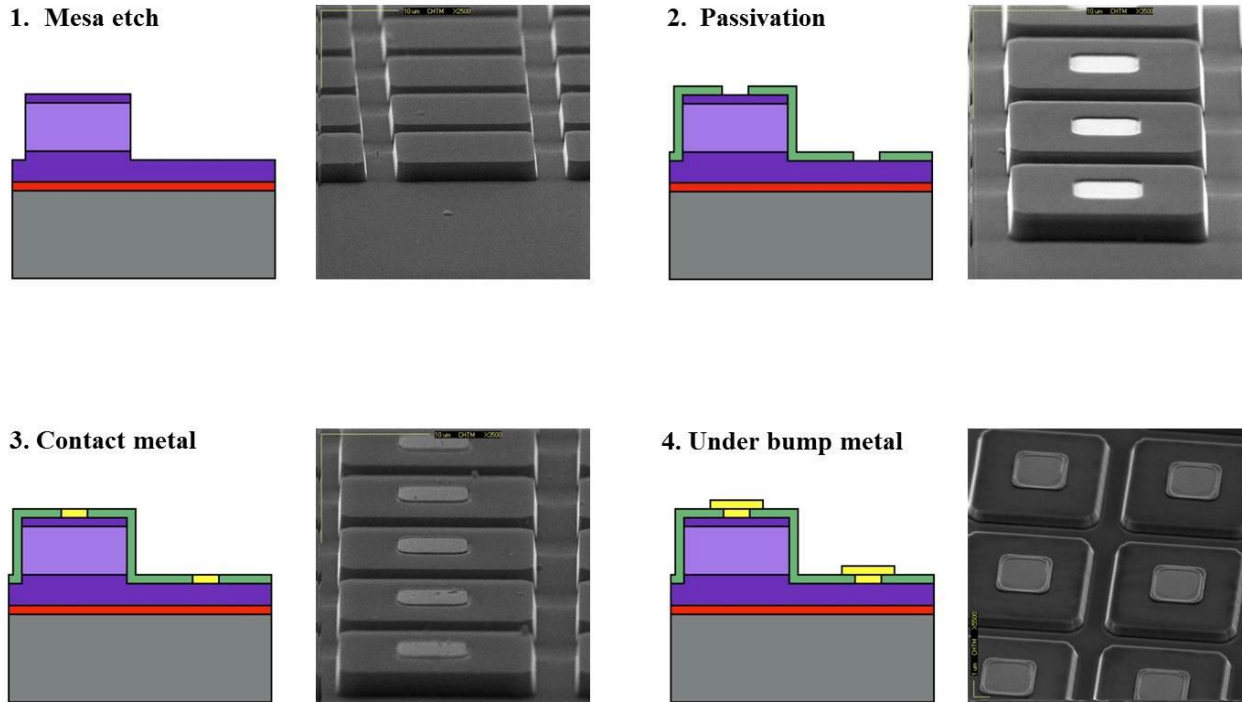


Figure 4.2: Fabrication steps to define a pixel array beginning with a mesa etch, passivation layer, contact layer, and under bump metal

The substrate is now coated with a $10\mu\text{m}$ thick layer of AZ4620 photoresist, baked for 12 minutes, and exposed with a mask for 30 seconds. Large holes in this photoresist are developed over the UBM metal. A $2\mu\text{m}$ thick layer of indium is deposited onto the UBM metal for the eventual formation of an indium bump. It is important to form a large indium bump to ensure electrical contact between the ROIC and all pixels in the array. In addition, a large indium bump can help reduce thermal stress that results from thermal mismatch between the ROIC and FPA. After depositing indium onto the substrate and performing a

metal liftoff step, the wafer is diced into individual dies with a dicing saw and cleaned. From this point forward, the remaining steps must be performed one die at a time. Next, a single die is coated with indium flux and heated to 180 C for several minutes. Reflow occurs when indium surface tension forces dominate the attractive forces of the silicon dioxide passivation layer. A typical bump height for an FPA is around $8\mu\text{m}$. After indium reflow, the indium flux is removed with acetone. Example images of an indium pad before reflow and after reflow are shown in Figure 4.3.

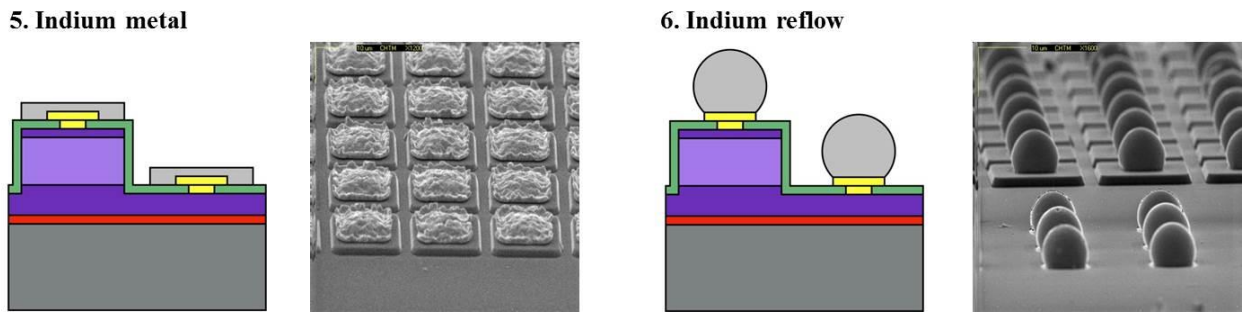


Figure 4.3: Fabrication steps to define an indium bump for flip-chip bonding

Once the pixel array has been defined, indium pads are deposited over the electrical contacts on the ROIC. A typical electrical contact on a ROIC is made of aluminum, which doesn't stick very well to an indium bump. As a result, these indium pads are defined to help ensure electrical contact between the ROIC and FPA. No indium reflow is required for the indium pads on the ROIC. Next, the ROIC and FPA are mounted to the upper and lower arms of a Karl Suss FC-150 flip-chip bonder. Flip-chip bonding is a process where a chip is flipped, aligned and bonded to another chip to form an electrical connection. Once the chips have been properly aligned through a split-screen microscope, the microscope is removed and the ROIC and FPA are brought together under heat and pressure, as shown in Figure 4.4.

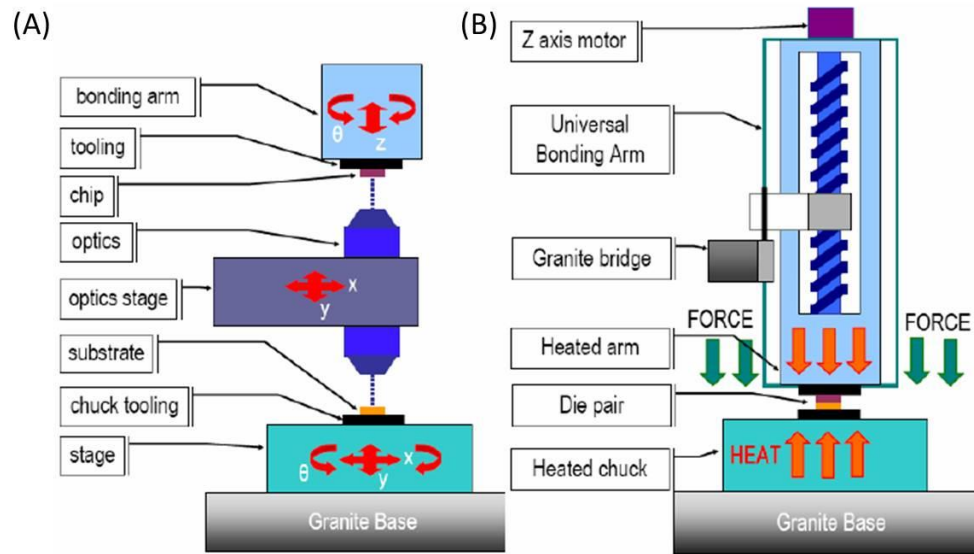


Figure 4.4: (A) FPA and ROIC alignment with a split-screen microscope (B) FPA and ROIC bonding

A flip-chip bonding recipe for a 320 x 256 FPA and ROIC is not a straightforward process. The bonding recipe requires careful calibration of the bonding pressure and temperature. If the bonding temperature is too high, indium from neighboring pixels will melt and fuse together, which will result with a patch network of shorted pixels. If the bonding temperature is too low, the indium bump will not melt enough to form a good electrical contact. The bonding pressure is also carefully calibrated so that indium bump height is as tall as possible to reduce thermal stress. The development of an extreme flip-chip bonding recipe for ultra large indium bumps is provided in section 4.2 in greater detail. The flip-chip bonding recipe developed for a 320 x 256 FPA is shown in Figure 4.5.

7. Flip-chip bonding

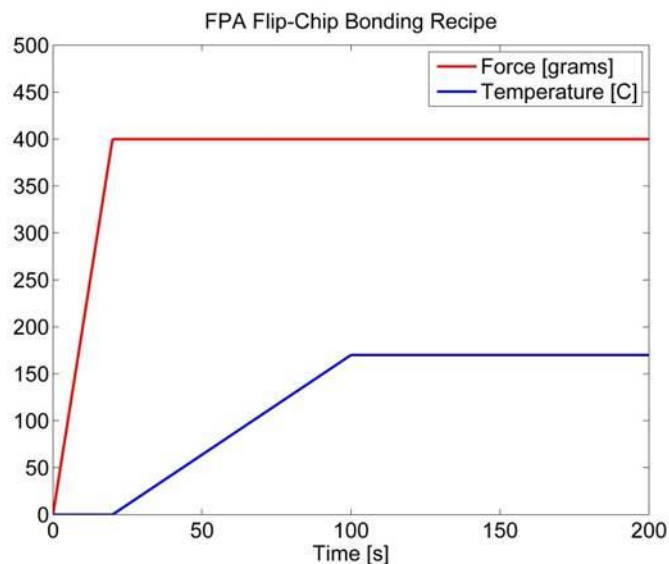
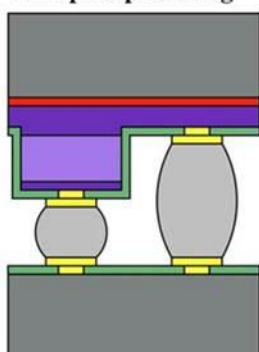
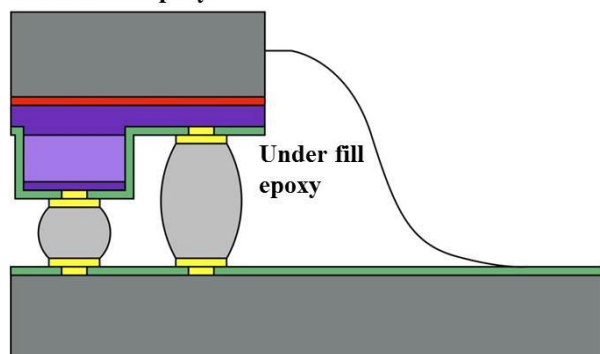


Figure 4.5: FPA flip-chip bonding recipe with 400g of applied force and 170C of applied heat

Next, the FPA is permanently bonded to the ROIC by placing a nonconductive underfill epoxy between the two chips with the aid of the capillary force to feed epoxy. This underfill epoxy is designed to be chemically inert and to reduce thermal stress between the ROIC and FPA at liquid nitrogen temperatures.

8. Under fill epoxy



Hybridized FPA

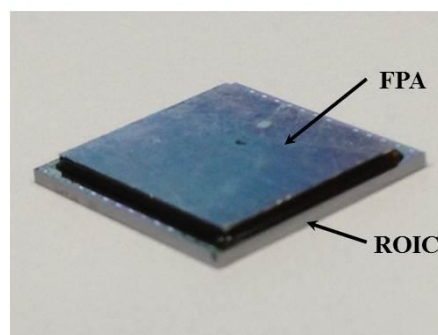


Figure 4.6: Placement of underfill epoxy between the ROIC and FPA

After permanently bonding the FPA to the ROIC, the die is mounted to a polishing jig for chemical mechanical polishing (CMP) (see Figure 4.7). A CMP is a two-step process that combines both chemical etching and abrasive polishing to reduce the thickness of a substrate. The mechanical polishing step utilizes aluminum oxide slurry to physically reduce the substrate on a rotating glass plate. After mechanical polishing, the glass polishing plate is replaced with a rubber lined plate and a solution of sodium hypochlorite and aluminum oxide (particle size $\sim 300\text{nm}$) is used to polish the sample to a mirror-like finish. The substrate is typically reduced to $20\mu\text{m}$ because this thickness has a negligible effect on attenuating incoming radiation to the pixel array. However, if the remaining substrate is not removed, there is some increased risk to the FPA cracking at low operating temperatures. To help reduce this risk, the remaining substrate can be selectively removed using selective etching techniques [70].

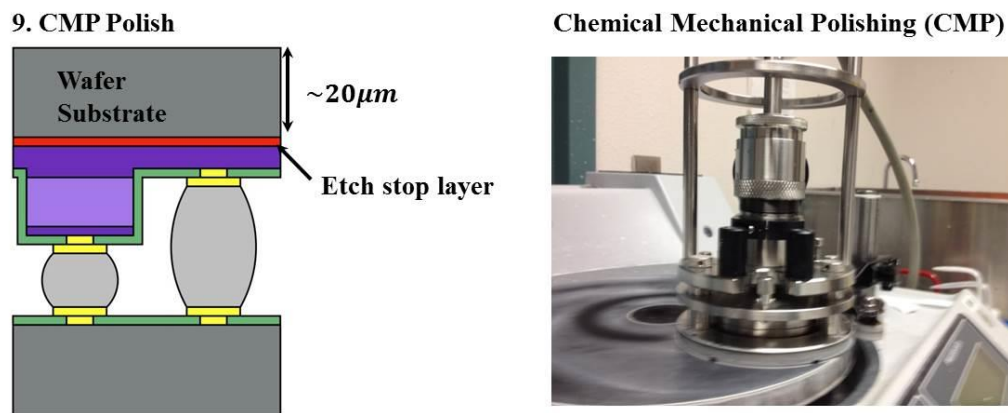


Figure 4.7: Chemical mechanical polishing of an FPA down to $20\mu\text{m}$

To achieve this goal, a selective substrate removal recipe must be developed to etch the remaining substrate, yet stop at the substrate / heterostructure interface. In this section, we develop a highly selective dry etching recipe with a RIE system. In order to develop a

selective substrate removal recipe, we first have to understand the operation of our Trion Minilock RIE system in selective and non-selective etching conditions. This RIE system consists of two parallel plates in a cylindrical chamber with the sample sitting on the lower plate. Gases with desired chemical properties are introduced to the chamber where a strong electromagnetic field is applied to ionize the gases to form plasma. As the electromagnetic field oscillates, ions are electrically accelerated up and down between the two plates with some ions striking the sample. These ions chemically react with the sample to form volatile compounds with a low boiling point temperature. As a result, these compounds will desorb from the substrate surface where they make their way out of the RIE system through a vacuum pump. However, it is possible to introduce gas chemistries that form compounds with low volatility and a high boiling point temperature so that no etching occurs with certain materials. A RIE recipe that can produce volatile compounds, causing a material to etch, and non-volatile compounds, causing other materials to become resistant to etching, is the premise behind RIE selective etching.

Prior substrate removal recipes have been developed with SF_6 and BCl_3 gases in a RIE system to selectively etch GaAs without significantly etching AlGaAs [70]. During epitaxial growth, an AlGaAs layer is grown to provide an etch barrier between the GaAs substrate and heterostructure. When an electromagnetic field is applied to the RIE chamber, fluorine and chlorine ions are formed in the plasma. Chlorine ions react with the GaAs substrate resulting with volatile compounds that desorb from the surface. Etching continues until AlGaAs is exposed. At this time, fluorine ions react with the exposed aluminum to form aluminum trifluoride, which is a non-volatile compound with a high boiling point temperature that essentially stops the etching process. The recipe presented in this section

slightly modifies the GaAs/AlGaAs etch recipe to etch GaSb/AlAsSb with the same effect. An illustration of how the selective GaSb/AlAsSb etching process occurs on a test sample with a $2\mu\text{m}$ GaSb layer and thin AlAsSb ESL is provided in Figure 4.8.

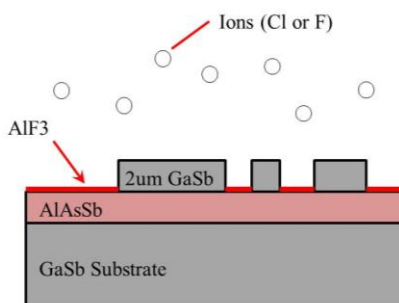


Figure 4.8: Selective substrate removal of GaSb with an AlAsSb etch stop layer

The goal is to maximize the etch rate of the GaSb layer while minimizing the etch rate of the AlAsSb layer. The RF power and chamber pressure was set to 100W and 100mTorr, which are typical RIE settings. A high RF power causes ions in the chamber to be more energetic while a high chamber pressure helps with the dissociation of gas molecules into ions. A Trion Minilock RIE system with BCl_3 and SF_6 gas chemistries are used. To determine an optimized recipe, the ratio of BCl_3 to SF_6 was varied to determine a gas composition with maximum selectivity. The gas flow rate was kept at 20 sccm for all measurements (20 sccm = X sccm BCl_3 + Y sccm SF_6). The etch rate of GaSb with different gas ratios was determined by etching 1cm x 1cm GaSb substrate samples patterned with AZ4330 photoresist for 10 minutes. After removing the photoresist with acetone, the etch depth of each sample was measured with a stylus profilometer and an etch rate was calculated for each etch recipe. Next, a test sample was grown with a 100nm AlAsSb layer and a $2\mu\text{m}$ GaSb capping layer on a GaSb substrate to measure the etch rate of AlAsSb with varying

SF₆ to BCl₃ gas ratios. A capping layer is required to prevent oxidation of AlAsSb in the atmosphere and to simulate substrate removal. The development of this recipe is performed on the top side of the substrate to reduce development time. This sample is diced into 1cm x 1cm squares and patterned with AZ4330 photoresist. The time required to etch the 2 μ m GaSb capping layer is estimated for each gas ratio and added to the time AlAsSb is exposed. The etch depth into the AlAsSb layer was measured and divided by the AlAsSb exposure time to determine an etch rate. Data for the GaSb and AlAsSb etch rate with varying SF₆ to BCl₃ ratios is shown in Figure 4.9.

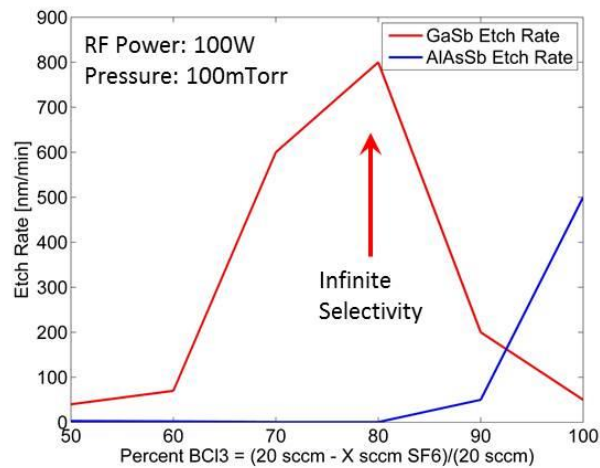


Figure 4.9: GaSb and AlAsSb etch rates with varying SF₆ to BCl₃ gas ratios for 100W RF power and 100mTorr chamber pressure

It can be seen from Figure 4.9 that the etch rate of GaSb is low for 100 percent BCl₃, maximizes at 80 percent BCl₃, and then gradually declines for lower concentrations. This can be explained by observing that SF₆ is a large molecule compared to BCl₃ and that an increase in SF₆ helps with the disassociation of gas molecules in the chamber into ions. An increase in chlorine ions will increase the etch rate of GaSb and an increase in fluorine ions

will decrease the etch rate of AlAsSb. It is observed that etch selectivity for this gas chemistry is infinite when BCl₃ is 80 percent and SF₆ is 20 percent because the etch depth is virtually zero for this ratio. We provide an image of the AlAsSb etch stop layer after removal of the GaSb capping layer in Figure 4.10.

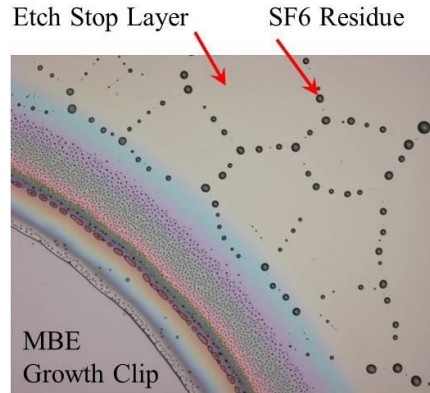


Figure 4.10: Selective substrate removal of GaSb on AlAsSb

At this point, the developed RIE recipe is applied to the remaining 20 μ m layer of GaSb substrate on the FPA with ROIC contacts protected with etch resistant wax. As seen in Figure 4.11, we are able to monitor the dry etching process of the FPA with a camera mounted to the RIE system. During this process, the etch stop layer is first exposed on the corners of the FPA with some remaining substrate at its center. Selective etching continues until the entire GaSb substrate is removed.

FPA Substrate Removal

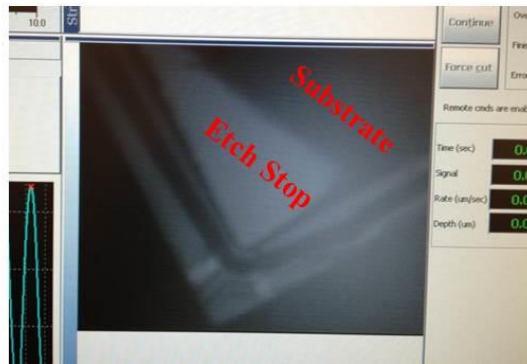


Figure 4.11: Corner image of an FPA during substrate removal with the AlAsSb etch stop partially exposed

After substrate removal, the FPA is treated in a dilute solution of hydrofluoric acid to clean the backside of the FPA. Once completed, the FPA is mounted to a chip carrier, wire bonded and used to produce an infrared image in a camera system. To reduce Fabry-Perot interference effects, an antireflection coating is coated onto the backside of this FPA.

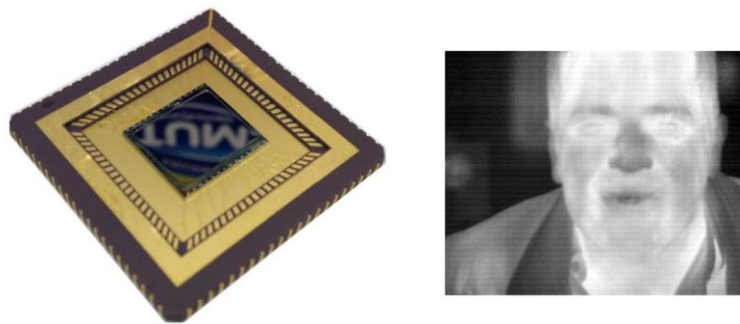


Figure 4.12: Completed fabrication of a conventional infrared focal plane array

4.1.1 Conventional IR FPA Fabrication Issues

Many of the fabrication steps are a single die process, which significantly increases the cost to produce a conventional FPA. Also, after flip-chip bonding the pixel array to the ROIC, the ROIC is now at risk to electrostatic and/or physical damage during the remaining

fabrication steps. In addition, a conventional FPA requires a thick semiconductor ground plane to serve as a common contact to the pixel array, which is at risk to cracking at liquid nitrogen temperatures, as demonstrated in Figure 4.13.

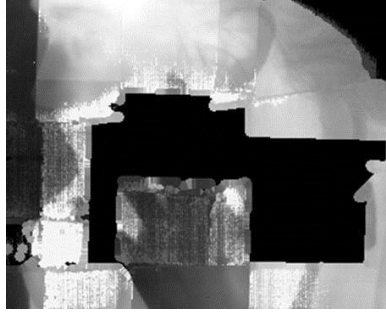


Figure 4.13: FPA with a cracked semiconductor ground plane due to thermal stress

If a metamaterial photodetector design is applied to a conventional FPA design, a significant amount of radiation would be lost to the semiconductor ground plane. Also, after substrate removal, there is a thick layer of underfill epoxy that exists at the boundary of an FPA as shown in Figure 4.14. This underfill epoxy is designed to be chemically inert to ensure a long FPA lifetime with low thermal stress. However, removal of this excess underfill epoxy so that additional fabrication steps can be applied to the backside of an FPA has proved challenging. Nevertheless, we demonstrate a metamaterial photodetector with a QWIP where many of these fabrication challenges can't be avoided in Chapter 5.

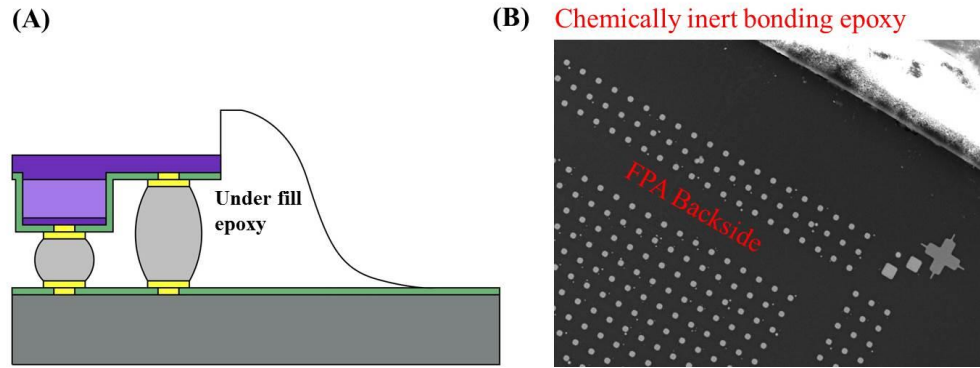


Figure 4.14: (A) Side profile and (B) SEM image of the backside of a conventional IR FPA after substrate removal with excess epoxy along its boundary.

A new FPA architecture is required to overcome these fabrication challenges. In section 4.2, we attempt to address some of these design issues by fabricating a prototype test chip, with a new FPA architecture, that replaces the thick semiconductor ground plane with a highly flexible backside metal that enables the highly doped semiconductor ground plane to be significantly thinner and independent of each pixel. This test chip also incorporates extremely large indium bumps to help separate the pixel array from the control chip so that a dicing saw can be used to remove the excess epoxy. After removal of this excess epoxy, additional fabrication steps can be applied to define a metamaterial photodetector. In addition to demonstrating a new FPA architecture, this prototype test chip is used to demonstrate a bio-inspired multicolor metamaterial pixel array with high quantum efficiency. For an experimental demonstration of this new FPA architecture, see Chapter 6 and 7.

4.2 Prototype Chip Fabrication Process

This new fabrication process attempts to address some design issues associated with a conventional FPA. We address the cracking issue with the highly doped semiconductor contact layer by replacing it with a highly flexible metal layer. This metal layer not only

improves the thermal lifetime of the FPA but also provides greater optical isolation between neighboring pixels resulting with lower optical crosstalk. In addition, the thickness of the highly doped semiconductor contact layer can be any desired thickness and independent from neighboring pixels. If a metamaterial pattern is placed onto the illumination side of the pixel array, reducing the thickness of the semiconductor contact layer can reduce the amount of radiation lost to this layer, which can result with higher detector quantum efficiency. The work presented in this section is a prototype test chip that demonstrates a new FPA architecture with enhanced quantum efficiency at multiple colors. The fabrication process is not perfect and continues to implement some design steps used for conventional FPA fabrication. However, design lessons learned from this prototype chip are used to design an advanced FPA fabrication process that achieves all design goals on the wafer level in a later section.

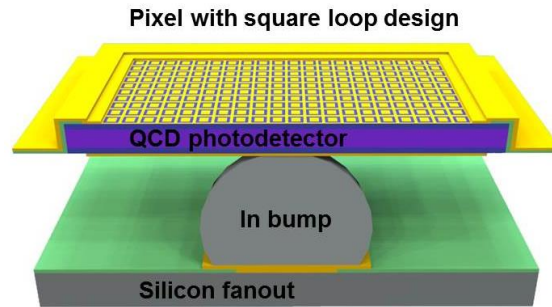


Figure 4.15: Next generation FPA architecture

The fabrication process begins by performing a dry etch to define the pixel mesas. The ESL layer is used to selectively etch the pixel from the front side for accurate pixel definition. For this prototype chip, the pixel size is $120\mu\text{m} \times 120\mu\text{m}$. Next, a $\text{Ti}(100\text{ \AA})/\text{Au}(2000\text{ \AA})$ contact metal is placed on each pixel. Because this layer also serves as an electromagnetic ground plane to the metamaterial photodetector, the titanium layer is kept as thin as possible

to reduce the amount of radiation lost in this highly absorbing layer in the infrared. Both titanium and gold make a good Ohmic contact metal to GaSb alloys. Next, a 100nm silicon dioxide passivation layer is placed over all the pixels. A window in the silicon dioxide layer is opened over the contact metal to allow electrical contact to the UBM metal.

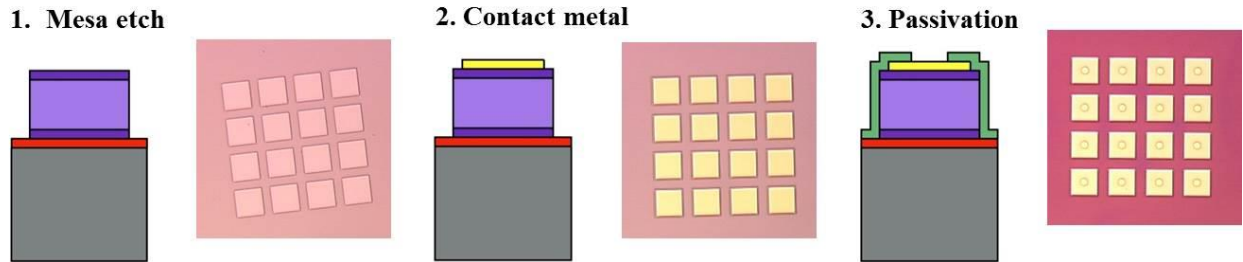


Figure 4.16: Fabrication of a pixel mesa with contact metal and a passivation layer

A Ti(500 Å)/Ni(1500 Å)/Au(500 Å) UBM metal is then placed over the pixels to serve as trace lines for electrical contact to a silicon control chip, as shown in Figure 4.17. The sample is then diced and cleaned for flip-chip bonding.

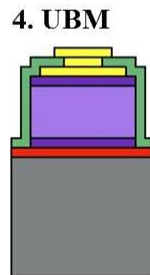


Figure 4.17: UBM on the pixel array

A control chip was fabricated in parallel to the fabrication of the pixel array. The fabrication of the control chip started with a silicon wafer with a $1\mu\text{m}$ thick layer of silicon dioxide. Metal control lines are defined on the silicon wafer with Ti(500 Å)/Au(3000 Å) metal, which

will be used to make electrical contact to the pixel array and wire bonding pads. A 100nm layer of silicon dioxide is deposited over the UBM trace lines. Next, a window in the silicon dioxide layer is opened over the wire bonding and indium bump pads. A UBM metal consisting of Ti(300 Å)/Ni(1,500 Å)/Au(500 Å) is then deposited to cap openings made in the silicon dioxide windows. A large $80\mu\text{m} \times 80\mu\text{m}$ indium pad is deposited $3\mu\text{m}$ thick over the UBM metal on the indium pads and reflowed to form large $40\mu\text{m}$ indium bumps. See Figure 4.18 for a scanning electron microscope (SEM) image of these large indium bumps.

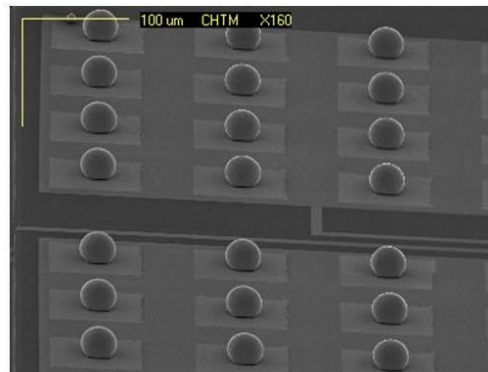
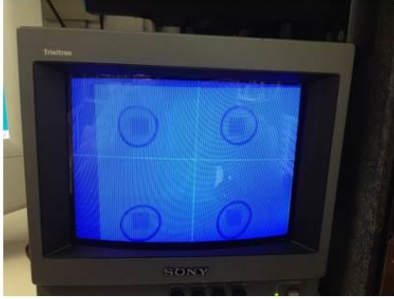


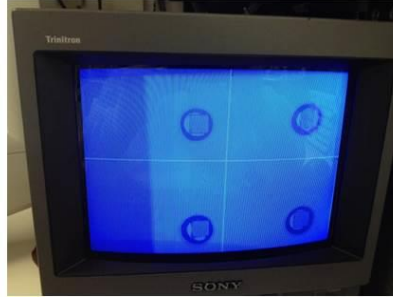
Figure 4.18: Silicon control chip with $40\mu\text{m}$ indium bumps

It is important to maintain a large separation distance between the control chip and the pixel array for excess epoxy removal with a dicing saw. To achieve this goal, a good flip-chip bonding recipe must be developed with quartz dummy samples to visually inspect the indium bump after flip-chip bonding for an optimum indium bump formation. This bonding recipe optimizes both temperature and applied pressure to simultaneously form an electrical contact with a tall indium bump. This optimization process is illustrated in Figure 4.19.

150 Celsius, **400 grams force**
Hold for 1 minute



150 Celsius, **50 grams force**
Hold for 1 minute



145 Celsius, **50 grams force**
Hold for 1 minute

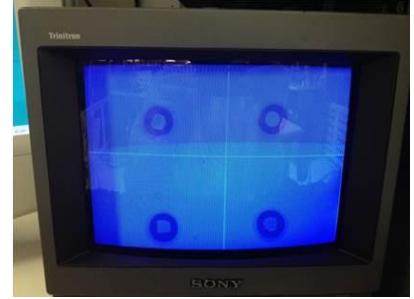


Figure 4.19: Flip-chip bonding optimization scheme for $40\mu\text{m}$ indium bumps

An applied temperature of 145C with 50 grams of pressure, held for 1 minute, provides a good electrical contact with a large chip separation distance. Next, the pixel array is flip-chip bonded to the control chip with this optimized recipe and underfill epoxy is applied to the chip and cured. Next, a dicing saw is carefully calibrated to the top of the silicon control chip, yet below the pixel array layer to remove excess epoxy along the boundary of the chip. The dicing saw is stepped until all excess epoxy is removed, as demonstrated in Figure 4.20.

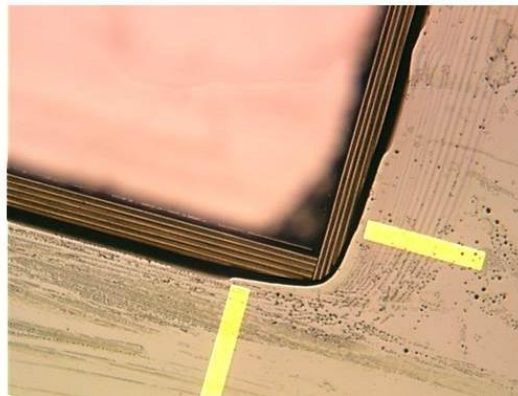


Figure 4.20: Excess epoxy removal with a dicing saw

Next, the GaSb substrate is removed through a combination of chemical mechanical polishing and selective RIE dry etching steps. Once the substrate is removed, a layer of $\text{Ti}(50 \text{ \AA})/\text{Au}(2000 \text{ \AA})$ is placed onto the backside of the pixel array with aperture openings

over the pixels. E-beam lithography alignment marks are also defined on the outside edges of the pixel array to align the e-beam writer for effective pixel patterning. After that, the backside of each pixel is patterned with a metamaterial pattern with the aid of e-beam photolithography. A thin Ti(50 Å)/Au(1000 Å) layer is then deposited to define the patterns and to reduce electromagnetic loss in the metal. The writing of this sample used ZEP520A electron beam resist developed in n-amyl acetate, exposed at 20nA with a step of 20nm on a JEOL JBX-9300FS e-beam lithography system.

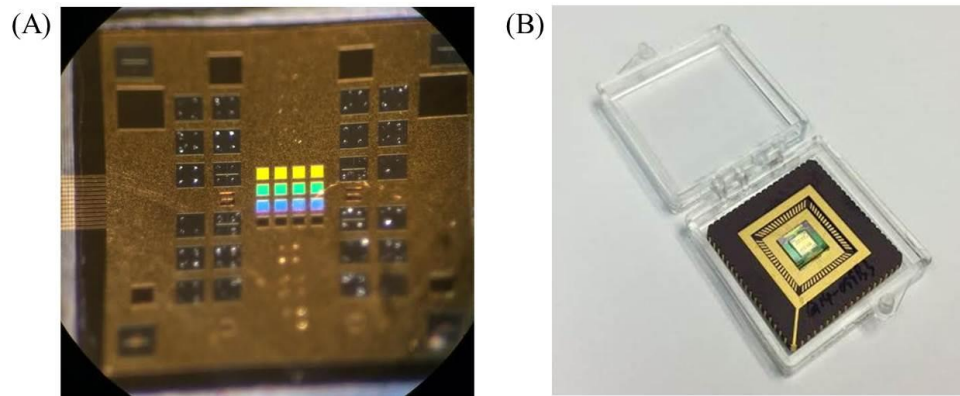


Figure 4.21: Completed prototype FPA / Test chip

4.2.1 Prototype Chip Fabrication Issues

Although this prototype test chip demonstrates a new FPA architecture with an advanced pixel design, the fabrication process is not perfect because it requires a few extraordinary procedures for its demonstration. First, the fabrication process requires an unusually large indium bump to help separate the pixel array from the control chip. These indium bumps are too large for a practical FPA because their small pitch is not compatible with their fabrication process. Also, a dicing saw must be used to physically remove excess epoxy from the boundary of the chip. This requires careful calibration of the saw, which often times makes the sample at risk to the proper operation of the machine. In addition, e-beam lithography is

required to produce a metamaterial pattern and many steps remain a single die process. In section 4.3, we discuss a highly advanced fabrication process that addresses all FPA design issues for smart, 4th generation imaging applications.

4.3 Next Generation FPA: The Smart Imager

A new generation of focal plane arrays (FPAs) is required for enhanced imaging capability with a low system cost. The development of a new generation of FPAs is primarily hindered upon their effective design and fabrication. With design lessons from the prototype test chip, a new FPA architecture is presented to allow accurate pattern definition, low cost substrate removal, and the option for additional fabrication steps on the wafer level. Through this proposed process, a lower fabrication time and cost should result with enhanced system functionality. This new FPA architecture redefines key components of a conventional FPA and makes use of three-dimensional wafer processing techniques to achieve certain design goals. Similar to a conventional FPA, the bottom contact is formed on the bottom side of each pixel in the array. However, the top contact is no longer defined by a highly doped semiconductor ground plane. The top contact is defined by a highly flexible metal layer directly on the backside of each pixel in the array with an optical aperture. This results with an FPA that has a longer thermal cycle lifetime, very thin semiconductor contact layers, and improved optical isolation between pixels. In addition, a metallic ground plane enables the design and fabrication of highly advanced FPAs with a metamaterial absorber design for bio-inspired smart imaging. For greater detail of these fabrication steps and some design considerations outside the scope of this thesis, please see the pending patent filed in 2013 [69].

The fabrication process for a smart imager begins by first defining a metamaterial pattern onto a wafer with a predefined semiconductor heterostructure that encompasses an infrared photodetector and a highly selective epitaxial lift-off layer. It is important to note that defining the metamaterial pattern first is a key advantage to this fabrication process because issues with existing patterns interfering with the lithography process have been eliminated. In addition, many advanced lithography systems (nanoimprint, stepper, interferometric, etc.) require blank, whole wafers for accurate pattern alignment and effective registration of small features. Next, a mesa etch is performed by utilizing the highly selective epitaxial lift-off layer to precisely define the etch depth for the pixel array. Once pixels are defined, an electrical passivation layer is coated onto the side walls of the pixel array. This passivation layer should be chemically inert to selective etching solutions during the epitaxial lift-off step. After placing an electrical passivation layer onto the pixel array, a common contact metal is placed to serve as a common ground plane to the entire pixel array. By placing a common contact metal, in place of a highly doped semiconductor contact plane, a higher thermal cycle lifetime should result because metals are more malleable than semiconductor crystals in low temperature environments, and therefore more tolerable to thermal cycles. These fabrication steps are illustrated in Figure 4.22 to provide contrast to the fabrication process of a conventional FPA. As one may note, the optical aperture to the pixel array is on the “wrong side” compared to a conventional FPA at this fabrication stage.

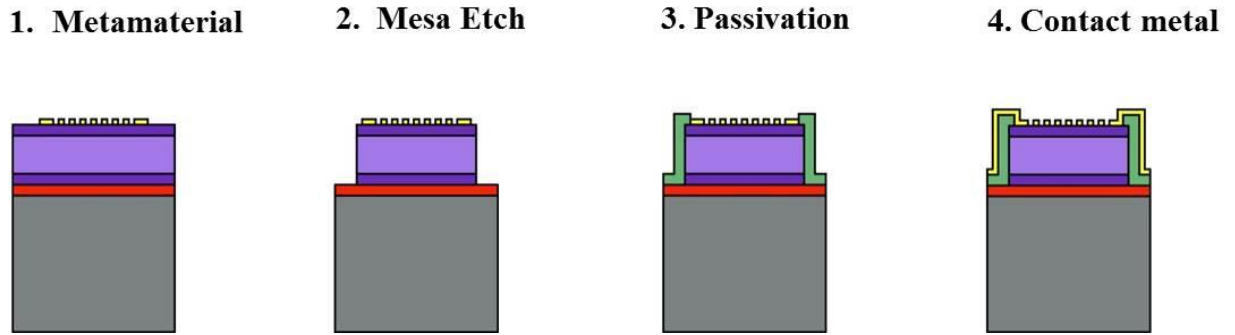


Figure 4.22: Fabrication steps to define a pixel array beginning with metamaterial patterning, mesa etch, passivation layer, and contact layer

As illustrated in Figure 4.23, the wafer containing the pixel array is temporarily bonded to a flexible handle wafer using a temporary bonding polymer. A flexible handle wafer is utilized to help peel away the pixel array from its supporting substrate when the epitaxial lift-off layer is exposed to a chemical solvent [71]. This fabrication step represents another key advantage to this method because substrate removal is performed on all dies simultaneously and it enables the added benefit to recycle the semiconductor substrate. In addition, the ROIC is no longer a part of the substrate removal process, which eliminates possible damage to the ROIC during this step. And finally, an epitaxial lift-off method is considerably easier to achieve compared to a CMP process where physical polishing of the substrate can lead to cracking and poor device yield.

5. Bond to handle

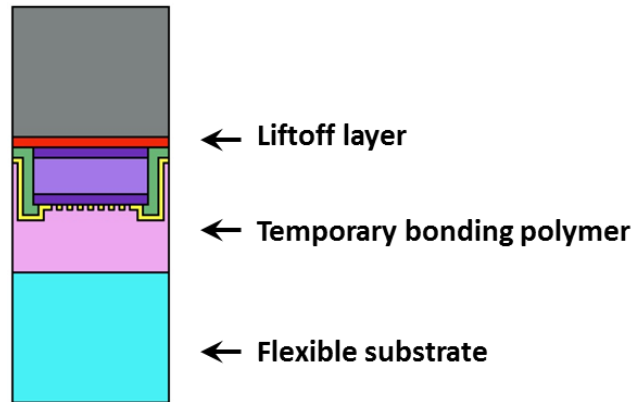


Figure 4.23: Illustration of the pixel array temporarily bonded to a flexible handle wafer

According to Cheng, aluminum containing epitaxial lift-off layers can result with post processing residues that require additional processing steps for substrate reuse [71]. However, if a phosphide containing semiconductor alloy is utilized as an epitaxial lift-off layer, the substrate can be reused immediately after epitaxial lift-off because the issue with substrate residue was eliminated. In addition, epitaxial lift-off can take place with hydrochloric acid, which is less harmful to the environment and cleanroom workers than hydrofluoric acid, which is typically used to selectively etch aluminum containing alloys [71].

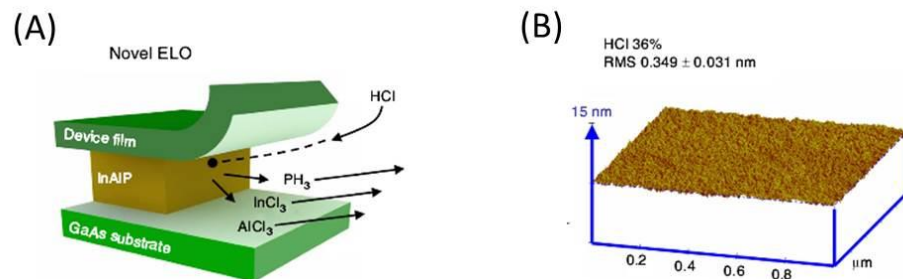


Figure 4.24: Premise behind epitaxial liftoff with phosphorus containing lift-off layers

After epitaxial lift-off is performed for the entire wafer, a contact metal is placed onto each pixel in the array, as illustrated in Figure 4.25.

7. Contact metal

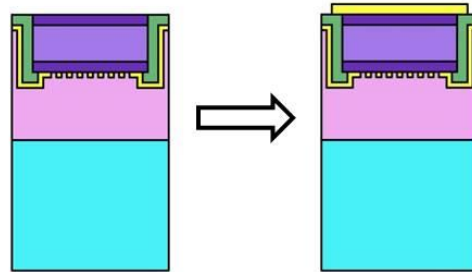


Figure 4.25: Metal deposition step to define a metal contact onto the bottom side of each pixel in the array

Next, the wafer containing the pixel array dies are diced and flip-chip bonded to a ROIC. After bonding the individual dies to the ROIC, an underfill epoxy is placed to help permanently bond the pixel array to the ROIC. Once bonded, the temporary bonding polymer is exposed to a highly selective solvent defined by its manufacturer. This temporary bonding polymer is designed to withstand all conventional cleanroom fabrication procedures except this highly selective solvent.

8. Hybridization

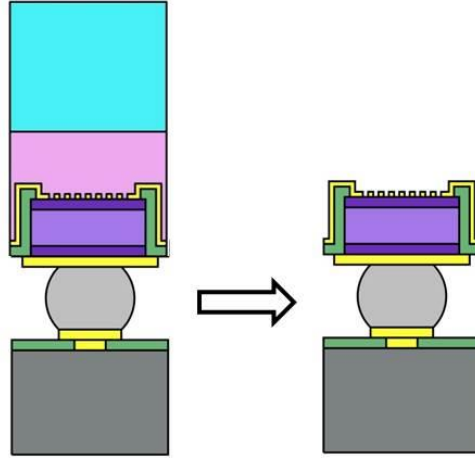


Figure 4.26: An advanced FPA bonded to a ROIC is exposed to a solvent to remove the temporary bonding polymer

4.4 Summary

In this chapter, we developed and presented the fabrication process of a conventional FPA. However, conventional FPA processing methods are not practical with next generation imaging systems on an industrial and metamaterial design level. As an attempt to find a solution to this problem, a prototype test chip was developed with a new FPA architecture. The pixels can incorporate ultra-thin doped semiconductor contacts for improved optical mode overlap with the active region of a photodetector. In addition, we replaced the highly doped semiconductor ground plane layer with a flexible metal layer for improved thermal cycle lifetime and optical isolation between pixels. Furthermore, we also demonstrated some advanced cleanroom processing methods through the development of flip-chip bonding, wafer polishing, highly selective dry etching, and backside patterning recipes. Although a significant amount of effort was required to achieve this prototype design, the fabrication process for this new FPA architecture is not perfect. In the remaining part of this chapter, we

discussed a highly advanced FPA design and fabrication process that addresses all FPA design issues for the fabrication of 4th generation FPAs. With this new method, we can perform all fabrication steps, including substrate removal, on the wafer level. Because we utilize a flexible handle wafer to achieve epitaxial lift-off of all the FPA dies, the option to reuse the substrate for crystal growth or continue wafer level processing on the pixel array is now possible. In addition, this method also enables metamaterial patterning as the first fabrication step for compatibility with many advanced lithography systems (nanoimprint, stepper, interferometric, etc.) that require whole, blank wafers for accurate pattern alignment and effective registration of small features. Advantages gained by this new FPA design and fabrication process is summarized and illustrated in Figure 4.27.

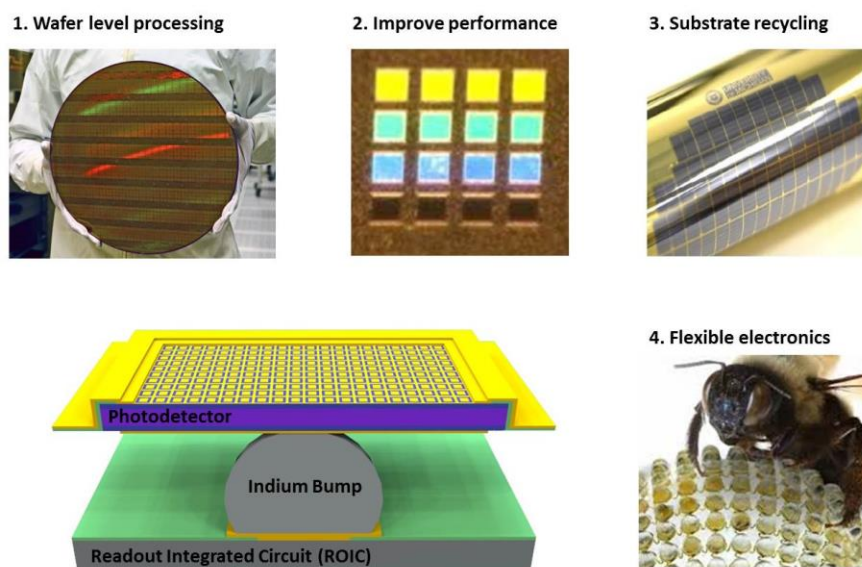


Figure 4.27: Advantages gained with the proposed FPA design and fabrication process.

These include wafer level processing, improved performance, substrate recycling, and a flexible ground plane

Chapter 5 : Metamaterial QWIP

Although infrared detector materials and design schemes have greatly improved over the years, the performance of detectors, in general, can be greatly improved with metamaterial absorber technology. A metamaterial absorber provides the advantage of selectively increasing the sensitivity of a detector at specific wavelengths. In section 5.1, we experimentally demonstrate a quantum-well-infrared-photodetector (QWIP) with a metamaterial pattern on its backside. The purpose of this work is to first demonstrate a metamaterial photodetector. Once this preliminary device is realized, we can then take design lessons from this metamaterial QWIP design and implement a metamaterial photodetector with much better performance (see Chapter 6). Some of these design issues for a QWIP include a low absorption coefficient, a thick semiconductor ground plane, a thick active region, and alloy Ohmic contact metal, which are all device characteristics that can result with low metamaterial photodetector performance. Many of these fabrication details are discussed in Chapter 4. In this chapter, we fabricate a QWIP based metamaterial photodetector as a preliminary proof of concept device and conclude with areas for improvement.

5.1 Detector Design

Here we fabricate a test chip with a metamaterial absorber cavity hybridized with a QWIP with a low absorption coefficient. The fabrication process is similar to the fabrication of a focal plane array (FPA) to provide accurate characterization and a rapid transition from test structure to a complete imaging system. In addition, substrate scattering in photodetector test structures that retain the substrate lowers the spectral selectivity of metamaterials, which makes it difficult to rapidly characterize metamaterial absorber designs. The photodetector

consists of a broadband QWIP design with many quantum wells that cover different regions of the infrared spectrum. In this design, infrared absorption results from quantum well ground state transitions to the continuum. The quantum well unit cell is composed of three quantum wells with a thickness of 3nm, 4nm, and 5nm. The quantum well unit cell is repeated 30 times with 50 nm $\text{Al}_{0.08}\text{Ga}_{0.92}\text{As}$ separation barriers.

QWIP Design

Layer name	Composition	Width (nm)	Doping (cm^{-3})	Repeat
Top Contact	GaAs (n doped)	200	$>2\text{e}18$	1
Barrier	$\text{Al}_{0.25}\text{Ga}_{0.75}\text{As}$	50	None	30
QW 3	GaAs (n doped)	5	$4.6\text{e}17$	30
Spacer 2	$\text{Al}_{0.25}\text{Ga}_{0.75}\text{As}$	8	None	30
QW 2	GaAs (n doped)	4	$4.6\text{e}17$	30
Spacer 1	$\text{Al}_{0.25}\text{Ga}_{0.75}\text{As}$	8	None	30
QW 1	GaAs (n doped)	3	$4.6\text{e}17$	30
Barrier	$\text{Al}_{0.25}\text{Ga}_{0.75}\text{As}$	50	None	1
Bottom Contact	GaAs (n doped)	1000	$>2\text{e}18$	1
Etch Stop	$\text{In}_{0.51}\text{Ga}_{0.49}\text{P}$	100	None	1
Buffer	GaAs	400	None	1

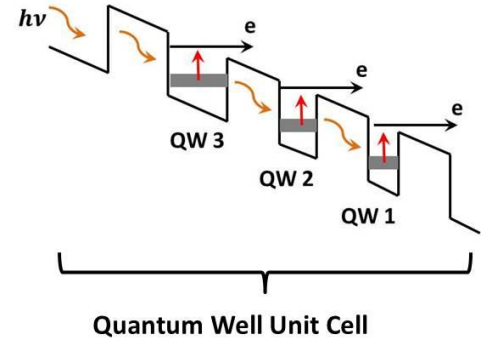


Figure 5.1: Broadband quantum well infrared photodetector design

A preliminary spectral response of the QWIP was obtained using a simple, front side wafer fabrication process. This process is advantageous for initial testing because its fabrication process is simple and a spectral response is quick to achieve. The chip was polished with a 45 degree facet, mounted on a 45 degree chip holder, and wire-bonded to a leadless chip carrier (LCC). Next, the LCC was loaded in a cryostat with a KBr window and cooled to 77K using liquid nitrogen. The wedge coupling geometry is shown in the inset of Figure 5.2. For a conventional QWIP, no significant s-polarized spectral response is observed since the QW has no in-plane confinement. However, the s/p polarized spectral response ratio of the

GaAs/AlGaAs QWIP device was measured to be 2.8%, which can be explained by the scattering caused by the edge of the device and the SI-GaAs substrate.

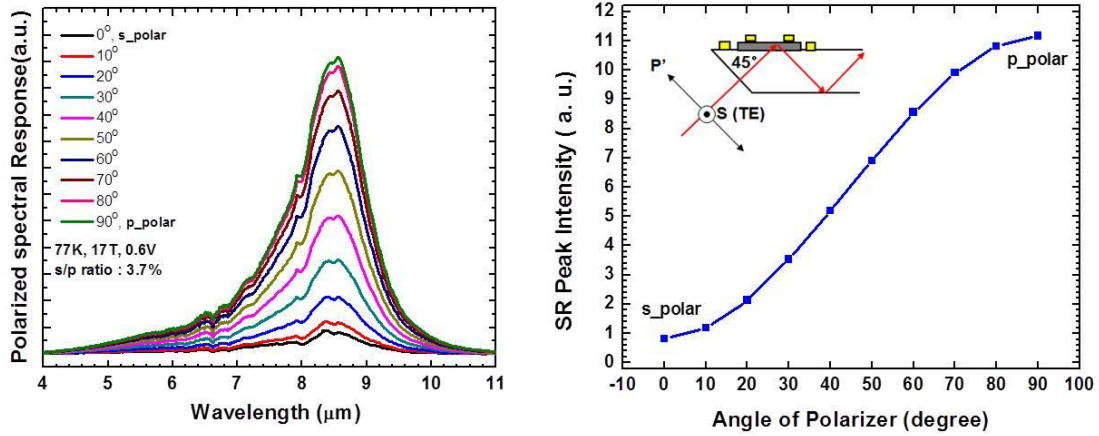


Figure 5.2: Spectral response of the QWIP with a 45 degree facet

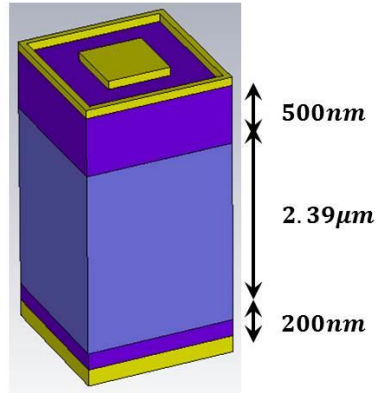
Next, a design simulation was undertaken for a QWIP with a metamaterial absorber cavity. To achieve this design, this requires the removal of the substrate below the epitaxial layer. The three components of this design are a backside metamaterial, an absorber and a ground plane. The backside metamaterial pattern is designed using a finite difference time domain (FDTD) simulator for determining the geometry of the backside pattern. The geometry of the pattern was varied to center the absorption peak of the metamaterial absorber with the absorption peak of the QWIP between 7 and 11 microns wavelength. The model also accounts for the doped contacts at both the top and bottom of the photodetector. In between the contacts, the active region is modeled as a lossy dielectric. The longitudinal absorption coefficient of the QWIP was estimated in the range of 1000cm^{-1} . Figure 5.3 is an illustration of the metamaterial photodetector design with permittivity and device geometry values.

Permittivity:

Top contact
 $\varepsilon = 9 + 0.1i$

Active region
 $\varepsilon = 9 + 0.36i$

Bottom contact
 $\varepsilon = 9 + 0.1i$



Design A: $A_x = 1.50\mu\text{m}$, $L_x = 1.35\mu\text{m}$, $W_x = 0.50\mu\text{m}$

Design B: $A_x = 1.75\mu\text{m}$, $L_x = 1.60\mu\text{m}$, $W_x = 0.75\mu\text{m}$

Design C: $A_x = 2.00\mu\text{m}$, $L_x = 1.85\mu\text{m}$, $W_x = 1.00\mu\text{m}$

Design D: $A_x = 2.25\mu\text{m}$, $L_x = 2.10\mu\text{m}$, $W_x = 1.25\mu\text{m}$

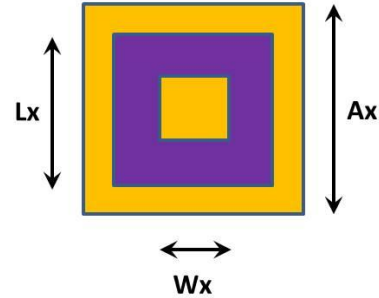


Figure 5.3: Simulated absorption coefficient for impedance matching the cavity to free space and simulated absolute absorption spectrum

For the wavelength range of interest, the resonant cavity design and a QWIP should be resonantly compatible to achieve a high degree of absorption to incoming radiation. To achieve this goal, various backside patterns are applied to achieve varying degrees of absorption efficiency. See Chapter 3 for an in-depth discussion on how to choose the correct backside pattern.

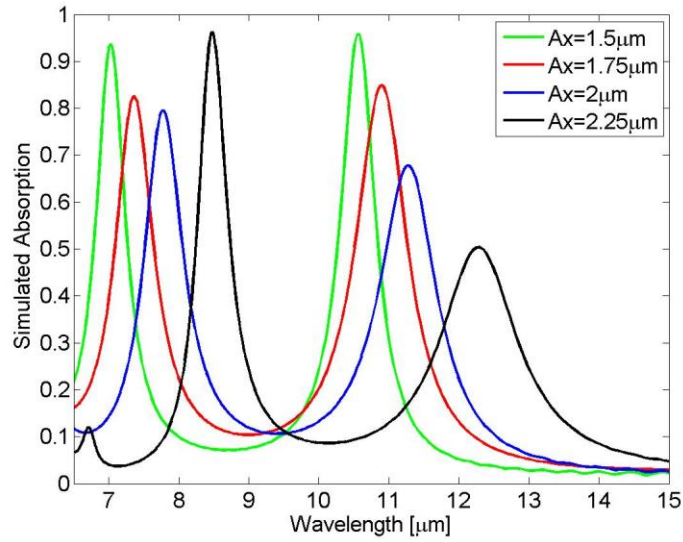


Figure 5.4: Simulated QWIP response with different backside patterns

5.2 Experimental Realization

Next, a test chip, with a similar fabrication process to an FPA, is fabricated. This test chip is hybridized to a silicon fanout to read signals from the QWIP pixels. The substrate is completely removed through a combination of mechanical polishing and selective etching. These fabrication steps are discussed in detail in Chapter 4. However, we discuss some specific fabrication steps here that affect the absorption efficiency of the metamaterial photodetector.

A thick, highly doped semiconductor ground plane is retained in this fabrication process because it's not possible to form an Ohmic contact onto the backside of a GaAs based pixel without performing a rapid thermal anneal, which would destroy the pixel array. Instead, we perform an Ohmic contact to the highly doped semiconductor ground plane before flip-chip bonding and substrate removal. The GaAs side that mates with a silicon control chip utilizes a 26nm Ge, 54nm Au, 15nm Ni, and 100nm Au metal layer to serve as

an Ohmic contact and metamaterial absorber ground plane. This Ohmic contact metal is not the best choice, but at the same time, highly conductive metals like gold, which represents a near ideal case for resonant electromagnetic cavities, do not easily form an Ohmic contact with GaAs. In order to form an effective Ohmic contact to draw photocurrent from the pixel, a rapid thermal anneal must be performed at 375C for one minute with the mentioned ground plane metals. Figure 5.5 is an example of Ohmic contact metal diffusing into the semiconductor contact region after a rapid thermal anneal is performed [72-73]. Obviously, this alloy metal will result with a significant amount of resistive power loss in the resonant cavity.

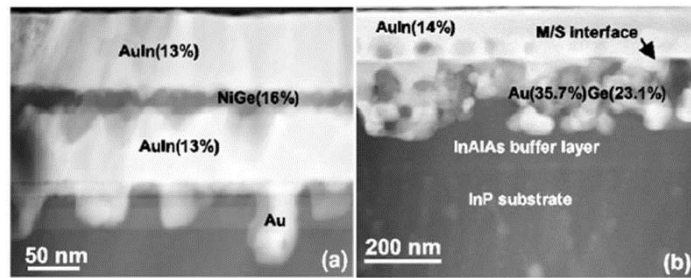


Figure 5.5: Z-contrast images of AuGe/Ni/Au Ohmic contact metal with different rapid thermal anneal temperatures: (A) 265C and (B) 300C [73]

After substrate removal, the illumination side of the pixel array is patterned with a metamaterial pattern with the aid of e-beam photolithography. The metallic patterns are composed of a thin 5nm layer of titanium and a 100nm layer of gold to reduce electromagnetic absorption in the metal layer. The thin titanium layer will also cause unwanted resistive power loss in the metamaterial photodetector design, so it's kept as thin as possible, but utilized to effectively adhere gold to the backside of the pixel array.

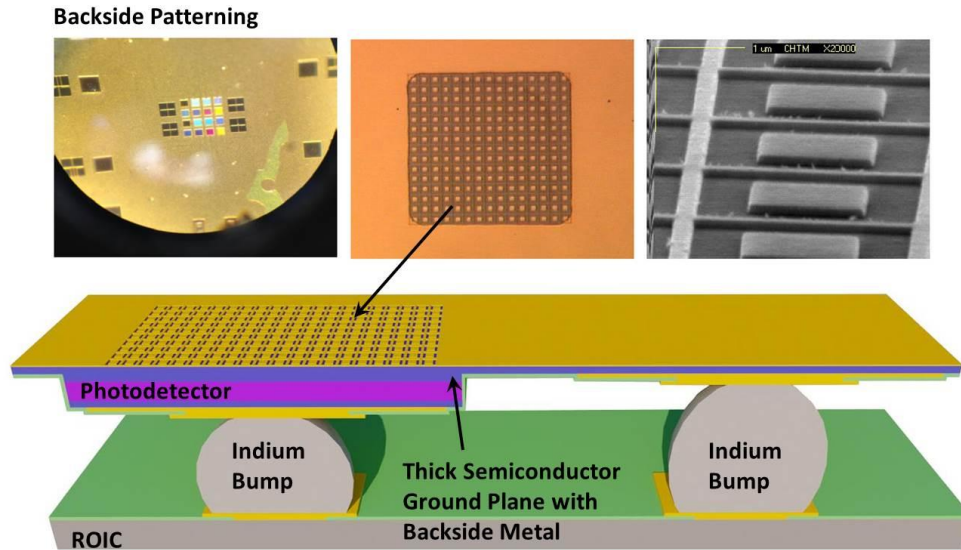


Figure 5.6: E-beam photolithography on the backside of the QWIP test chip

The metamaterial photodetector design implemented with a QWIP detector is not ideal because the thickness of the highly doped semiconductor contact is too thick for useful absorption in the active region of the detector to occur. The highly doped semiconductor contact layer is 500nm which weakens the effect of any penetrating field lines into the active region. This resulted in a very weak photocurrent response since a significant amount of the electromagnetic mode overlaps with the highly doped semiconductor contact layer. Nevertheless, a multispectral response from the device is shown in Figure 5.7 with good agreement between the simulated results and the experimentally obtained spectrum. Higher order modes are present, but these modes can be suppressed with more efficient metamaterial designs.

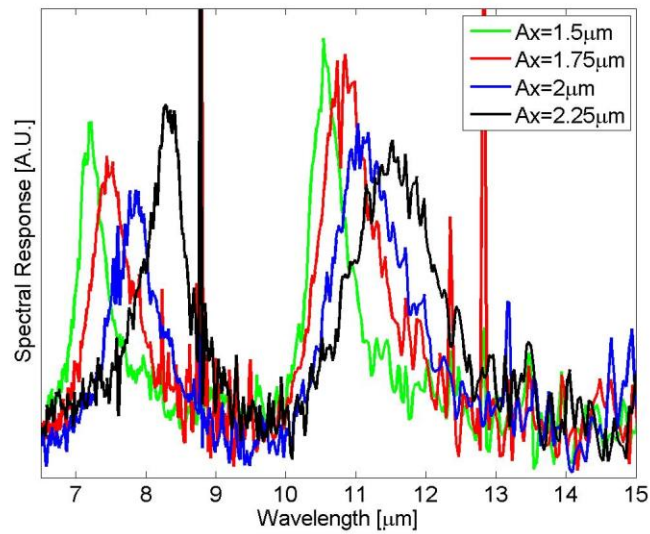


Figure 5.7: Measured photocurrent response of a metamaterial QWIP

The physics for why inefficient optical coupling occurs can be explained with the aid of Figure 5.8. If the thickness of the photodetector is too thick, field penetration tends to concentrate more towards the backside pattern and less in the active region of the photodetector. The backside pattern must be sufficiently close to the ground plane to draw in the electric field lines. However, if the backside pattern is too close to the ground plane, the field penetrates into the lossy metal, which can also result in lower photodetector absorption efficiency. If the absorption efficiency of the photodetector is plotted as a function of detector thickness, there is an optimum value. The fabricated photodetector is 2.39 microns thick where the optimum thickness should be 500nm for optimum absorption to occur in the active region of our photodetector. In addition, the thickness of the highly doped semiconductor ground plane should be significantly reduced to further increase field overlap with the active region of our infrared photodetector.

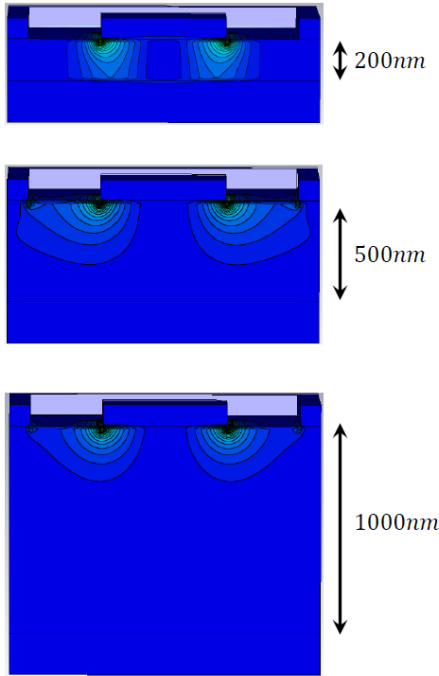


Figure 5.8: Electromagnetic field penetration and radiation absorption efficiency as a function of photodetector thickness

A quantum efficiency measurement was attempted for this QWIP metamaterial photodetector. However, its signal response was too low to measure with or without a band pass filter. Nevertheless, the signal from several QWIP metamaterial pixels were measured with an FTIR system, averaged 128 times, and compared in Figure 5.9. Spikes in the signal are due to a low signal-to-noise ratio. It can consistently be shown that the configuration used for optical enhancement for this QWIP was not achieved. Although this design did achieve some degree of spectral selectivity, this design reduced the amount of photocurrent produced when compared to the photodetector demonstrated in Figure 5.2.

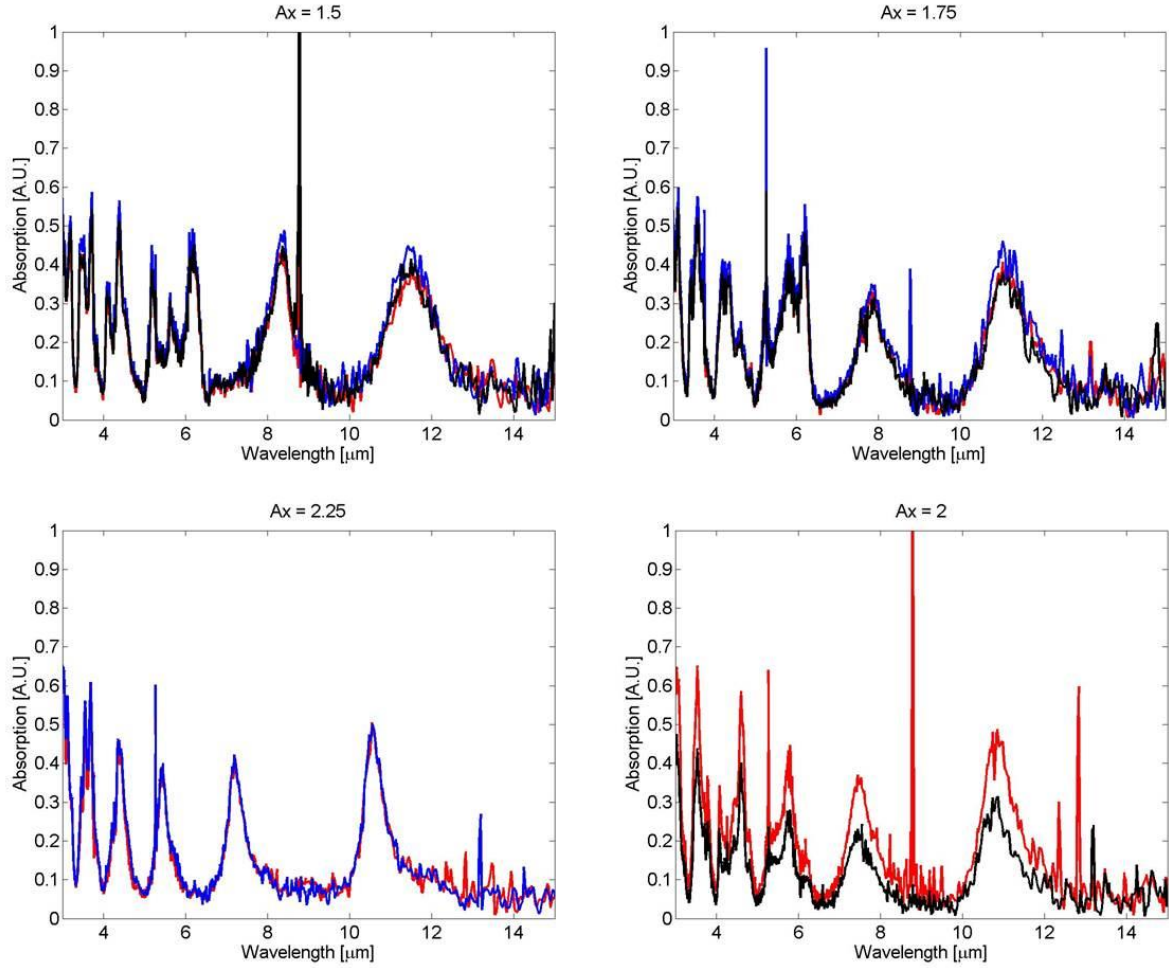


Figure 5.9: Photocurrent response of multiple pixels with each graph containing multiple photocurrent measurements of pixels with the same backside pattern

5.3 Summary

A metamaterial absorber design was proposed and fabricated to demonstrate a metamaterial absorber hybridized with a QWIP detector. The fabrication process is similar to an FPA to allow accurate device measurement for its rapid integration into an infrared imaging system. However, there are many design limiting issues with QWIP detector technology that prevent their effective hybridization into a metamaterial absorber cavity. The first issue is that an alloy Ohmic contact is required to achieve an electrical connection with low resistance. This

metal alloy can contribute to electromagnetic losses in our metamaterial absorber cavity, which reduces the detectors ability to achieve a high degree of useful absorption (or enhanced quantum efficiency). In addition, the thickness of the photodetector needs to be optimized for efficient optical enhancement to occur. However, photodetector thickness is limited by the thickness of its highly doped semiconductor ground plane. This thick semiconductor ground plane is required to define the pixel array as discussed in Chapter 4. As a result, a significant amount of radiation is lost to this layer. Also, a thick photodetector reduces electromagnetic field coupling with the ground plane, which ultimately reduces field penetration into the active region of our photodetector. A new fabrication process should be implemented to overcome these design issues.

Chapter 6 : Metamaterial Type II Superlattice

The ability to obtain spectral information from a scene is a highly sought after goal, especially in the infrared (2-20 μm) where spurious reflections and thermal emission make it difficult to realize a robust imaging system [74]. Here we design, fabricate and demonstrate the first deep-subwavelength multispectral infrared detector using an ultra-thin Type II superlattice (T2-SL) detector coupled with a metamaterial resonator with high quantum efficiency. Unlike a conventional filter, the spectral response is not attenuated but is *enhanced by 7X* compared to the reference detector. The quantum efficiency of the ultra-thin ($\lambda/20$) detector increased from 2.4% to 17% at a peak operating wavelength of $4.78\mu\text{m}$. This detector eliminates the complex optics network with moving filters or dispersive elements and avoids spatial and temporal registration problems, thereby decreasing the cost and size of the imaging system. This demonstration paves the way for the realization of a bio-inspired infrared retina.

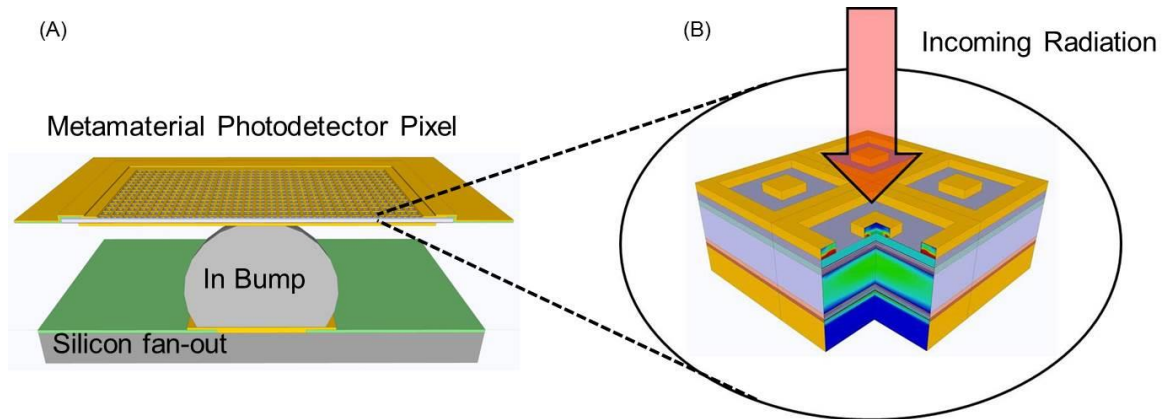


Figure 6.1: (A) 375nm thick infrared photodetector pixel (B) Power loss density profile of a few metamaterial absorber unit cells that results from incoming radiation

6.1 Detector Design

In this work, we use a hybrid metamaterial (MM) that consists of an ultrathin infrared photodetector sandwiched between an impedance-matched patterned surface and a metallic ground plane, as shown in Figure 6.1. Metamaterial theory provides a set of tools so that the real and imaginary part of the effective permittivity ($\epsilon(\omega)$) and permeability ($\mu(\omega)$) can be engineered to minimize the reflection and transmission, thereby maximizing the absorption for certain wavelength ranges. Using different patterns on the surface, a detector chip with 3-colors on an ultrathin broad band T2-SL detector was demonstrated. Instead of an attenuation of the signal (as in the case of conventional filters), the quantum efficiency (QE) was enhanced 7X compared to the reference detector. At T=77K, the QE increased from 2.4% for the bare detector ($\sim 4\text{-}5.8\mu\text{m}$) to 12.5% for λ_1 ($5.1\mu\text{m}$), 15.4% for λ_2 ($4.9\mu\text{m}$) and 17% for λ_2 ($4.78\mu\text{m}$).

The detector used for this work was based on an interband cascade design implemented using InAs/GaSb superlattices. InAs/GaSb SLS material is characterized by the broken-gap type-II alignment, with electrons and holes localized in InAs and GaSb layers, respectively. The overlap of electron (hole) wave functions between adjacent InAs (GaSb) layers results in the formation of an electron (hole) minibands in the conduction (valence) band. Optical transition between the highest hole (heavy-hole) and the lowest conduction minibands is employed for the detection of incoming IR radiation. The interband cascade design has been recently used to demonstrate high operating temperature detectors and FPAs [75-76]. A single stage interband cascade detector with a 235 nm absorber sandwiched between a hole barrier (43nm) and an electron barrier (33 nm) was grown using molecular beam epitaxy (heterostructure schematic in Figure 6.2). A square loop design was chosen for

the patterned surface and the frequency was changed by varying the length of the square. FDTD simulations were undertaken to obtain the distribution of the incident energy in various regions of the metamaterial photodetector. Based on our simulations, we see an optimum response around $a = 200\text{nm}$ for a photodetector with an absorption coefficient in the range of 3500cm^{-1} .

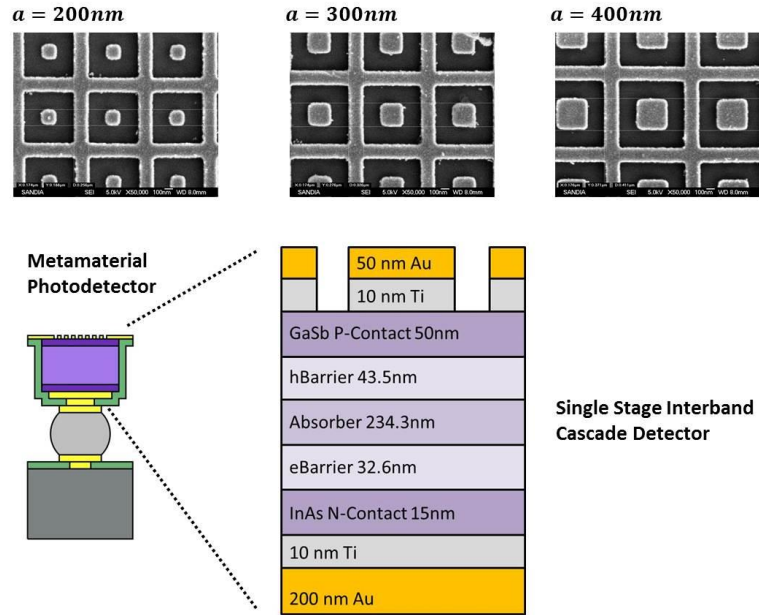


Figure 6.2: Heterostructure schematic of the Interband Cascade Detector and SEM images of the backside of each fabricated pixel with varying geometry

6.2 Experimental Realization

The detector array was fabricated using conventional cleanroom processing techniques and flip-chip bonded to a silicon fanout which allowed an electrical contact to each pixel. The substrate was removed using chemical mechanical polishing and the metamaterial pattern was undertaken using electron-beam lithography. Figure 6.2 also shows the image of the fabricated detector and the scanning electron microscope images of the pattern.

Although there have been several reports of “perfect absorption” using a metamaterial geometry, perfect absorption is a necessary but not a sufficient condition for “perfect detection”. For perfect detection, the “useful absorption” which is the absorption in the dielectric as opposed to the loss in the metal or background has to be maximized. In our experiments, the total absorption was measured using an infrared microscope coupled with a cooling stage and the useful absorption was measured using the photocurrent. Figure 6.3(a) shows the total absorption obtained from the detectors using the IR microscope and Figure 6.3(b) shows the quantum efficiency extracted from the photocurrent.

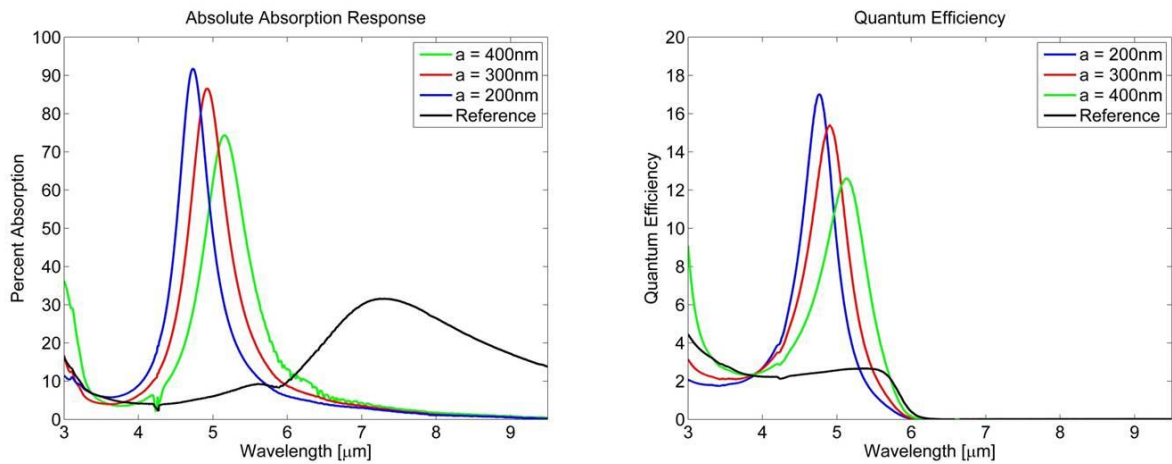


Figure 6.3: (a) Total absorption obtained from the detectors using an IR microscope and (b) quantum efficiency extracted from the photocurrent.

Note that even though the total absorption in the structures could be as high as 90%, the useful absorption was limited to 17% (assuming that the photoconductive gain in these devices is one). Thus the background absorption could be as high as 70%. Note that the even though there is background absorption in the reference detector at $\sim 7\mu\text{m}$ (probably due to free carrier absorption), there is no “useful absorption” or photocurrent at that wavelength.

This work also illustrates that there is an intricate relationship between the required absorption coefficient for critical tuning and the geometry of the resonant cavity. In the design of the meta-infrared detector, the absorption of all incoming radiation must be maximized to meet the full potential of the metamaterial perfect absorber to enhance a photodetector's performance. The absorption efficiency of a metamaterial perfect absorber is determined by the absorption coefficient of the encased dielectric layer. If the absorption coefficient is too low or too high, a significant amount of reflection occurs, which reduces the amount of incoming radiation absorbed. The absorption coefficient of the encased dielectric layer must be critically tuned to achieve perfect absorption. Figure 3.13 shows that for a given loss tangent (absorption coefficient), perfect absorption can be obtained. However, near perfect detection can only be obtained when the absorption coefficient of the detector is large enough to mitigate the background absorption.

6.2.1 Specific Detectivity Measurement

As illustrated in Figure 6.4, the specific detectivity for our metamaterial photodetector was measured for the geometry $a = 200\text{nm}$, $a = 300\text{nm}$, $a = 400\text{nm}$ and a reference pixel with no backside pattern. This measurement was performed at 78K with an applied detector bias of -10mV. Detectivity was calculated using dark current density to estimate Johnson and shot noise, as described in Chapter 2, because of difficulties in accurately measuring detector noise. For the optimized metamaterial photodetector geometry ($a = 200\text{nm}$), the Detectivity increased 7x from $\sim 2 \times 10^{11} \text{ cmHz}^{1/2}/W$ from $\sim 3 \times 10^{10} \text{ cmHz}^{1/2}/W$ for a device without a backside pattern.

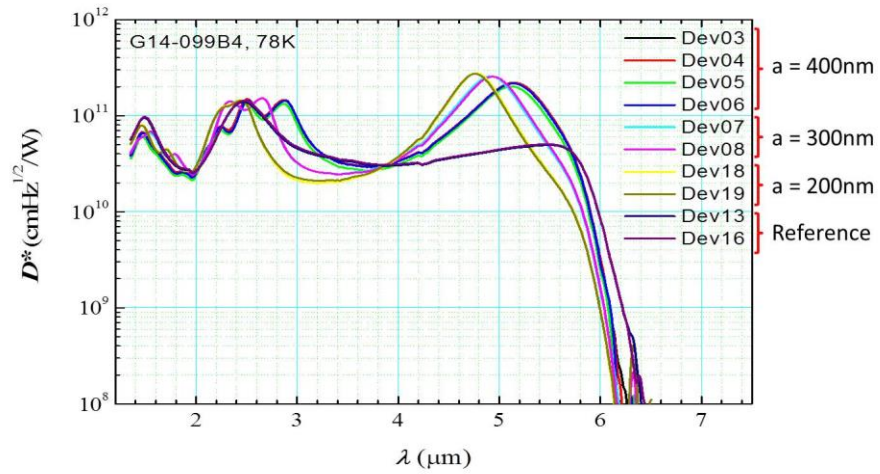


Figure 6.4: Specific detectivity measurement for metamaterial detector geometries $a = 200\text{nm}$, $a = 300\text{nm}$, $a = 400\text{nm}$ and a reference pixel with no backside pattern

6.2.2 Dark Current Measurement

Dark current measurements were conducted on all detector pixels and the Arrhenius behavior was then plotted in order to analyze the current limiting mechanism. This measurement was performed at a temperature of 78K, which is the same temperature for our quantum efficiency measurements. In Figure 6.5, we plot our dark current measurements as a function of applied bias. It can be seen from this figure that dark is relatively consistent across all detectors.

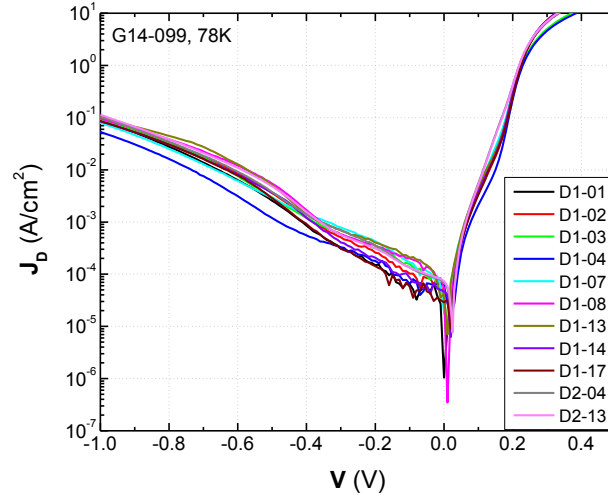


Figure 6.5: Dark current measurement for all detector pixels to demonstrate a consistent response

An Arrhenius plot, computed in Figure 6.6, is used to determine the limiting dark current mechanism for our detectors. For instance, the slope of the curve is the activation energy, E_A , which can indicate the limiting current mechanism.

$$J \propto \exp\left(\frac{E_A}{kT}\right)$$

If E_A is approximately equal to the band gap energy of the absorber material, diffusion dark current is the limiting mechanism. If E_A is approximately half of the band gap energy, then the limiting mechanism is Shockley-Read-Hall. If E_A is on the order of ten percent of the band gap energy, then the limiting mechanism tends to be tunneling or surface leakage current. It can be seen from Figure 6.6 that E_A is relatively flat, suggesting that the limiting dark current mechanism is either tunneling or surface leakage current.

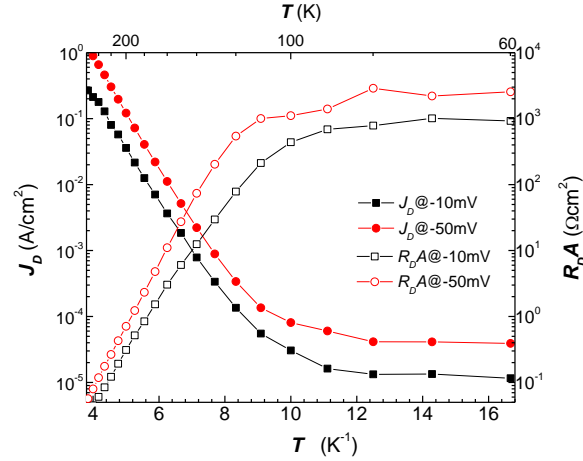


Figure 6.6: Arrhenius plot of a thin interband cascade photodetector

6.3 Summary

In this chapter, we experimentally demonstrate an interband cascade photodetector with a type II superlattice absorber as a material system for next generation imaging with metamaterial designs. We implement our metamaterial design scheme to optimize the absorption of incoming radiation to an infrared photodetector. Unlike a conventional filter, the spectral response is not attenuated but is *enhanced* by 7X compared to the reference detector. The quantum efficiency of the ultra-thin ($\lambda/20$) detector increased from 2.4% to 17% at a peak operating wavelength of $4.78\mu m$. This detector eliminates the complex optics network with moving filters or dispersive elements and avoids spatial and temporal registration problems, thereby decreasing the cost and size of the imaging system. In addition, we perform quantum efficiency and absolute absorption measurements to approximately determine background radiation losses for a metamaterial photodetector.

Chapter 7 : Vision for a Dynamic IR Photodetector

Next generation imaging systems require two distinctive features that current systems don't offer, which are 1) pixel-level tunable bias and 2) built-in analog signal processing units. These unique features have the potential to fundamentally change the way that data-exploiting and post-processing imaging are developed. Currently, to create a desired spectral response, multiple images must be taken of the scene. Utilizing the pixel-level tunable bias, one can take multiple spectral responses within one frame. Therefore, the overall spectral response can be generated with only a few frames, which can potentially improve the speed of image classification by an order of magnitude.

Unlike existing imaging systems, a *smart imager* should perform most image processing algorithms with integrated hardware on the pixel level. In addition to the large simplification of the optical system, a smart imager with dynamic sensing provides complete spectral adaptivity. All spectral sensors that are currently available are designed to perform a specific and static spectral sensing mission. A spectrally dynamic response would allow a single camera system to be used for panchromatic imagery, multi-color imagery at arbitrary wavelengths, multispectral imagery with arbitrary numbers, locations, and widths of spectral bands, and coarse resolution hyperspectral imagery. The additional features in *smart imager* technology provides enormous flexibility to the electronic imaging systems which allow us to implement novel image processing algorithms that wouldn't be possible using existing systems. Such algorithms includes: 1) the possibility that different portions of the FPA could perform different spectral tasks simultaneously, 2) the ability to obtain a nearly-arbitrary spectral response that provides the promise for real-time, adaptive matched filtering, and 3)

the possibility of a fast and low power hyperspectral remote sensing hardware to create images that highlight particular spectral features of interest.

In recent years, quantum-dot-in-a-well (DWELL) photodetectors have proven their applicability as dynamic spectrometers for object classification [77]. The goal here is to extend their applicability to a high quantum efficiency Type II superlattice (T2-SL) photodetector with a spectrally tunable metamaterial layer for multicolor sensing. To achieve dynamic spectral sensing on the pixel level, an electrically tunable metamaterial can be integrated with a broadband SL infrared photodetector. The spectral tuning of the metamaterial is continuously controllable by means of varying the applied voltages to the metamaterial pattern. Hence, a single metamaterial can be thought of as a spinning-wheel spectral filter, albeit with highly overlapping spectral bands.

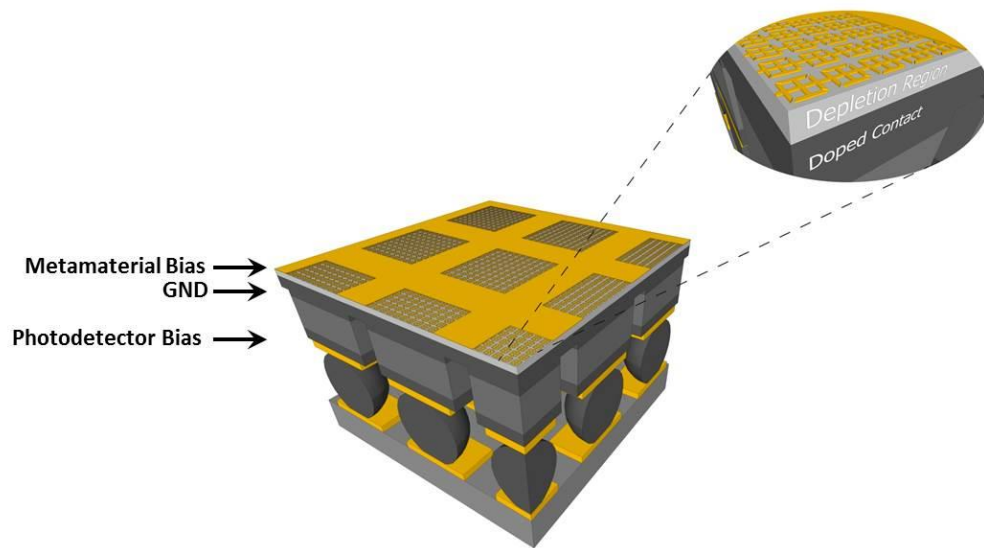


Figure 7.1: Dynamic metamaterial photodetector concept

A dynamic metamaterial integrated with a broadband infrared photodetector, shown Figure 7.1, is designed to control the carrier concentration below the metamaterial pattern with an

applied voltage to ultimately control the spectral response of the photodetector. If the carrier concentration is varied over a wide range of values, this can result with an optical filter with a fairly wide range of sensing capability. In addition, the applied voltage for the detector and the depletion region are separated by utilizing an electrical contact for each region for independent operation of each structure. To demonstrate a multicolor, dynamic semiconductor metamaterial, we designed our resonator to operate in the terahertz frequency regime due to some design implementation advantages. Once demonstrated, new design schemes can be implemented for their operation in the infrared for dynamic spectral sensing with a broadband photodetector. In section 7.1, we discuss the design and implementation of a dynamic terahertz spatial light modulator.

7.1 Dynamic Terahertz Spatial Light Modulator

The control of fundamental electromagnetic (EM) processes at surfaces – transmission, reflection and absorption – has a long and glorious past. From camouflage and stealth technology to energy harvesting and skin cancer detection, the ability to tailor the EM response at interfaces has had an enormous impact on society. Here we have created a spatial light modulator (SLM) with multi-color super-pixels composed of arrays of electronically controlled terahertz (THz) MMAs with modulation depths of up to 50 percent, frequency tunability greater than 5 percent. The device created here shows that fundamental light interactions of surfaces can be electronically controlled and provides a path forward for future designs.

Terahertz (THz) technology has been steadily growing in recent years, however, the devices and components necessary to efficiently manipulate THz radiation remain in need of substantial development to be able to provide effective solutions for a range of applications

[78]. Efforts at creating frequency agile and tunable metamaterials have been demonstrated and various methods utilized to achieve amplitude and frequency modulation at THz frequencies including photodoping [79], electronic charge injection [80], temperature control [81] and microelectromechanical systems (MEMS) [82]. The capability to control light dynamically, spatially, and or spectrally has shown numerous potential advantages; specifically with regards to spectroscopic and imaging applications [83-85]. Commercially available digital micro-mirror [86] and liquid crystal [87] based devices have shown great promise from the near-IR (NIR) to UV, but tend to no longer function towards longer wavelengths [83,88]. Obtaining spatio-spectral data with these devices can be challenging requiring complex, high cost equipment and instrumentation with significantly limited acquisition speeds [84]. If these devices had integrated control of spatial and spectral information at the device level this would offer significant improvements and advantages in a wide area of potential uses. Metamaterials, whose electromagnetic behavior can be tuned dynamically, as well as be made to be both frequency and spatially selective [89], are attractive candidates to bridge these challenges. Here we demonstrate for the first time by combination doped semiconductor and metamaterials, a SLM with multi-color super-pixels composed of arrays of electronically controlled THz MMAs.

7.1.1 Design and Fabrication

The THz MMA-SLM presented here is shown in Figure 7.2 and is composed of a pixelated MMA arrays, arranged to form a square lattice of 8 by 8 pixels. The pixels are tiled in a similar fashion to conventional RGB color schemes, with modulation at four unique THz frequencies. The overall SLM system architecture is schematically shown in Figure 7.2b and consists of MMA pixels flip chip bonded to a silicon chip carrier with routing to bond pads

which are wire-bonded to a leadless chip carrier (LCC). Individual pixels are biased through a commercial 64 channel FPGA.

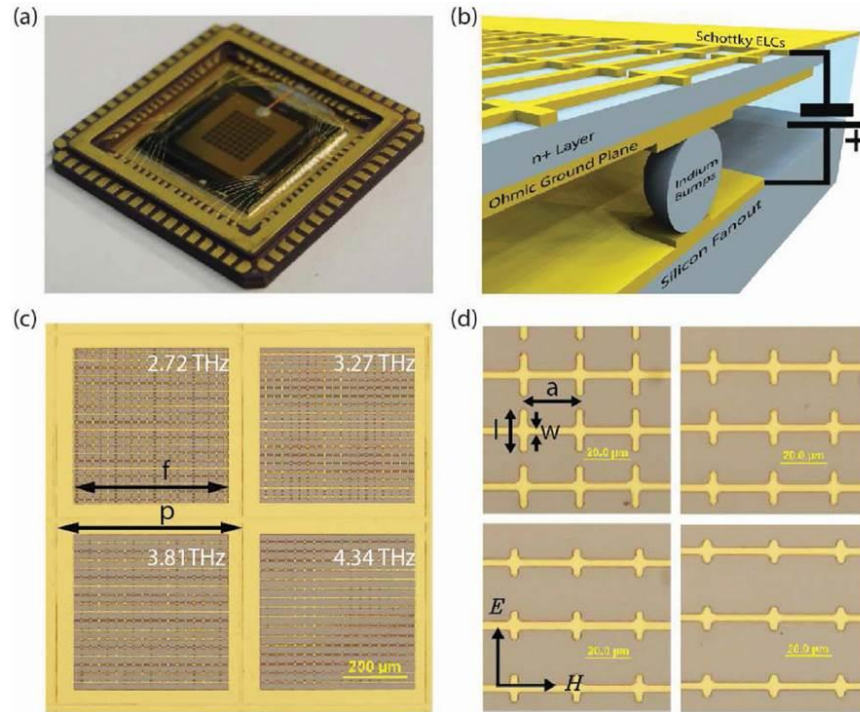


Figure 7.2: Design and structure detail of the electronically controlled THz metamaterial absorber based spatial light modulator (MMA-SLM). (a) Image of MMA-SLM as assembled in chip carrier package. (b) Schematic depicting the entire MMA-SLM device. (c-d) Optical microscope images for each color pixel with dimensions as listed in Table 7.1.

MMAs typically consist of two metallic layers spaced apart by a dielectric spacer. The top metal layer is geometrically patterned in order to strongly couple to a uniform incident electric field. By pairing the top layer with a metal ground plane, a mechanism for coupling to the magnetic component of light is created – see Figure 7.2b. Altering the geometry of the metallic pattern and dielectric thickness enables tuning of the effective material response parameters allowing for both impedance matching and strong absorption at nearly any desired frequency. Here we have modified the conventional MMA and utilized a 2

μm ($< \lambda/35$) thick n-doped ($2.0 \times 10^{16} \text{ cm}^{-3}$) epitaxial layer of GaAs as the dielectric spacer as depicted in Figure 7.2b. We form a Schottky junction by having the ELCs serve as the Schottky contact and the bottom ground plane as the Ohmic contact. This configuration enables depletion of carriers in the epitaxial layer underneath the ELCs as a function of applied reverse bias, resulting in tunability and modulation of the electromagnetic absorption.

A schematic and optical microscope image of the device are shown in Figure 7.2c,d with each color pixel having dimensions as listed in Table 7.1. Electric isolation to ensure independent pixel modulation is achieved by discretizing the ground plane, forming small gaps between neighboring pixels in conjunction with defining mesas through the epitaxial layer around each pixel. The ELC unit cells are connected to their neighbors via horizontal metallic wires. The pitch of the array pixels, p , is $600 \mu\text{m}$, with total ELC array size slightly varying for each respective frequency, providing a fill factor approximately equal to 65%. The continuous metal boundaries between ELC arrays enable a single contact to be made for entire Schottky layer. The square ground plane is centered about each pixel has a side length of $570 \mu\text{m}$ with the mesa lying between having a width of $10 \mu\text{m}$.

Table 7.1: The dimensions for each frequency (THz) color pixel as relating to Figure 7.2c,d. The line width w is $3 \mu\text{m}$ and the pixel pitch p is $600 \mu\text{m}$ are held constant for each pixel design.

dimension [microns]	2.72 THz	3.27 THz	3.81 THz	4.34 THz
a	25	27	28	30
l	19.2	15.2	12.5	10.6
f	500	486	476	480

7.1.2 Results and Discussion

In Figure 7.3a-d we show the measured reflectance $R(\omega)$ as a function of frequency for both the unbiased and for reverse bias $V_{\text{bias}} = -26.5 \text{ V}$. For the unbiased case, the channel has a maximum carrier concentration in the GaAs epitaxial layer n_{GaAs} , as the V_{bias} is increased, continued depletion in the n_{GaAs} results in the reflection minimum red shifting monotonically until saturating as shown for each color pixel in Figure 7.3e. A maximum $V_{\text{bias}} = -26.5 \text{ V}$ results in sufficient depletion of n_{GaAs} to shift the frequency of the reflection minimum by nearly 5% in the case of the lowest color frequency pixels. As the reflection minimum redshifts, the reflection minimum value decreases between the two bias conditions, with the largest decrease occurring at lower frequencies where the reflection minimum decreases by up to 12%. In many applications one may desire amplitude modulation only over a narrow band. As an example we consider operating at a fixed frequency ω_0 , i.e. the minimum reflection response of the unbiased case. In Figure 7.3f we plot $R(\omega_0)$ as a function of V_{bias} for each color pixel. We observe that the reflection level increases as a

function of increasing V_{bias} which appears to saturate upon approaching the breakdown threshold. The doped semiconductor layer thus provides an all electronic means of both frequency and amplitude tuning of the reflection minimum of metamaterial absorbers and here we realize an amplitude tuning at the lower frequency color pixels of over 30%.

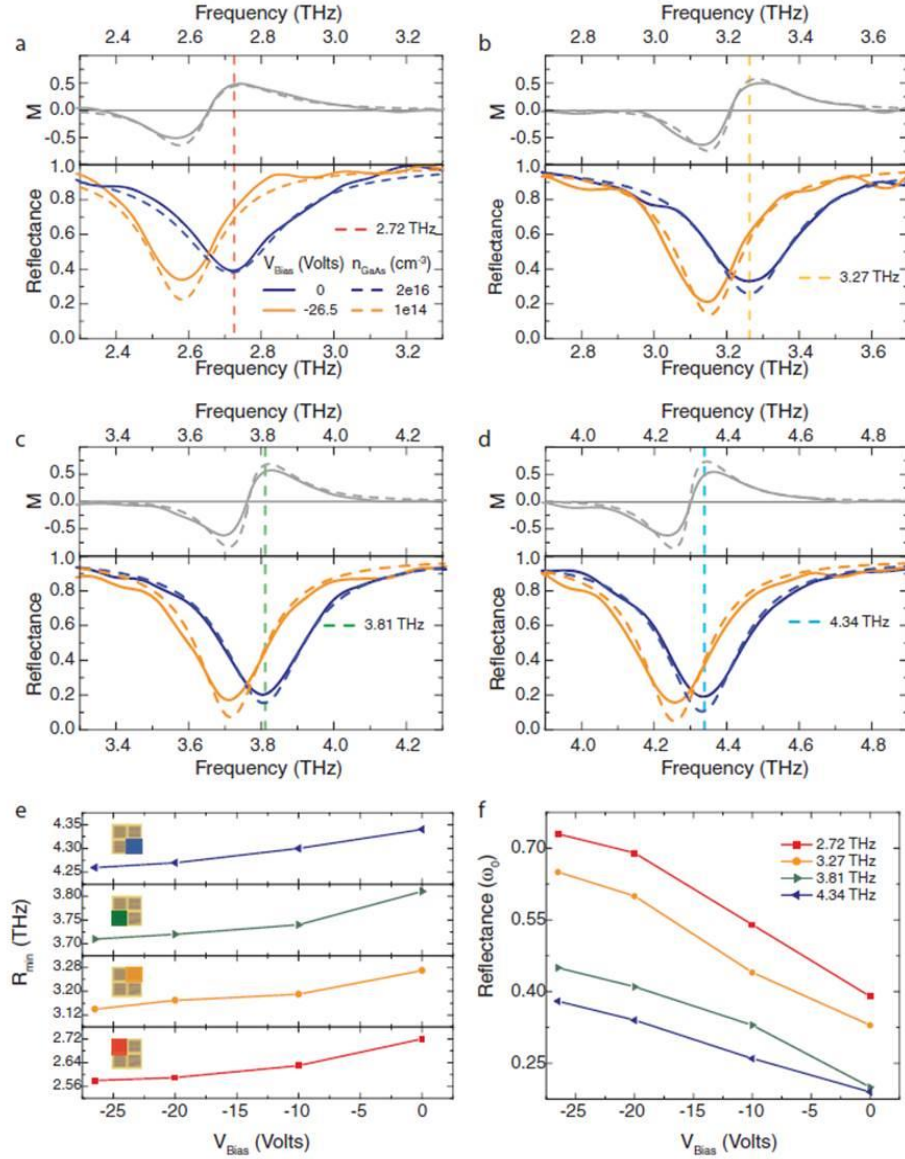


Figure 7.3: Experimentally measured and computationally simulated frequency dependent reflectance and modulation index (defined in the text) of the metamaterial absorber shown for each color sub-pixel. (a–d) (Bottom panels) The experimental curves are shown for

applied bias voltage V bias equal to both 0 V (blue) and -26.5 V (gold), with the simulated curves shown for carrier concentration of the n-doped GaAs epitaxial layer n GaAs equal to $2.0 \times 10^{16} \text{ cm}^{-3}$ (blue dashed) and $1.0 \times 10^{14} \text{ cm}^{-3}$ (gold dashed). (Top panels) Simulated modulation index are shown as the dashed gray curves in the top panels of (a–d). The colored vertical dashed lines indicate frequency of the unbiased reflectance minimum, $R_{\min}(V \text{ bias} = 0) = \omega_0$, for their respective sub-pixels. (e) Frequency location of R_{\min} as a function of V bias for each color subpixel, color shading on inset image indicates location within the super-pixel. (f) The reflectance values $R(\omega_0)$ for ω_0 as indicated by the vertically dashed color lines in Figure 7.3a d, shown as a function of V bias for each color sub-pixel.

In order to clarify the mechanism underlying operation of the tunable absorber, we perform full wave 3D electromagnetic simulations. Recent dynamic studies have looked at the convolution between the semiconductor device physics and the electromagnetic response of metamaterials [90]. We model the frequency dependent dielectric permittivity of the epilayer $\tilde{\epsilon}_{GaAs}(\omega)$ using Drude theory where at THz frequencies n-doped GaAs has been well characterized for similar doping levels [91-92]. We approximate the depletion to be directly underneath the Schottky junction formed at the Au:GaAs interface, and at max bias, to be sufficiently depleted across the $2 \mu\text{m}$ thickness. The results from our computational model are plotted as the dashed curves in Figure 7.3a-d and show excellent agreement with experiment as n_{GaAs} depletes down from $2 \times 10^{16} \text{ cm}^{-3}$ to $1 \times 10^{14} \text{ cm}^{-3}$ the tunability in the absorption saturates.

The device performs collectively as a SLM and we characterize individually the absorption tunability for each pixel. In Figure 7.4a the spatial mapping of the maximum

absolute change in reflectance $|\Delta R(\omega)| = |R_{-26.5V}(\omega) - R_{0V}(\omega)|$ is shown. The corresponding frequency at which the maximum occurs is similarly displayed in Figure 7.4b. The device demonstrates tunable reflectance that spans from 25 to over 50 percent change in total reflectance. The 2×2 multi-color subarrays are replicated across the entire 8×8 spatial array. The two shorted pixels are displayed as black, which along with the reflecting boundary between pixels, are spectrally unmodulated.

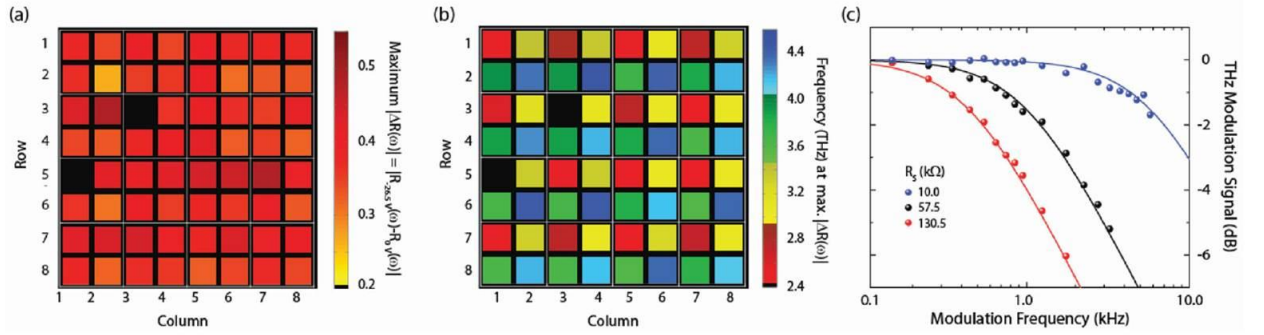


Figure 7.4: Spatial light modulator performance. (a) Magnitude of the maximum change in reflectance shown for each pixel. (b) The corresponding frequency for each pixels respective magnitude response. (c) The modulation frequency response of a typical pixel with an in series resistor

The modulation speed of the device was measured and the results are shown in Figure 7.4c. We measured the device RC time constant as done in previous studies [98] by loading with an external series resistor, allowing for the extraction of the device capacitance and the resulting 3 dB roll-off frequency f_c of 10 MHz. The reduction in device capacitance as compared to previous metamaterials designs [80,98] is a result of having the Ohmic ground plane directly underneath the Schottky layer, providing an optimal configuration for minimal device capacitance for high speed modulation. Another added benefit of having the Ohmic ground plane underneath is that routing on the silicon carrier is shielded from incident THz

radiation allowing for higher filling factors as well as the ability to accommodate larger array sizes.

7.2 Experimental Methods

The frequency dependent reflection $[R(\omega)]$ was characterized at an incident angle of 20 degrees from 2 to 10 THz using a Hyperion-2000 infrared microscope connected to a Fourier-transform infrared spectrometer, Hg-arc lamp source, liquid helium-cooled silicon bolometer detector, and a germanium coated 6 μm mylar beamsplitter. The measured reflection spectra are normalized with respect to a gold mirror with square metal apertures set to 450 μm on each side. Since the transmitted intensity was zero due to the metal ground plane, this measurement was not required. Measurements were performed with the THz electric field perpendicular to the metal connecting wires, as depicted in Figure 7.2d. The DC potential between the ERR Schottky metal layer and the Ohmic ground plane is a reverse bias voltage (V_{bias}) as shown in Figure 7.2b.

We characterized the electrical performance of the SLM by running voltage dependent current (IV) profiles for all 62 functioning pixels. The resulting mean and standard deviation are shown in Figure 7.5 and is comparable to previous investigations. The breakdown voltage occurs just beyond the maximum bias swept with the knee of the IV curve occurring close to $V_{\text{bias}} = -23 \text{ V}$.

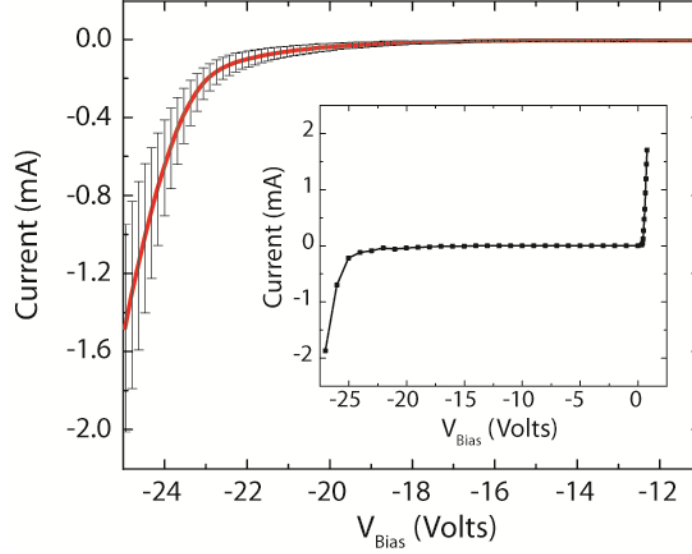


Figure 7.5: Voltage dependent current (IV) profile shown with the standard deviation plotted as the error bars for the 62 functioning pixels. The inset plot shows a single pixel's IV curve including forward bias.

7.3 Electromagnetic Simulation

We model each color pixel using commercial finite difference time domain (FDTD) solver, CST's Microwave Studio. We define both the ELC and ground plane metal layers as a lossy metal with DC conductivity value $\sigma_0 = 4.5 \times 10^7$ S/m. For the n-doped GaAs epi-layer, whose frequency dependent permittivity $\tilde{\epsilon}_{GaAs}(\omega)$ is modeled by a Drude model [91-92], we define three separate volume regions: the unbiased depletion, the maximum bias depletion, and the non-depleted region as depicted in Figure 7.6c,d.

The dielectric permittivity of GaAs has been shown to be well described within the framework of the Drude model for the conductivity at THz frequencies. The model can be written as the following:

$$\tilde{\epsilon}_{GaAs}(\omega) = \epsilon_{\infty} + \frac{\omega_p^2}{\omega(\omega - i\gamma_c)}$$

Where $\epsilon_\infty \approx 12.9\epsilon_0$ is the dielectric constant of undoped GaAs and $\epsilon_0 = 8.85 \times 10^{-12}$ F/m is the vacuum permittivity, ω_p is the plasma frequency, and γ_c is the collision frequency. ω_p is dependent of the free carrier concentration n_{GaAs} :

$$\omega_p^2 = \frac{n_{GaAs} q^2}{\epsilon_0 m^*}$$

Where $q = 1.6 \times 10^{-19}$ C is the elementary charge, and $m^* = 0.067m_0$ is the effective mass of n-doped GaAs and $m_0 = 9.11 \times 10^{-31}$ kg is the ordinary mass of an electron. γ_c is dependent on the carrier mobility ν :

$$\gamma_c = \frac{q}{m^* \nu}$$

Studies show that μ is strongly dependent on the doping level N_d with μ values up to 6500 cm²/Vs reported at $N_d = 2 \times 10^{16}$ cm⁻³ [92], though values closer to 4000 cm²/Vs have also been measured [91], and is closer to what is commercially available. In the computational model we use μ as a fit parameter and determine a value of 3800 cm²/Vs which is fixed for the model of all four unit cell types.

The depletion width x_n in an n-GaAs based Schottky diode can be calculated from [93-94].

$$x_n = \sqrt{\frac{2\epsilon_s(V_{bi} + V)}{qN_d}}$$

where $\epsilon_s = \epsilon_\infty$, the built-in voltage $V_{bi} = 0.9$ V at the Schottky junction interface between the Au (ELC) and n-GaAs, $N_d = 2 \times 10^{16}$ cm⁻³, and V is the applied voltage (taking positive values upon reverse bias). The unbiased depletion resulting from the V_{bi} is determined to have a depletion width of 250 nm. We model the depletion layer, which we restrict to being directly

underneath the metal. Breakdown and depletion width studies of n-doped GaAs have shown relatively close match to theory and have shown x_n beyond a micron can be achieved [95-96]. In our model we represent the depletion at maximum reverse bias $V_{\text{bias}} = -26.5$ V by sweeping n_{GaAs} underneath the 250 nm unbiased depletion width and keeping $\tilde{\epsilon}_{\text{GaAs}}(\omega)$ constant in the volume of the epi-layer beyond the ELC metal boundary.

The results from our computational model are plotted as the dashed curves in Figure 7.3a-d and show excellent agreement with experiment as n_{GaAs} depletes down from $2 \times 10^{16} \text{ cm}^{-3}$ to $1 \times 10^{14} \text{ cm}^{-3}$ the tunability in the absorption saturates and remains unchanged as depicted in Figure 7.6a. The mechanism of tunability of the MMA can be explored by observation of the surface current density and magnitude of the THz electric field (plotted directly underneath the ELC) as shown in Figure 7.6b. We find that the surface current density is similar to that found in prior investigations [97] and, as expected, the THz electric field is primarily localized underneath the ELC focused just beyond the gap edge.

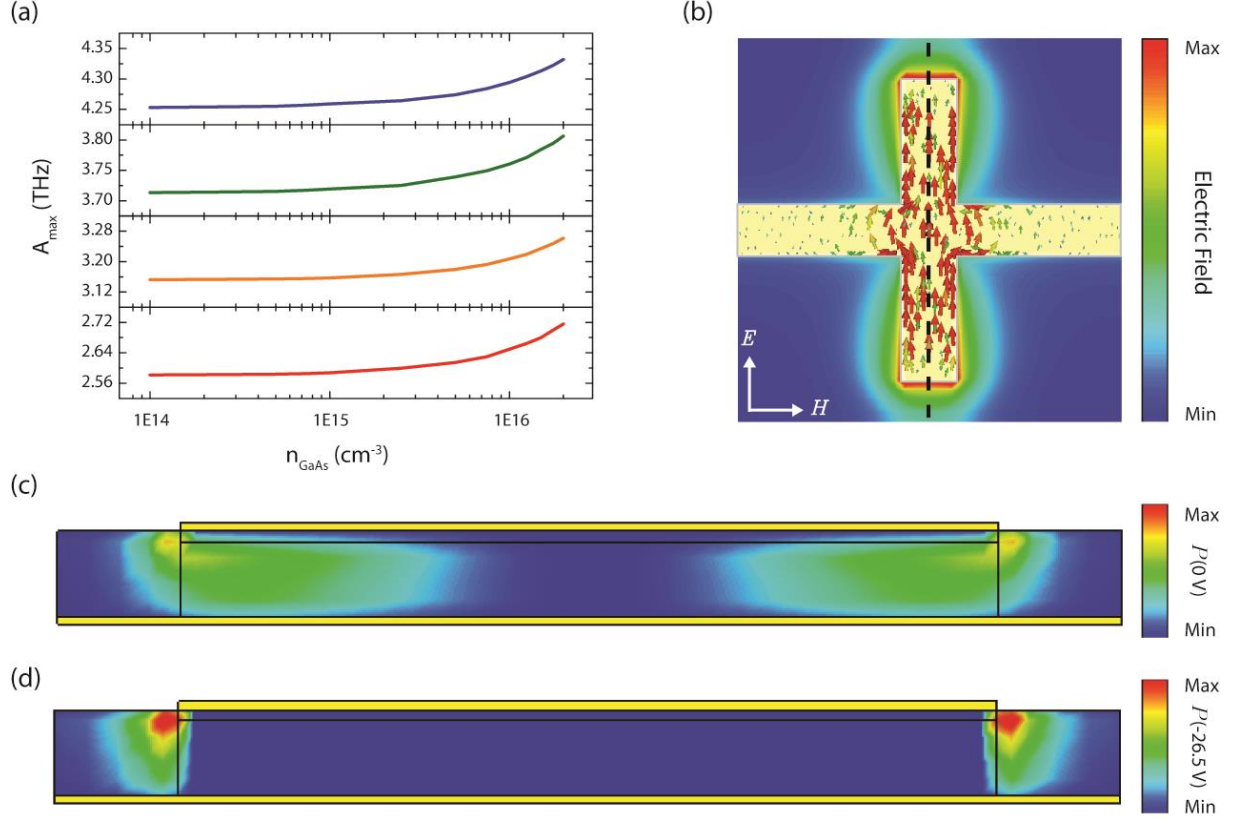


Figure 7.6: Numerical simulation results of the metamaterial absorber. (a) Frequency location of the absorption maximum (A_{max}) as a function of carrier concentration in the n-GaAs epitaxial layer which lies underneath the ELC Au metal and 250 nm threshold depletion layer. (b) Simulated current density in the ELC and the electric field magnitude plotted in plane for the case of the unbiased absorption maximum A_{max} ($V_{bias} = 0$) = 2.72 THz as indicated by the red dashed line in Fig. 2(a). (c,d) Power loss density shown for a cross sectional cut (black dashed line in (b)), for V_{bias} equal to 0 V (c) and -26.5 V (d).

Unlike the electric field distribution which is relatively unchanged, the power loss density distribution, shown in Figure 7.6c,d for both the unbiased and maximum bias cases, is strongly dependent on carrier density spatially located through the epi layer with the loss removed from the depleted volume. The form of the metamaterial absorptive feature strongly

depends on the value of the complex dielectric constant that the local terahertz electric field experiences. In particular the resonant frequency is set by the real part of the dielectric function, whereas the width of the absorption is determined by dielectric loss. Thus future designs can achieve greater modulation of the absorption peak by either removing the region of the epi layer that is not depleted or operate at lower frequencies where simulations indicate modulation depth can be improved due to increased damping of the resonance.

The modulation speed of the device was measured and the results are shown in Figure 7.4c. We input a square wave voltage between 0 and -10 V, and sweep the modulation frequency allowing us to measure the device RC time constant as has been done in previous studies¹⁶, where by loading external series resistors, the device capacitance can be extracted. The forward resistance R of the Schottky diode is measured to be 100Ω . The depletion capacitance C is extracted by using two different external series resistors of 0.98 and 2.16 k Ω , providing measured roll-off of 50 and 45 kHz respectively. The solid curves in Figure 7.4c represent the fits to the experimental data using the RC time constants as the fitting parameter. The resulting 3 dB roll-off frequency f_c of 10 MHz was determined from these fits.

7.4 Summary

In this chapter, we have demonstrated for the first time an electronic controlled multi-color spatial light modulator with super-pixels composed of arrays of terahertz metamaterial absorbers device capable of modulation of THz radiation at frequencies up to 10's of MHz, modulation depths of up to 50 percent, frequency tunability greater than 5 percent. By utilizing an n-doped gallium arsenide epitaxial layer as the dielectric spacer in the MMA, and then flip chip bonding the MMA to a carrier wafer we are able to achieve high pixel density

preserving pixel independence and maintaining minimal device capacitance to allow for high speed modulation. The design framework also lends to scalability and is sufficient to be able to accommodate large active areas for much larger pixel count for real applications. This work demonstrates a new path for construction of high speed terahertz electronic devices and has implications in numerous scientific and technological areas rich in applications, particularly in sensing, imaging, energy harvesting and dynamic scene projectors.

Chapter 8 : Summary and Future Work

In this dissertation, we examine both a QWIP and ICD detector hybridized with a metamaterial absorber for multicolor quantum efficiency enhancement in the infrared regime. We also explore dynamic multicolor metamaterials in the terahertz regime with electronically tunable frequency and gain. In Chapter 2, we discuss QWIP and ICD photodetectors used for the fabrication of a metamaterial photodetector and methods for their experimental characterization. In Chapter 3, we present a rigorous computational study that investigates the hybridization of a metamaterial absorber with an infrared photodetector for impedance matching to free space. Chapter 4 presents the fabrication of a conventional FPA, its transformation into a prototype test chip for the characterization of metamaterial devices, and an in-depth (patent pending) discussion on the fabrication of a metamaterial FPA on the wafer level. In Chapter 5, we experimentally analyze a QWIP photodetector in a metamaterial absorber cavity and discuss its design limitations for quantum efficiency enhancement. In chapter 6, we incorporate design lessons from the QWIP metamaterial detector and design, fabricate and demonstrate the first deep-subwavelength multispectral infrared detector using an ultra-thin T2-SL detector coupled with a metamaterial absorber with high quantum efficiency. We also identify useful versus non-useful absorption through a combination of absolute absorption and quantum efficiency measurements. In Chapter 7, we demonstrate a spatial light modulator (SLM) with multicolor super-pixels composed of arrays of electronically controlled terahertz (THz) MMAs. The device created here shows that fundamental light interactions of surfaces can be electronically controlled and provides a path forward for future designs.

8.1 Specific Detectivity Enhancement

Although significant improvement in quantum efficiency was demonstrated for a metamaterial photodetector at different colors for the first time, there remains untapped potential to significantly improve the detectors specific detectivity possibly beyond conventional photodetector designs. As suggested by Rogalski [1], dark current in infrared photodetectors is proportional to the device volume. Ultimately a thinner absorber should (in theory) greatly reduce the device dark current. Since high quantum efficiency can be achieved in metamaterial photodetectors with thinner absorbers, one would expect an improved overall device performance. The specific detectivity of a hypothetical conventional photodetector is calculated in Figure 8.1 with varying absorption coefficient values.

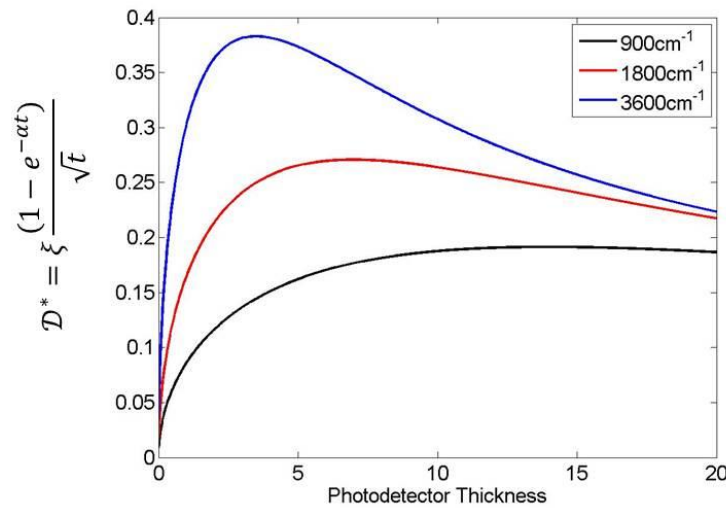


Figure 8.1: Detectivity versus photodetector thickness with varying absorption coefficient values

It is important to note that there is an optimum photodetector thickness that largely depends on the absorption coefficient of the active region of the photodetector. For an infrared

photodetector with an absorption coefficient of 3600cm^{-1} at the optimum thickness of $3.5\mu\text{m}$, the specific detectivity, D_C^* for a conventional detector (assuming the presence of an antireflection coating on the detector's optical aperture) is calculated as the following:

$$D_C^* = \xi \frac{(1 - e^{-\alpha t})}{\sqrt{t}} = \xi \frac{\eta}{\sqrt{t}} = \xi \frac{0.72}{\sqrt{3.5}} = \xi 0.385$$

where ξ is a physical constant. However, a metamaterial absorber hybridized with a photodetector can simultaneously improve the photodetector's quantum efficiency and reduce its dark current. For instance, if a photodetector with a resonant cavity is designed to absorb 90% of all incoming radiation in the active region of a photodetector with a photodetector thickness of 250nm , the specific detectivity for a metamaterial photodetector is the following:

$$D_M^* = \xi \frac{(1 - e^{-\alpha t})}{\sqrt{t}} = \xi \frac{\eta}{\sqrt{t}} = \xi \frac{0.90}{\sqrt{0.25}} = \xi 1.8$$

Taking the ratio of the specific detectivity for a metamaterial photodetector with a conventional photodetector, we define the following enhancement factor (EF):

$$EF = \frac{\xi 1.8}{\xi 0.385} = 4.7$$

As a result, we can achieve an EF approximately 4.7 times greater than what is physically possible with an optimized conventional photodetector design. However, in order to realize such performance enhancement, further optimization in thin detector design maybe required for the suppression of other non-ideal dark current components.

References

1. A. Rogalski, "New Material systems for third generation infrared photodetectors," *Opto-Electron. Rev.* 16, 458 (2008).
2. M. L. Althouse and C. I. Chang, "Chemical vapor detection with a multispectral thermal imager," *Opt. Eng.* 30, 1725 (1991).
3. S. Krishna, "The infrared retina," *J. Phys. D: Appl. Phys.* 42, 234005 (2009).
4. C. Destefanis, P. Tribolet, "Advanced MCT technologies in France," *Proceedings of SPIE* 6542, 65420D-1 (2007).
5. G. Destefanis, J. Baylet, P. Ballet, F. Rothan, O. Gravrand, J. Rothman, J.P. Chamonal, "Status of HgCdTe bicolor and dual band infrared focal plane arrays at LETI," *Journal of Electronic Materials*, 36 (8), 1031 (2007).
6. T. Whitaker, "Sanders' QWIPs detect two colors at once," *Compound Semicond.* 5(7), 48-51 (1999).
7. S. D. Gunapala, S. V. Bandara, J. K. Liu, J. M. Mumolo, C. J. Hill, E. Kurth, J. Woolway, P. D. LeVan and M. Z. Tidrow, "Toward dualband megapixel QWIP focal plane arrays," *Proceedings of SPIE* 6542, 65420W (2007).
8. E. Costard, J. P. Truffer, O. Huet, L. Dua, A. Nedelcu, J. A. Robo, X. Marcadet, N. Briere de l'Isle, P. Bois, A. Manissadjian and D. Gohier, "Two color QWIP and extended wavebands," *Proceedings of SPIE* 6542, 65420X (2007).
9. A. Rogalski, "HgCdTe infrared detector material: history, status, and outlook," *Reports on Progress in Physics*, 58, 2267 (2005).

10. R. Rehm, M. Walther, J. Fleibner, J. Schmitz, J. Ziegler, W. Cabanski and R. Breiter, "Bispectral thermal imaging with quantum well infrared photodetectors and InAs/GaSb type-II superlattices," *Proceedings of SPIE*, 6206, 6206-34 (2006).
11. R. Rehm, M. Walther, J. Schmitz, J. Fleissner, J. Ziegler, W. Cabanski, R. Breiter, *Electronics Letters*, 42, 577 (2006).
12. P.-Y. Delaunay, B.-M. Nguen, D. Hoffman, A. Hood, E.-K.-W. Huang, M. Razeghi, M. Tidrow, *Applied Physics Letters*, 92, 111112 (2008).
13. M. C. K. Wiltshire, J. B. Pendry, I. R. Young, D. J. Larkman, D. J. Gilderdale, and J. V. Hajnal, "Microstructured Magnetic Materials for RF Flux Guides in Magnetic Resonance Imaging," *Science* 291, 849-851 (2001).
14. M. Gokkavas, K. Guven, I. Bulu, K. Aydin, R. S. Penciu, M. Kafesaki, C. M. Soukoulis and E. Ozbay, "Experimental demonstration of a left-handed metamaterial operating at 100 GHz," *Phys. Rev. B* 73, 193103 (2006).
15. T. J. Yen, W. J. Padilla, N. Fang, D. C. Vier, D. R. Smith, J. B. Pendry, D. N. Basov, X. Zhang, "Terahertz Magnetic Response from Artificial Materials," *Science* 303, 1494-1496 (2004).
16. S. Linden, C. Enkrich, M. Wegener, J. Zhou, T. Koschny, and C. M. Soukoulis, "Magnetic Response of Metamaterials at 100 Terahertz," *Science* 306, 1351-1353 (2004).
17. S. Zhang, W. Fan, N. C. Panoiu, K. J. Malloy, R. M. Osgood, and S. R. J. Brueck, "Experimental Demonstration of Near-Infrared Negative-Index Metamaterials," *Phys. Rev. Lett.* 95, 137404 1-4 (2005).

18. C. Enkrich, M. Wegener, S. Linden, S. Burger, L. Zschiedrich, F. Schmidt, J. F. Zhou, T. Koschny, and C. M. Soukoulis, "Magnetic Metamaterials at Telecommunication and Visible Frequencies," *Phys. Rev. Lett.* 95, 203901 1-4 (2005).
19. J. Zhou, T. Koschny, M. Kafesaki, E. N. Economou, J. B. Pendry, and C. M. Soukoulis, "Saturation of the Magnetic Response of Split-Ring Resonators at Optical Frequencies," *Phys. Rev. Lett.* 95, 223902 1-4 (2005).
20. N. Landy, S. Sajuyigbe, J. Mock, D. Smith, and W. Padilla, "Perfect metamaterial absorber," *Physical Review Letters* 100, 207402 (2008).
21. J. Hao, J. Wang, X. Liu, W. J. Padilla, L. Zhou, and M. Qiu, "High performance optical absorber based on a plasmonic metamaterial," *Applied Physics Letters* 96, 251104-251104-3 (2010).
22. W. J. Padilla and X. Liu, "Perfect electromagnetic absorbers from microwave to optical," *SPIE Newsroom Optical Design and Engineering* 10, 003137 (2010).
23. N. Landy, S. Sajuyigbe, J. Mock, D. Smith, and W. J. Padilla, "Perfect metamaterial absorber," *Phys. Rev. Lett.* 100, 207402 (2008).
24. C. M. Watts, X. Liu, W. J. Padilla, "Metamaterial Electromagnetic Wave Absorbers." *Adv. Mater.* (2012).
25. X. Liu, "Taming the blackbody with infrared metamaterials as selective thermal emitters," *Phys. Rev. Lett.* 107, 45901 (2011).
26. K. Aydin, V. E. Ferry, R. M. Briggs, and H. A. Atwater, "Broadband polarization-independent resonant light absorption using ultrathin plasmonic super absorbers," *Nature Communications* 2, 517 (2011).

27. J. A. Montoya, S. A. Myers, A. V. Barve, J. O. Kim, S. Krishna, D. W. Peters, C. M. Reinke, and J. Wendt, "Broadband enhancement of infrared photodetectors with metamaterial resonators," *Proc. of SPIE Vol. 8704* 870437-1 (2013).
28. S. J. Lee, Z. Ku, A. Barve, J. A. Montoya, W. Y. Jang, S. R. J. Brueck, M. Sundaram, "A monolithically integrated plasmonic infrared quantum dot camera," *Nature Communications* 2, 286 (2011).
29. J. A. Montoya, A. V. Barve, R. V. Shenoi, M. Naydenkov, H. Kim, Z. Ku, S. R. J. Brueck, S. Krishna, S. J. Lee, and S. K. Noh, "Backside illuminated infrared detectors with plasmonic resonators," *SPIE Defense, Security, and Sensing* 76603P-76603P-5 (2010).
30. A. V. Barve, Y. D. Sharma, J. A. Montoya, J. Shao, T. Vandervelde, T. Rotter, and S. Krishna, "Engineering the barrier of quantum dots-in-a-well (DWELL) infrared photodetectors for high temperature operation," *Int. J. High Speed Electron. Syst.* 20, 549-555 (2011).
31. A. V. Barve, S. Sengupta, J.-O. Kim, J. Montoya, B. Klein, M. A. Shirazi, M. Zamiri, Y. D. Sharma, S. Adhikary, S. E. Godoy, W.-Y. Jang, G. R. C. Fiorante, S. Chakrabarti, S. Krishna, "Barrier selection rules for quantum dots-in-a-well infrared photodetector," *IEEE J. Quantum Electron.* 48, 1243-1251 (2012).
32. Z.-B. Tian, S. E. Godoy, H. S. Kim, T. Schuler-Sandy, J. A. Montoya, and S. Krishna, "High operating temperature interband cascade focal plane arrays," *Appl. Phys. Lett.* 105, 051109 (2014).

33. Z.-B. Tian, S. E. Godoy, H. S. Kim, T. Schuler-Sandy, J. A. Montoya, and S. Krishna, "Mid-wave infrared interband cascade photodetectors and focal plane arrays," SPIE Defense+ Security OPTO, 90701K-90701K-10.
34. Z.-B. Tian, T. Schuler-Sandy, S. E. Godoy, H. S. Kim, J. A. Montoya, and S. Krishna, "Mid-wave infrared interband cascade photodetectors and focal plane arrays based on InAs/GaSb superlattices," Photonics Conference (IPC), 2013 IEEE, 598-599.
35. Z.-B. Tian, T. Schuler-Sandy, S. E. Godoy, H. S. Kim, Quantum engineered mid-infrared type-II InAs/GaSb superlattice photodetectors for high temperature operation
36. D. Shrekenhamer, J. A. Montoya, S. Krishna, and W. J. Padilla, "Four-color metamaterial absorber THz spatial light modulator," *Adv. Opt. Mater.* 1 (12), 905-909.
37. C. M. Watts, D. Shrekenhamer, J. A. Montoya, G. Lipworth, J. Hunt, T. Sleasman, S. Krishna, D. R. Smith, and W. J. Padilla, "Terahertz compressive imaging with metamaterial spatial light modulators," *Nature Photonics* 8, 605-609 (2014).
38. C. M. Watts, D. Shrekenhamer, J. A. Montoya, G. Lipworth, J. Hunt, T. Sleasman, S. Krishna, D. R. Smith, and W. J. Padilla, "Coded and compressive THz imaging with metamaterials," SPIE OPTO, 89851N-89851N-10 (2014).
39. D. Shrekenhamer, C. M. Watts, J. A. Montoya, S. Krishna, and W. J. Padilla, "Metamaterial-based imaging for potential security applications," SPIE OPTO, 863221-7 (2013).
40. R. Tsu, L. Esaki, and B. A. Sai-Halasz, "A new semiconductor superlattice," *Appl. Phys. Lett.* 30, 651 (2012).

41. D. L. Smith, and C. Mailhot, "Theory of semiconductor superlattice electronic structure," *Rev. Mod. Phys.*, 62, 173 (1990).
42. R. H. Miles, D. H. Chow, J. N. Schulman, and T. C. McGill, "The infrared retina," *Appl. Phys. Lett.* 57, 801 (1990).
43. C. H. Grein, H. Cruz, M. E. Flatte and H. Ehrenreich, "Theoretical performance of very long wavelength InAs/In_xGa_{1-x}Sb superlattice based infrared detectors," *Appl. Phys. Lett.* 65, 2530 (1994).
44. J. R. Meyer, C. A. Hoffman, F. J. Bartoli, and L. R. Ram-Mohan, "Type-II quantum-well lasers for the mid-wavelength infrared," *Appl. Phys. Lett.* 67, 757 (1995).
45. B. H. Yang, D. Zhang, Rui Q. Yang, C.-H. Lin, S. J. Murry, and S. S. Pei, "Mid-infrared interband cascade lasers with quantum efficiencies >200%," *Appl. Phys. Lett.* 72, 2220 (1998).
46. A. P. Ongstad, G. C. Dente, M. L. Tilton, D. Gianardi, G. Turner, "Linewidth analysis of the photoluminescence from InAs/GaSb/InAs/AlSb type-II superlattices," *Appl. Phys. Lett.*, 87, 7896 (2000).
47. R. Rehm, M. Walther, J. Schmitz, J. Fleibner, S. Kopta, F. Fuchs, W. Cabanski, and J. Ziegler, "Growth of InAs/GaSb short-period superlattices for high-resolution mid-wavelength infrared focal plane array detectors," *J. Cryst. Growth*, 278, 156 (2005).
48. Y. Wei, A. Hood, H. Yau, M. Z. Tidrow, A. Gin, M. Razeghi, and V. Nathan, "Uncooled operation of type-II InAs/GaSb superlattice photodiodes in the midwavelength infrared range," *Appl. Phys. Lett.* 86, 233106 (2005).

49. E. Plis, J. –B. Rodriguez, H. S. Kim, G. Bishop, Y. D. Sharma, L. R. Dawson, S. Krishna, S. J. Lee, C. E. Jones, and V. Gopal, “Type II InAs/GaSb strain layer superlattice detectors with p-on-n polarity,” *Appl. Phys. Lett.* 91, 133512 (2007).
50. J. Bergman, G. J. Sullivan, A. Ikhlassi, C. Grein, R. E. DeWames, J. R. Waldrop, H. Yang, M. Flatte, K. Mahalingam, M. Zhong, and M. Weimer, “Molecular beam epitaxy growth of high quantum efficiency InAs/GaSb superlattice detectors,” *J. Vac. Sci. Technol. B*, 23, 1144 (2005).
51. I. Vurgaftman, E. H. Aifer, C. L. Canedy, J. G. Tischler, J. R. Meyer, J. H. Warner, J. M. Jackson, G. Hildebrandt, and G. J. Sullivan, “Graded band gap for dark-current suppression in long-wave infrared W-structured type-II superlattice photodiodes,” *Appl. Phys. Lett.* 89, 121114 (2006).
52. G. J. Brown, F. Szmulowicz, K. Mahalingam, S. Houston, Y. Wei, A. Gin, and M. Razeghi, “Recent advances in InAs/GaSb superlattices for very long wavelength infrared detection,” *Proc. SPIE*, 4999, 457 (2003).
53. Rogalski, “Progress in focal plane array technologies,” *Progress in Quantum Electronics* 36 342–473 (2012).
54. V. G. Veselago, “The electrodynamics of substances with simultaneously negative values of ϵ and μ ,” *Sov. Phys. Usp.* 10, 509 (1968).
55. D. R. Smith, W. J. Padilla, D. Vier, S. C. Nemat-Nasser, and S. Schultz, “Composite medium with simultaneously negative permeability and permittivity,” *Physical Review Letters* 84, 4184-4187 (2000).
56. R. Shelby, D. Smith, and S. Schultz, “Experimental verification of a negative index of refraction,” *Science* 292, 77-79 (2001).

57. D. Schurig, J. Mock, B. Justice, S. A. Cummer, J. Pendry, A. Starr, and D. Smith, "Metamaterial electromagnetic cloak at microwave frequencies," *Science* 314, 977-980 (2006)
58. J. B. Pendry, "Negative refraction makes a perfect lens," *Physical Review Letters* 85, 3966-3969 (2000)
59. N. Fang, H. Lee, C. Sun, and X. Zhang, "Sub-diffraction-limited optical imaging with a silver superlens," *Science* 308, 534-537 (2005)
60. J. B. Pendry, A. Holden, D. Robbins, and W. Stewart, "Magnetism from conductors and enhanced nonlinear phenomena," *IEEE Transactions on Microwave Theory and Techniques* 47, 2075-2084 (1999)
61. J. Pendry, A. Holden, W. Stewart, and I. Youngs, "Extremely low frequency plasmons in metallic mesostructures," *Physical Review Letters* 76, 4773-4776 (1996)
62. D. Schurig, J. Mock, and D. Smith, "Electric-field-coupled resonators for negative permittivity metamaterials," *Applied Physics Letters* 88, 041109-041109-2 (2006)
63. W. Padilla, M. Aronsson, C. Highstrete, M. Lee, A. Taylor, and R. Averitt, "Electrically resonant terahertz metamaterials: Theoretical and experimental investigations," *Physical Review B* 75, 041102 (2007)
64. N. Landy, S. Sajuyigbe, J. Mock, D. Smith, and W. J. Padilla, "Perfect metamaterial absorber," *Physical Review Letters* 100, 207402 (2008)
65. X. Liu, T. Starr, A. F. Starr, and W. J. Padilla, "Infrared spatial and frequency selective metamaterial with near-unity absorbance," *Physical Review Letters* 104, 207403 (2010)

66. D. Smith, S. Schultz, P. Markos, and C. Soukoulis, "Determination of effective permittivity and permeability of metamaterials from reflection and transmission coefficients," *Physical Review B* 65, 195104 (2002).
67. M. R. Kitchin and M. Jaros, "Characterization of GaSb/InAs type II infrared detectors at very long wavelengths: carrier scattering at defect clusters," *Physica E-Low-Dimensional Systems & Nanostructures*, vol. 18, pp. 498-508, 2003.
68. S. Krishna, "The infrared retina," *J. Phys. D: Appl. Phys.* 42, 234005 (2009).
69. J. Montoya, S. Myers, and S. Krishna. *U.S. Patent Application No. 14/290,619*. Washington, D.C.: U.S. Patent and Trademark Office (2014). For further details: <http://www.flintbox.com/public/project/23459/>
70. Y.-S. Lee, K. Upadhyaya, K. J. Nordheden, M.-Y. Kao, "Selective reactive ion etching of GaAs/AlAs in BCl₃/SF₆ for gate recess," *Journal of Vacuum Science & Technology B Microelectronics and Nanometer Structures* 18(5) 2505-2508 (2000).
71. C.-W. Cheng, K.-T. Shiu, N. Li, S.-J. Han, L. Shi, and D. K. Sadana, "Epitaxial lift-off process for gallium arsenide substrate reuse and flexible electronics," *Nature Communications*, 4, 1-4 (2013).
72. N. Yoshida, Y. Yamamoto, H. Takano, T. Sonoda, S. Takamiya, and S. Mitsui, "Alloyed and non-alloyed Ohmic contacts for AlInAs/InGaAs high electron mobility transistors," *Jpn. J. Appl. Phys.* 1, 33, (6A), pp. 3373–3376 (1994).
73. W. Zhao, L. Wang, I. Adesida, "Electrical and structural investigations of Ag-based Ohmic contacts for InAlAs/InGaAs/InP high electron mobility transistors," *Appl. Phys. Lett.* 89, 072105 (2006).

74. A. Rogalski, "New Material systems for third generation infrared photodetectors," *Opto-Electron. Rev.* 16, 458 (2008).
75. ZB Tian, SE Godoy, HS Kim, T Schuler-Sandy, J. A. Montoya, S Krishna, "High operating temperature interband cascade focal plane arrays," *Applied Physics Letters* 105 (5), 051109 (2014).
76. ZB Tian, R. T. Hinkley, R. Q. Yang, D. Lubyshev, Y. Qiu, J. M. Fastenanu, W. K. Liu, SE Godoy, HS Kim, T Schuler-Sandy, J. A. Montoya, S Krishna, "High operating temperature interband cascade focal plane arrays," *Journal of Applied Physics* 111 (2), 024510 (2012).
77. W.-Y. Jang, M. M. Hayat, P. Zarkesh-Ha, and S. Krishna, "Continuous time-varying biasing approach for spectrally tunable infrared detectors," *Optics Express*, vol. 20(28), pp.29823-37, (2012).
78. M. Tonouchi, "Cutting-edge terahertz technology," *Nature Photonics* 1, 97-105 (2007).
79. W. J. Padilla, A. J. Taylor, C. Highstrete, M. Lee, R. D. Averitt, "Dynamical electric and magnetic metamaterial response at terahertz frequencies," *Phys. Rev. Lett.* 96, 107401 (2006).
80. H. T. Chen, "Active terahertz metamaterial devices," *Nature* 444, 597-600 (2006).
81. T. Driscoll, "Dynamic tuning of an infrared hybrid-metamaterial resonance using vanadium dioxide," *Appl. Phys. Lett.* 93, 024101-024101-3 (2008).
82. H. Tao, "Reconfigurable terahertz metamaterials," *Phys. Rev. Lett.* 103, 147401 (2009).

83. U. Efron, "Spatial light modulator technology: materials, devices, and applications" (CRC, 1994).
84. R. A. DeVerse "Applications of spatial light modulators for new modalities in spectrometry and imaging (Biomedical Optics 2003, International Society for Optics and Photonics, 2003).
85. M. F. Duarte, "Single-pixel imaging via compressive sampling," *Signal Processing Magazine, IEEE* 25, 83-91 (2008).
86. D. Dudley, W. Duncan, and J. Slaughter, "Emerging digital micromirror device (DMD) applications (Prof. SPIE Ser. 4985, 2003).
87. K. M. Johnson, D. J. McKnight, and I. Underwood, "Smart spatial light modulators using liquid crystals on silicon," *Quantum Electronics, IEEE Journal* 29, 699-714 (1993).
88. J. P. Rice, J. E. Neira, M. Kehoe, and R. Swanson, "DMD diffraction measurements to support design of projectors for test and evaluation of multispectral and hyperspectral imaging sensors (SPIE MOEMS-MEMS: Micro-and Nanofabrication, International Society for Optics and Photonics (2009).
89. B. Walther, "Spatial and Spectral Light Shaping with Metamaterials," *Adv. Mater.* (2012).
90. Y. Urzhumov, "Electronically reconfigurable metal-on-silicon metamaterial," *Phys. Rev. B* 86, 075112 (2012).
91. T. I. Jeon, and D. Grischkowsky, "Characterization of optically dense, doped semiconductors by reflection THz time domain spectroscopy," *Appl. Phys. Lett.* 72, 3032-3034 (1998).

92. P. Huggard, "Drude conductivity of highly doped GaAs at terahertz frequencies," *J. Appl. Phys.* 87, 2382-2385 (2000).
93. S. M. Sze, and K. K. Ng, "Physics of semiconductor devices," (Wiley-interscience, 2006).
94. M. Shur, "Introduction to electronic devices" (1996).
95. B. Baliga, R. Ehle, J. Shealy, and W. Garwacki, "Breakdown characteristics of gallium arsenide," *Electron Device Letters, IEEE* 2, 302-304 (1981).
96. M. Hudait, S. Krupanidhi, "Breakdown characteristics of MOVPE grown Si-doped GaAs Schottky diodes," *Solid-state Electronics* 43, 2135-2139 (1999).
97. D. Schurig, J. Mock, and D. Smith, "Electric-field-coupled resonators for negative permittivity metamaterials," *Appl. Phys. Lett.* 88, 041109-041109-3 (2006).
98. H. T. Chen, "Hybrid metamaterials enable fast electrical modulation of freely propagating terahertz waves," *Appl. Phys. Lett.* 93, 091117-091117-3 (2008).